Ultrasonic distance detection in spinal cord stimulation

Emiel Dijkstra

2003

Ph.D. thesis
University of Twente

Twente University **Press**

Also available in print:
http://www.tup.utwente.nl/

ULTRASONIC DISTANCE DETECTION IN SPINAL CORD STIMULATION

The research described in this thesis was carried out at the Institute for Biomedical Technology and the MESA$^+$ Research Institute at the University of Twente. The financial support by Medtronic Inc. is gratefully acknowledged.

Twente University **Press**

Publisher:
Twente University Press
P.O. Box 217, 7500 AE Enschede, the Netherlands,
www.tup.utwente.nl

Print: Océ Facility Services, Enschede

ISBN 9036518636

ULTRASONIC DISTANCE DETECTION IN SPINAL CORD STIMULATION

PROEFSCHRIFT

ter verkrijging van
de graad van doctor aan de Universiteit Twente,
op gezag van de rector magnificus,
prof. dr. F.A. van Vught,
volgens besluit van het College voor Promoties
in het openbaar te verdedigen
op donderdag 27 februari 2003 te 15.00 uur

door

Emiel Arjen Dijkstra
geboren op 28 april 1971
te Groningen

Dit proefschrift is goedgekeurd door:

de promotor:	Prof. dr. ir. P. Bergveld
de assistent-promotor:	Dr. ir. W. Olthuis

Table of contents

Chapter 1

Introduction

1.1 Spinal cord stimulation

Already during the Roman Empire, physicians used electric eels in the treatment of chronic pain [1]. Various forms of electrical stimulation to treat chronic pain, such as transcutaneous electrical nerve stimulation (TENS), have been applied since then. In 1967, spinal cord stimulation was applied for the first time to treat a man suffering from cancerous pain [2]. Although nowadays spinal cord stimulation (SCS) is a well-established modality for the management of some types of chronic intractable pain, the efficacy of the method is still not satisfactory. Therefore, theoretical as well as empirical methods are used to improve this method of treating primarily chronic pain [3,4].

SCS for the management of chronic pain is based on electrical stimulation of ascending nerve fibers on the posterior side of the spinal cord, the dorsal columns. The sensory nerve fibers composing the dorsal columns play an important role in the modulation of the transmission of pain signals to the brain. According to the physiological "gate-control" theory of Melzack and Wall [5] stimulation of dorsal column fibers diminishes or blocks the transmission of pain signals. An electric pulse of a few hundreds of microseconds is applied to a selection of the electrodes integrated on an electrode array and connected to either the positive or negative output of a voltage-driven pulse generator. A drawing of a plate electrode array is shown in figure 1–1a. The injected current causes an electric field in the spinal cord that stimulates the ascending nerve fibers. The electrode array is implanted in the epidural space at the posterior side of the spinal cord, as shown in figure 1–2.

Two types of SCS pulse generators are currently available: totally implantable pulse generators (IPG) and radio frequency (RF) systems. The IPG provides the constant voltage stimulation pulses applied to the spinal cord via the cable and electrode array. The IPG is implanted subcutaneously in the abdomen (figure 1–2), and contains a lithium battery. In average use, most patients can expect the battery to last 2.5 to 4.5 years. RF systems consist of a passive receiver im-

planted under the skin with a coil placed over the receiver on the skin and an external transmitter. RF systems can deliver more power than the lithium-powered systems, but require the patient to change batteries on a regular basis [6].

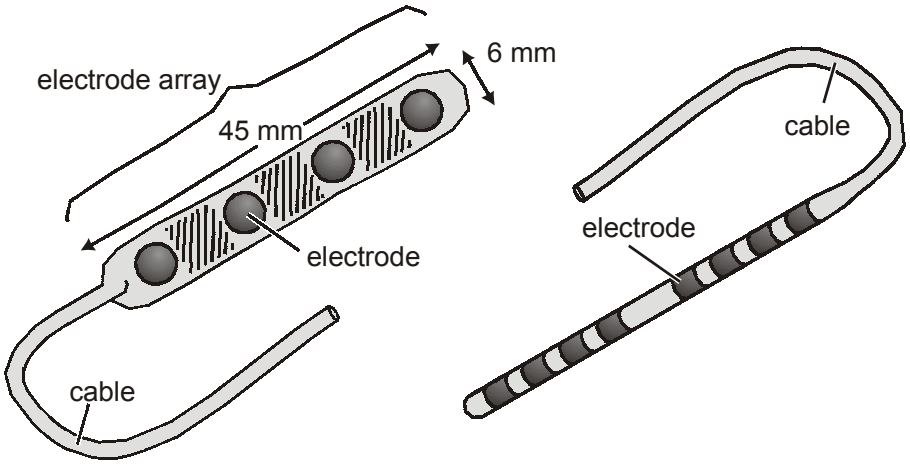

Figure 1–1 Schematic picture of (a) a plate electrode array and (b) a cylindrical electrode array.

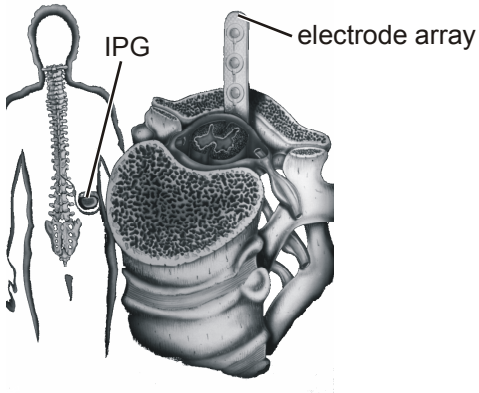

Figure 1–2 View on part of the vertebral column with the spinal cord and an epidurally placed plate electrode array for SCS (right); the IPG is placed in the abdomen (left).

Besides plate electrode arrays which need open surgery for their implantation, cylindrical electrode arrays (figure 1–1b) placed percutaneously via a cannula, are used as well [6]. However, these arrays are too small for a distance detection transducer.

1.1.1 Anatomical structure of the spinal cord

Figure 1–3 shows a schematic cross section of the spinal canal and the position of the electrode array. The spinal cord floats in the dural sac, a column of cerebrospinal fluid (CSF) surrounded by the dura mater. The CSF is optically clear. The spinal cord is surrounded by a thin smooth layer: the pia mater. At each

spinal segment a pair of posterior and anterior roots leaves the spinal cord on both sides and they join lateral to the spinal cord (figure 1–3) before leaving the dural sac as spinal nerves. This anatomical structure enables the spinal cord to move primarily in an anterior and posterior direction inside the dural sac, while little shift in lateral directions is possible as well. The actual position of the spinal cord in the dural sac depends on the position and posture of a subject as shown in figure 1–4.

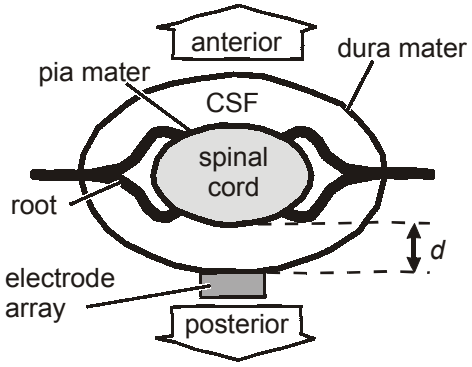

Figure 1–3 Schematic cross section of the spinal canal including the distance d to be measured between the electrode array and the spinal cord.

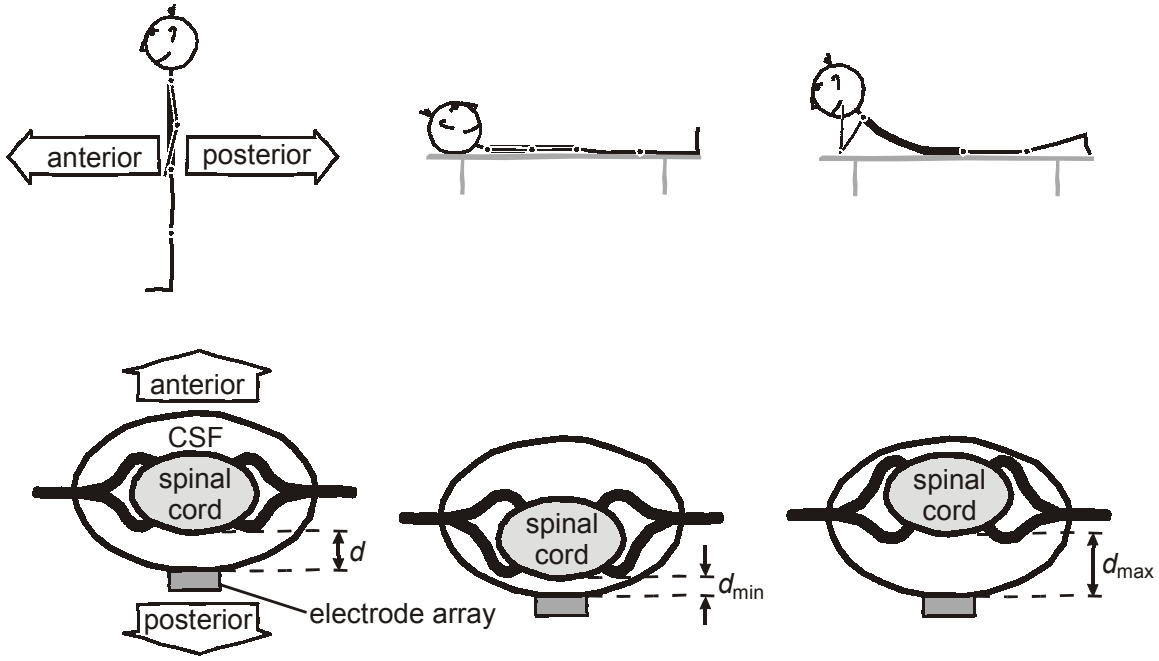

Figure 1–4 Position of the spinal cord with respect to the position of a person (a) standing, (b) supine and (c) prone.

In an MRI study by Holsheimer *et al.* [7] the thickness of the dorsal CSF layer was measured at different spine levels in 26 healthy volunteers. It was shown that the thickness of the dorsal CSF layer varies roughly between 1 mm and 10 mm, depending on the vertebral level considered and the position of the subject. These situations are illustrated in figure 1–4. The MRI study showed that at T11 the mean thickness was approximately 2.2 mm larger when the subjects

were in a prone position than in a supine position. At T12 this mean difference was approximately 3.4 mm. When in patients a plate electrode array is inserted in the posterior epidural space, the thickness of the posterior CSF layer is likely to be 1 mm to 2 mm less. Because a plate electrode array is generally positioned next to the thin dura, the distance between the electrode array and the spinal cord is almost identical to the thickness of the posterior CSF layer. Table 1–1 lists the mean thicknesses of the CSF layer at T11 and T12 for prone and supine position and the difference between those two values (right column).

Table 1–1 The mean thickness of the posterior CSF layer at T11 and T12 for prone and supine position and the difference between those two values.

level	prone [mm]	supine [mm]	difference [mm]
T11	5.8	3.6	2.2
T12	6.4	3.0	3.4

1.1.2 The stimulation window

In present SCS systems the applied stimulus voltage pulse has a constant amplitude and duration. Therefore, the electric field in the spinal cord will vary with body position. To obtain a good clinical effect, i.e. that the patient feels neither pain, nor other uncomfortable sensations, the stimulation amplitude has to be kept within a rather narrow therapeutic range. Its lower limit relates to initial tingling sensations (paresthesia threshold), whereas stimulation above the upper limit elicits uncomfortable sensations and reflexive motor responses (discomfort threshold). The discomfort threshold generally exceeds the paresthesia threshold only by 35 % to 55 % [8]. To keep the electric field in the posterior spinal cord (almost) constant, the stimulus amplitude has to be varied when the distance d between the spinal cord and the electrode array is changed. From an inhomogeneous, anisotropic volume conductor model of SCS it was calculated by Holsheimer *et al.* [9] that the paresthesia threshold stimulus P [V], applied bipolarly by the electrode array, can be written as:

$$P = 0.765 \cdot 10^{d/d_0} - 0.57 \qquad (1\text{–}1)$$

where d is in millimeters, and d_0 is 11.49 mm. Figure 1–5 shows the paresthesia threshold P and the discomfort threshold D, which is 40 % higher than P [8], as a function of the distance d. The applied stimulus amplitude has to be maintained between paresthesia and discomfort threshold, resulting in the therapeutic window ΔS.

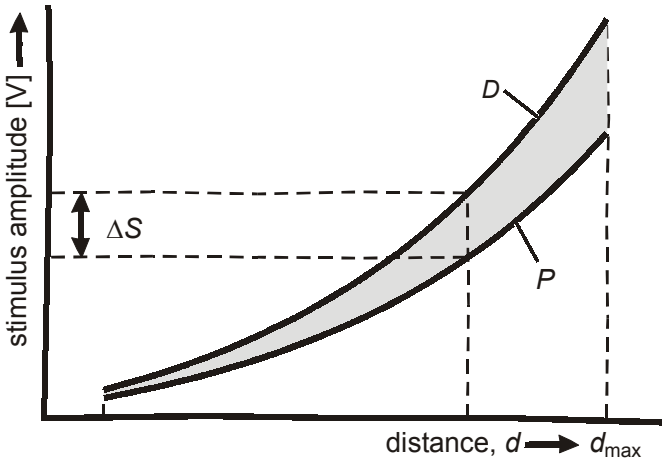

Figure 1–5 The required stimulus amplitude as a function of the distance between the electrode array and the spinal cord for optimal stimulation. The hatched area indicates the stimulation amplitude window ΔS.

1.1.3 Requirements for an improved SCS system performance

In order to obtain a therapeutic effect, the stimulus has to remain in the hatched area as given in figure 1–5. Because the distance *d* may vary substantially with changes in posture, it is therefore necessary to apply a distance-related stimulus. A major improvement of the current SCS system would be achieved when the distance between the electrode array and the spinal cord could be measured and used to control the stimulus amplitude automatically. Therefore, the following system properties would be required.

The measurement device should be biocompatible and non-toxic, while the distance measurement should be contactless, safe, harmless, and should be repeated regularly, e.g. once per minute. The distance between the electrode array and the spinal cord may vary between 1 mm and 10 mm. Because most electrodes are implanted in the low thoracic region (T11-T12) the range varies between 3.0 mm and 6.5 mm. The resolution of the measurement should be 0.5 mm, or less.

The distance detection system should have low power consumption, because significantly increased power consumption reduces the battery lifetime of an implanted system and necessitates a frequent replacement of the IPG. Replacement of the systems requires additional surgery. An RF system would, therefore, be more appropriate for the implementation of a distance detection system. The transducer should be integrated on the electrode array of which a schematic picture is shown in figure 1–1. The hatched areas indicate the space for the transducer for distance detection. The size of the transducer is limited to an area of 5 mm × 5 mm and a thickness of 2 mm. Robustness is also an important requirement for an in-vivo transducer.

Four methods for distance detection have been theoretically analyzed [10]: electrical, optical, opto-acoustic, and acoustic. According to the system requirements, the latter, using ultrasound, has been chosen to be implemented. For this method just one element is needed as a sensor and actuator, the size of the transducer can be kept small, the delay times can be detected electronically, and piezoelectric transducers in pulsed mode have low power dissipation. A similar idea to measure the distance between the electrode array and the spinal cord by ultrasound has been patented by Starkebaum and Rise [11].

1.1.4 Design criteria for ultrasonic distance measurement

Table 1–2 lists the system requirements for an (ultrasonic) distance measurement system (left column). From these requirements design criteria can be extracted which the transducer has to fulfill. The four design criteria, efficiency, dynamic range, axial resolution and size are discussed.

Table 1–2 System requirements and design criteria for an (ultrasonic) distance measurement system used for closed-loop SCS.

system requirement	design criterion
power consumption should be low to limit battery or IPG exchange	efficiency must be high to minimize power consumption
the reflected signal to be detected is small because the acoustic impedance of the spinal cord is close to the value of the surrounding fluid (CSF), and the distance measured is between 3 mm and 6.5 mm.	transducer range should be from 3 mm to 6.5 mm it is likely that the SNR needs to be increased
the position of the spinal cord should be measured with an accuracy of at least 0.5 mm for optimal stimulation	axial resolution must be at least 0.5 mm; $f_{res} \geq 1.5$ MHz
the transducer has to be integrated on the stimulating electrode array	the transducer size must be equal or less than an area of 5 mm × 5 mm and a thickness of 2 mm

The efficiency of a transducer is the ratio of the peak-peak amplitude of the driving signal and the echo signal. The efficiency can be improved by applying matching layers between the transducer and the medium into which the ultrasonic pulse is emitted [12,13]. This will increase the amplitude of the echo signal while the driving signal amplitude is kept constant.

The transducer range is defined by the minimum and maximum distance of an interface that can be detected by the transducer. The range not only depends on the noise level, but also on the properties of the media through which the sonic

wave propagates. Attenuation of an acoustic wave traveling through a medium takes place in two ways. First, a wave will diverge from the parallel beam or will be scattered by small discontinuities in the characteristic impedance, so the ultrasound power flows through an increased area. Secondly, absorption takes place: ultrasonic energy is converted into heat. Generally, the attenuation constant of solids is linearly proportional to the frequency, while the attenuation constant of liquids increases with the square of the frequency [14]. The transducer range is inversely related to the frequency. In conclusion, the highest frequency that can be used is limited by the frequency-dependent attenuation within the CSF. In the human body the attenuation is approximately 0.5 dB/(cm·MHz) [15] and in water it is 0.002 dB/(cm·MHz) [14]. The axial resolution decreases with the depth of penetration since lower frequencies must be used for deeper penetration.

Since the transducer must be integrated on the electrode array, the transducer dimensions are limited to an area of 5 mm × 5 mm and a thickness of 2 mm. The transducer resonance frequency is inversely proportional to the transducer thickness. The sound velocity in piezoelectric material roughly varies between 2000 and 5000 m/s, whereas the sound velocity in CSF will be approximately 1500 m/s (sound velocity in water). Generally, the resonance frequency f_{res} of a (ceramic) piezoelectric transducer is inversely proportional to twice its thickness t:

$$f_{res} = \frac{v_p}{2t} \tag{1–2}$$

where v_p [m/s] is the velocity of sound in the transducer. The frequency of the ultrasonic wave in the CSF is equal to the resonance frequency. The wavelength in CSF (λ_{CSF}) is the ratio of the sound velocity in the CSF (v_{CSF}) and the resonance frequency. The spatial resolution Δ corresponds to half the wavelength. This gives for the spatial resolution:

$$\Delta = \tfrac{1}{2}\lambda_{CSF} = \tfrac{1}{2}\frac{v_{CSF}}{f_{res}} = \frac{v_{CSF}}{v_p}\,t \tag{1–3}$$

Since the sound velocity in the transducer material is higher than in the CSF, it can be calculated that a transducer with a thickness of at most 2 mm can generate a wavelength of 0.5 mm or less.

By rewriting equation (1–3) the resonance frequency is found:

$$f_{res} = \frac{v_{CSF}}{2\Delta} \tag{1–4}$$

With a spatial resolution of 0.5 mm and v_{CSF} = 1500 m/s the minimum frequency is 1.5 MHz. In conclusion, a trade-off must be made between range and resolution, since a high resolution (high frequency) results in a low transducer range, and vice versa. The specifications can be met with the maximum transducer dimensions. In practice, the range will be smaller than 1 mm to 10 mm, that is 3 mm to 6.5 mm.

1.2 Piezoelectricity

1.2.1 The Piezoelectric effect

The piezoelectric effect can be described as the appearance of an electric potential difference across certain faces of a crystal when it is subjected to mechanical pressure. This is the direct effect: electricity originating from applied stress. Conversely, when an electric field is applied between certain faces of the crystal, the crystal undergoes mechanical distortion.

The piezoelectric effect occurs in several crystalline substances, such as barium titanate, tourmaline and lead zirconate titanate (PZT). The effect is caused by the displacement of ions in crystals that have a non-symmetrical unit cell, the simplest polyhedron that makes up the crystal structure. An example of a PZT unit cell is given in figure 1–6 (left). When the crystal is elongated, the ions in each unit cell are displaced, causing the electric polarization of the unit cell, as shown in figure 1–6 (right). Because of the regularity of crystalline structure these effects accumulate, causing the appearance of an electric potential difference between certain faces of the crystal. When an external electric field is applied to the crystal, the ions in each unit cell are displaced by electrostatic forces, resulting in the mechanical deformation of the whole crystal [16].

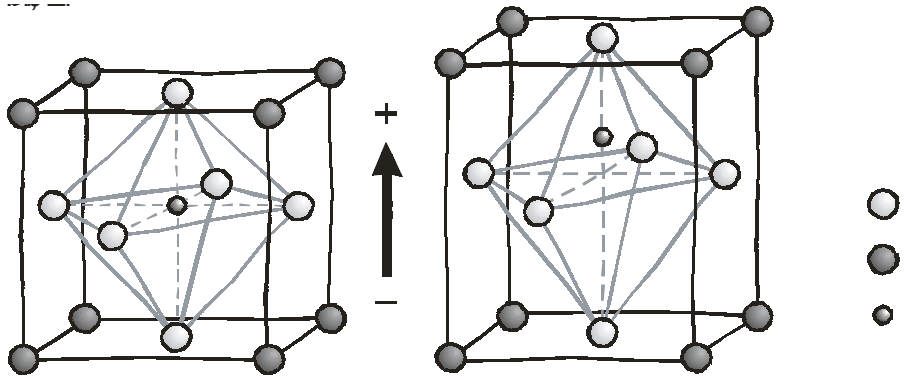

Figure 1–6 Unit cell PZT (left) in cubic phase and (right) in tetragonal phase.

1.2.2 History of piezoelectricity

1880–1882 The phenomenon that some materials, when they are heated, attract other materials (pyroelectricity) was known for a long time. In the eighteenth and nineteenth century tourmaline was studied to characterize the pyroelectric effect. These studies led to the discovery of the piezoelectric effect. The first experimental demonstration of a connection between macroscopic piezoelectric phenomena and crystallographic structure was published in 1880 by Pierre and Jacques Curie [17]. They found that in certain materials such as zincblende, tourmaline, cane sugar, topaz and quartz, mechanical stresses were accompanied by electric surface charges, which is called the direct piezoelectric

effect. The next year, Lippmann predicted the converse effect based on thermodynamic considerations: an imposed voltage produces mechanical deformations. The name "piezo" derives from the Greek *piezein*, meaning "to press". Nowadays, we say the effect couples electrical and elastical phenomena [16,18,19].

The first application did not occur until World War I when another Frenchman, Langevin, used piezoelectrically excited quartz plates to generate sound waves in water for use in submarine detection. Continuing past the end of the war, he achieved the goal of emitting a high frequency "chirp" underwater and measuring depth by timing the return echo [20]. Langevin, however, was not the first to propose echo ranging. In 1912 in response to the Titanic disaster, both airborne and underwater echo systems were suggested for iceberg detection. In 1914 echo-ranging underwater and detection of an iceberg was experimentally demonstrated [20].

1920–1940 In 1920, Vasalek discovered that the polarization of Rochelle salt ($NaKC_4H_4O_6.4H_2O$) could be reversed. Rochelle salt is ferroelectric, and was first prepared by Seignette around 1665 in La Rochelle, France. The term ferroelectricity was not used until the 1940s, but the phenomenon was known as Seignette electricity. Around the 1930s, quartz started to be replaced for underwater ultrasound applications by the strongly piezoelectric Rochelle salt.

The success of sonar (SOund NAvigation and Ranging) stimulated intense development activity on all kinds of piezoelectric devices. A new class of materials was developed based on the propagation of ultrasonic waves. In fact, during this revival following World War I, most of the classic piezoelectric applications with which we are now familiar (microphones, accelerometers, ultrasonic transducers, bender element actuators, phonograph pick-ups, signal filters, etc.) were conceived and put into practice.

1940–1950 The discovery of easily manufactured piezoelectric ceramics during World War II with astonishing performance characteristics touched off a revival of intense research and development into piezoelectric devices. Development of the barium titanate family –a piezoelectric ceramic– and later the lead zirconate titanate family were some of the advances in materials science that were made during this phase.

Up to that time Rochelle salt was used for underwater ultrasound applications. It was replaced because its properties were very susceptible to moisture. Piezoelectric ceramics had two major advantages, the improved efficiency to convert electrical into acoustical energy and the possibility to be processed into varying sizes and shapes. Moreover, piezoelectric ceramics did not require large amplitude voltages to drive them.

The scientific and engineering advances on naval and military radar during world war II helped enormously in the design of SONAR and ultrasonic detector devices in later years. Two of these advances made it possible to put ultrasound

into medical practice. First, the development of the electronic computer greatly improved signal processing capacities. Second, radar required fast electronic switching to replace electromechanical switching. This led AT&T's Bell Laboratories to initiate a solid-state research program that led to the invention of the point-contact transistor in 1947 [20].

The early use of ultrasonics in the field of medicine was largely confined to its application in therapy rather than diagnosis, utilizing its heating and disruptive effects on tissues. Two references [21,22] claim to have the first diagnostic ultrasound application, although there is a gap of 13 years between both events. Both applications deal with the visualization of tumors. In 1942, Dussik employed ultrasound in medical diagnosis. He located brain tumors and the cerebral ventricles by measuring the transmission of an ultrasound beam through the head, employing a transducer on either side. This technique was not quite successful because the skull absorbed much of the ultrasound energy and there were also technical inadequacies in recording the generated results [21].

Shortly after the end of World War II, researchers in Japan began to explore medical diagnostic capabilities of ultrasound, building the first commercially available ultrasonic equipment in 1949, with A-mode (amplitude) presentation (see figure 1–7): a line on an oscilloscope screen. This was followed by equipment with B-mode (brightness) presentation: two dimensional, gray scale imaging [23]. This two dimensional technique was independently conceived by several pioneers of the 1950s [24].

Figure 1–7 The first A-mode scanner that Uchida built in the late 1940's.

1950–1960 Diagnostic ultrasound has been in clinical use since the late 1950's, when Donald started to use sonar for diagnosis of tumors. Early results were disappointing and the enterprise was greeted with a mixture of skepticism and ridicule. However, a dramatic case where ultrasound saved a patient's life by diagnosing a huge, easily removable, ovarian cyst in a woman who had been diagnosed as having inoperable cancer of the stomach, made people take the

technique seriously. Later Donald was using ultrasound not only for abdominal tumors in women but also for fetal imaging on pregnant women [22].

The Japanese work on ultrasound was relatively unknown in the United States and Europe until the 1950s. Then, Japanese researchers presented their results on the use of ultrasound for the detection of gallstones, breast masses, and tumors to the international medical community. Japan was also the first country to apply Doppler ultrasound, an application of ultrasound that detects moving objects that for example can be used for cardiovascular investigation [23].

1960–present Piezoelectric behavior of **p**oly**v**inylidene**d**i**f**luoride (PVDF), a polymer, has first been reported by Kawai in 1969. PVDF has a low acoustic impedance close to that of water and human body tissues. It is therefore successfully utilized for ultrasonic transducers for high resolution diagnostic imaging. PVDF transducers, however, have a lower sensitivity compared with conventional ceramic transducers, and a more sensitive piezoelectric polymer has been greatly desired. The copolymer **p**oly**v**inyli**d**ene**f**luoride **tr**i**f**luor**e**tylene P(VDF-TrFE) has been known to exhibit the highest coupling factor of all polymers investigated [25]. The first piezoelectric films were commercially available in 1980. In 1995 Ohigashi [26] first succeeded in preparing single crystalline films of P(VDF-TrFE).

In 1965 the first mechanical real-time scanner was developed by Krause *et al*. [27] and was used for imaging fetal life and motions. Improved real-time scanners were employed in cardiac scanners. In mechanical scanners a single element is translated or rotated mechanically to produce a 2D image. A typical example of a mechanical sector probe is shown in figure 1–8a. The transducer is housed in a dome and bathed in oil to facilitate the transmission of the ultrasonic energy from the transducer to the area being imaged. Electronic scanners consist of an array of transducer elements. A linear switched array is operated by applying voltage pulses to groups of elements in succession, as shown in figure 1–8b. In this way, the sound beam is moved across the face of the transducer electronically, producing a picture similar to that obtained by scanning a single transducer mechanically [28].

Around 1975, electronic scanners, which were more flexible, mobile, and more economical than the costly and bulky mechanical scanners, became available and were based on linear array transducers [29]. In the early 1980’s, the advancement in computer technology enabled more stable images and a greater versatility in image processing. Image quality of real-time ultrasound scanners made steady improvements during the mid 1980's to early 90's secondary to the increasing versatility and affordability in microprocessor technology. Nevertheless, it was not until the early to mid 1990's that more substantial enhancements in image quality were seen [30].

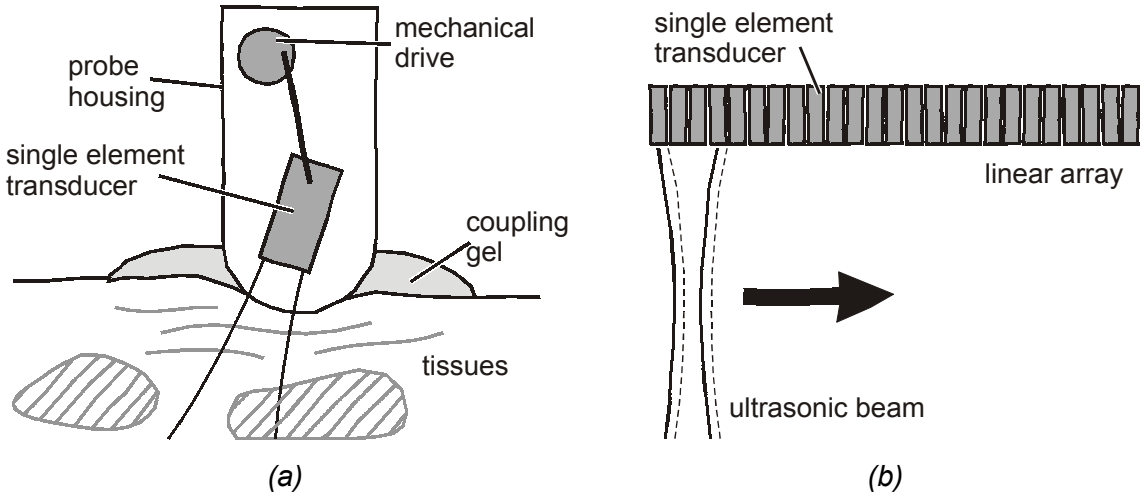

Figure 1–8 Construction of (a) a mechanical sector probe and (b) linear array in which a group of elements is excited simultaneously to form a sharper beam.

In 1989, Baba *et al.* [31] described an ultrasonic 3-D visualization system. An example of a 3-D image is shown in figure 1–9. Due to the explosive advancements in electronic and microprocessor technology in the 1990's the enhancement in diagnostic capabilities of scanners has enormously been propelled, resulting in, for example, diagnosis of embryos that are smaller than 10 mm.

Figure 1–9 A 3-D fetus image made with the Voluson 530D 3D System of Kretztechnik.

1.3 Outline of this thesis

In this thesis, a closed-loop spinal cord stimulation system is described, by which the measurement of the distance between the stimulation electrode array and the spinal cord is used to apply electrical pulses of appropriate amplitude to the spinal cord for the management of chronic pain. The method is based on the measurement of the time-of-flight of an ultrasonic pulse using a piezoelectric transducer. The emphasis of this study is upon the optimization of the piezoelectric transducer. A model of a piezoelectric transducer is presented in chapter 2, followed by a method to obtain the appropriate piezoelectric parameters for modeling the transducer. Different methods are applied to obtain the piezoelec-

tric parameters of ceramic and polymer materials, because the electrical and mechanical losses in these materials differ substantially.

The model presented in chapter 2 is used in chapter 3 to set design criteria for the transducer. In this chapter the characteristics of two transducer types are analyzed, particularly in relation to the signal-to-noise ratio. First, a hybrid transducer, consisting of a ceramic sender with on top a polymer receiver, also operating as a matching layer, is discussed. The sending capabilities of ceramic piezoelectric materials are superior to that of polymers, whereas piezoelectric polymers have superior receiving capabilities of ultrasound. Second, a multi-element transducer is proposed to improve the signal-to-noise ratio. A large piezoelectric element is divided into *n* smaller elements. In sending mode the elements are electronically connected in parallel, so they can be considered as one large element sending an excitation pulse. In receiving mode, all elements are connected in series, so the signals of the elements are added. Since the noise sources are incoherent and the signals are coherent the signal-to-noise ratio will be improved.

The measurement setup, presented in chapter 4, consists of a piezoelectric transducer connected to a function generator and an oscilloscope. The excitation pulse for pulse-echo experiments is a single sine wave. A spinal cord model is attached to a precision manipulator, by which the distance between the transducer and the spinal cord model can be varied. In chapter 5 experimental data on two different multi-element transducers are presented and compared to data on the single element transducers.

Two important issues are the detection of the echo during ringing of the transducer and the distinction of the echo from the background noise. Therefore, several signal processing methods for echo detection are presented in chapter 6. Two detection methods, i.e. matched filter and amplitude demodulation are discussed in more detail and their performance is compared. Finally, conclusions are drawn and recommendations for future research and development are given in chapter 7.

References

[1] P. Kellaway, "The part played by electric fish in the early history of bioelectricity and electrotherapy," *Bulletin of the history of medicine*, vol. 20, pp. 112-137, 1946.

[2] C.N. Shealy, J.T. Mortimer, and J.B. Reswick, "Electrical inhibition of pain by stimulation of the dorsal columns," *Anesthesia and analgesia: current researches*, vol. 46, pp. 489-491, 1967.

[3] W.A. Wesselink, "Computer Aided Analysis of Spinal Cord Stimulation." PhD Thesis, University of Twente, 1998.

[4] B.A. Simpson, "Spinal cord stimulation," *Pain Reviews*, vol. 1, pp. 199-230, 1994.

[5] R. Melzack and P.D. Wall, "Pain mechanisms: a new theory," *Science*, vol. 150, pp. 971-979, 1965.

[6] G. Barolat, "Current Status of Epidural Spinal Cord Stimulation," *Neurosurgery Quaterly*, vol. 5, no. 2, pp. 98-124, 1995.

[7] J. Holsheimer, J.A. Den Boer, J.J. Struijk, and A.R. Rozeboom, "MR Assessment of the Normal Position of the Spinal Cord in the Spinal Canal," *American Journal of Neuroradiology*, vol. 15, pp. 951-959, 1994.

[8] J. He, G. Barolat, and B. Ketcik, "Stimulation Usage Range for Chronic Pain Management," *Analgesia*, vol. 1, no. 1, pp. 75-80, 1994.

[9] J. Holsheimer and G. Barolat, "Significance of the Spinal Cord Position in Spinal Cord Stimulation," *Acta neurochirurgica [supplementum]*, vol. 64, pp. 119-124, 1995.

[10] E.A. Dijkstra, "Ultrasonic Distance Detection in an Epidural Spinal Cord Stimulation System." MSc Thesis, University of Twente, 1995.

[11] W. Starkebaum, and M.T. Rise, Ultrasonic Techniques for Neurostimulator Control. Medtronic, Inc. 627,574[5,628,317]. 1997. Minnesota,USA.
Ref Type: Patent

[12] G. Kossoff, "The Effects of Backing and Matching on the Performance of Piezoelectric ceramic Transducers," *IEEE transactions on sonics and ultrasonics*, vol. SU-13, pp. 20-30, 1966.

[13] C.S. Desilets and J.D. Fraser, "The Design of Efficient Broad-Band Piezoelectric Transducers," *IEEE transactions on sonics and ultrasonics*, vol. SU-25, no. 3, pp. 115-125, 1978.

[14] P.N.T. Wells, *Ultrasonics in Clinical Diagnosis* Edinburg: Churchill Livingstone, 1977.

[15] T.R. Gururaja, "Piezoelectrics for Medical Ultrasonic Imaging," *American Ceramic Society bulletin*, vol. 73, no. 5, pp. 50-55, 1994.

[16] Piezoelectric Effect. Microsoft Encarta 98 Encyclopedia . 1993. Microsoft Corporation.
Ref Type: Electronic Citation

[17] J. Curie and P. Curie, "Développement par pression de l'électricite polaire dans les cristaux hémièdres à faces inclinées," *Comptes Rendus de l'Academie des Sciences*, vol. 91, pp. 294, 1880.

[18] A History of Piezoelectricity.
Ref Type: Internet Communication

[19] M.E. Lines and A.M. Glass, *Principles and Applications of Ferroelectrics and Related Materials* Oxford: Clarendon Press, 1977.

[20] W.D. O'Brien, "Assessing the Risks for Modern Diagnostic Ultrasound Imaging," *Japanese journal of applied physics*, vol. 37, pp. 2781-2788, 1998.

[21] K.T. Dussik, "Uber die moglichkeit hochfrequente mechanische schwingungen als diagnostisches hilfsmittel zu verwerten," *Z. Neurol. Psychiat.*, pp. 174-153, 1942.

[22] I. Donald and J. MacVicar, "Investigation of abdominal masses by pulsed ultrasound," *Lancet*, vol. 1, pp. 1188-1195, 1958.

[23] History of Diagnostic Ultrasound.
Ref Type: Internet Communication

[24] S. Levi, "The history of ultrasound in gynecology 1950-1980," *Ultrasound in Medicine & Biology*, vol. 23, no. 4, pp. 481-552, 1997.

[25] H. Ohigashi and K. Koga, "Ferroelectric Copolymers of Vinylidenefluoride and Trifluoroethylene with a Large Electromechanical Coupling Factor," *Japanese journal of applied physics*, vol. 21, pp. L455-L457, 1982.

[26] H. Ohigashi and K. Omote, "Formation of "single crystalline films" of ferroelectric copolymers of vinylidene fluoride and trifluoroethylene," *Applied physics letters*, vol. 66, pp. 3281-3283, 1995.

[27] W. Krause and R. Soldner, "Ultrasonic imaging technique (B scan) with high image rate for medical diagnosis," *Electromedica*, vol. 4, pp. 1-5, 1967.

[28] K.K. Shung and M. Zipparo, "Ultrasonic Transducers and Arrays," *IEEE engineering in medicine and biology magazine*, vol. 15, no. 6, pp. 20-30, 1996.

[29] F.S. Foster, "Transducer materials and probe construction," *Ultrasound in Medicine & Biology*, vol. 26, no. 1, pp. S2-S5, May2000.

[30] Woo, J., A short History of the developments of Ultrasound in Obstetrics and Gynecology.
Ref Type: Internet Communication

[31] K. Baba and K. Satch, "Development of an Ultrasonic System for Three-Dimensional Reconstruction of the Fetus," *Journal of perinatal medicine*, vol. 17, pp. 19-24, 1989.

Chapter 2

Modeling and evaluation of a piezoelectric transducer

2.1 Introduction

Several equivalent circuits for piezoelectric transducers have been presented in the past. Van Dyke [1] showed already in 1925 that a series resonant circuit shunted by a capacitor is the electrical equivalent of a two electrode piezoelectric resonator. He was able to relate the electrical parameters of the equivalent circuit to the physical properties of a piezoelectric crystal. The traditional Van Dyke's circuit model is depicted in figure 2–1. In this circuit, the components are traditional real capacitors, resistors and inductors. In the circuit, the capacitance C_0 represents the electrical capacitance of the transducer, while L_m, R_m, and C_m are chosen to provide a resonant frequency and a Q-factor numerically equal to that of the mechanical resonance of the transducer. This model cannot be applied to describe a resonator far from the center of the fundamental resonance peak, and it does not work well for lossy resonators.

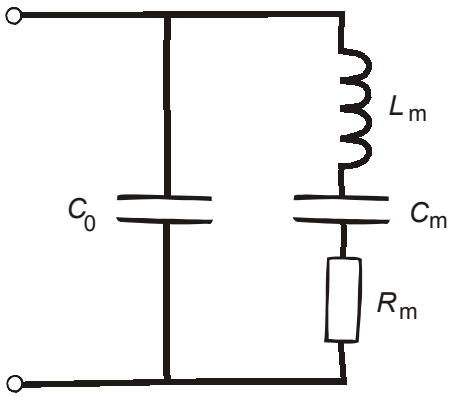

Figure 2–1 *Van Dyke's circuit model [1]. C_0 represents the electrical capacitance of the transducer, and L_m, R_m, and C_m are chosen to provide a resonant frequency and a Q-factor numerically equal to that of the mechanical resonance of the transducer.*

Mason [2] derived a lumped-element equivalent circuit for 1-dimensional analysis of piezoelectric transducers. Mason's model for a thickness mode transducer is shown in figure 2–2 and consists of a negative capacitance and a transformer. *V* and *I* represent the electrical input voltage and current, respectively. The voltages F_1 and F_2 represent the acoustical signals at the left and right side of the piezoelectric element. Redwood [3] altered Mason's thickness expander plate into a circuit that contains an acoustic transmission line. However, this alteration does not appreciably simplify the circuit.

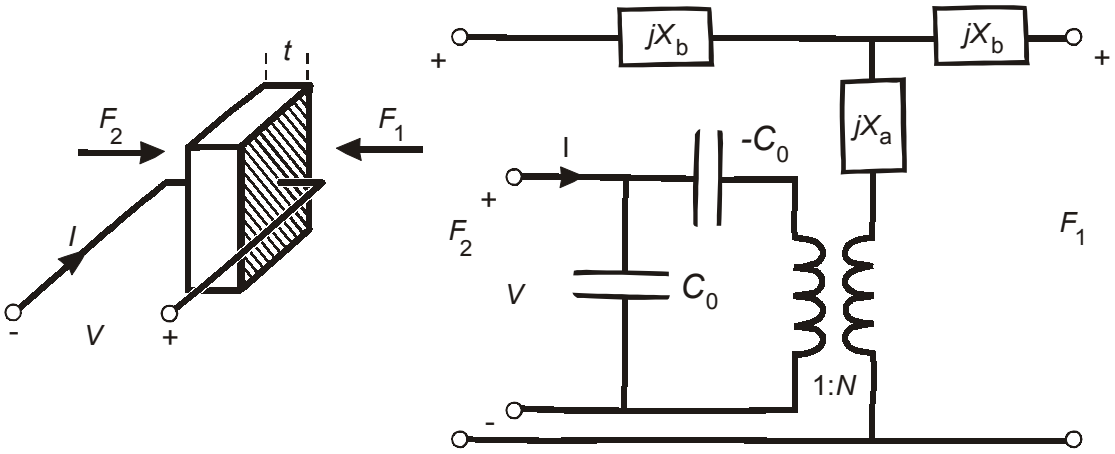

Figure 2–2 *Mason's model [2] for a thickness mode resonator. $C_0 = A/t\beta_{33}^{S}$, A = transducer area, t=transducer thickness, β_{33}^{S}=impermeability, $N = C_0 h_{33}$, h_{33}=piezoelectric constant, $X_a = Z_0 \operatorname{cosec}(t\omega/v_p)$, $Z_0 = A\rho v_p$, v_p=acoustic wave velocity, ρ=density, $X_b = Z_0 \tan(t\omega/2v_p)$, ω = angular frequency.*

Krimholtz *et al.* [4] used a similar equivalent circuit, the KLM[1] model shown in figure 2–3, but this one differs in a more fundamental way from Mason's model.

[1] named after the inventors: Krimholtz, Leedom and Matthaei

The electrical and mechanical parts of the transducer are clearly distinguished in the circuit. In addition, the KLM model facilitates the calculation of electrical input impedance for an arbitrary acoustic load. The KLM model and its parameters will be discussed in more detail in subsection 2.2.1.

Several methods have been presented for calculating the time response of a transducer. Sittig [5] employed matrix techniques for the analysis of transducer structures. Hayward [6] applied the *z*-transform for modeling thickness mode transducers. Capineri [7] proposed an analytical model in the Laplace *s*-domain, in which the transducer is considered as a black-box, characterized by two analytical functions representing the driving point impedance and the electroacoustic transfer function. These methods are rather laborious since the introduction of schematic editors that allow designing networks in a visual environment, e.g. PSpice. Hutchens [8] developed Schwarz's [9] transmission line model for use in SPICE II. This simulated transmission line can be made exactly equivalent to an actual transmission line at one frequency only. This disadvantage was overcome by Morris [10] who implemented Redwood's model in Spice. Leach [11] presented a transmission line analogous circuit, which employs controlled sources to model the coupling between the electrical and the mechanical part. Püttmer [12] included mechanical losses in a Spice model to provide modeling of lossy piezoceramic transducers. The previously mentioned models were used only for the simulation of the piezoelectric element. Maione [13] presented a PSpice implementation of a transducer model, including electrical and acoustical matching and a focusing lens. The ultrasound transducer model was based on Redwood's version of Mason's equivalent circuit. The acoustical lens was modeled by a lossy transmission line [12] because it had significant acoustical losses.

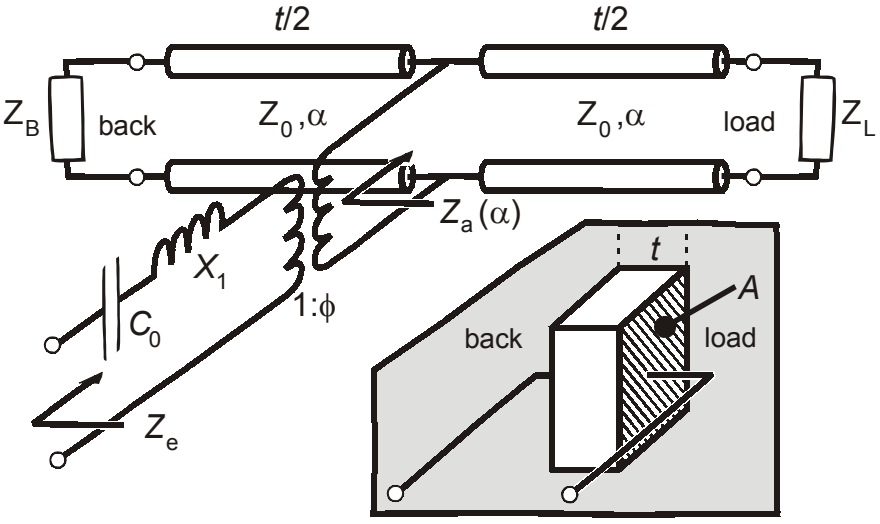

Figure 2–3 KLM model for a thickness mode resonator [4], A=transducer area, t=transducer thickness, Z_0=acoustical impedance of transducer, α=attenuation constant, Z_B=backing impedance, Z_L=load impedance, Φ=transform ratio, C_0=clamped capacitance, X_1=inductance.

Irrespective of their functional realization, most transducer models are primarily confined to the frequency domain, implying that the governing differential equations for a particular configuration are solved by the application of frequency transformation techniques in order to obtain a transfer function of the system. However, many transducer applications require a detailed knowledge of the transient response characteristics [6]. Consequently, interest is focused on the time domain and hence a transformation from frequency to time is required. This may be achieved by applying an inverse Fourier transform on the output signal.

In the next section the modified KLM model, used to simulate lossy piezoelectric transducers more accurately, is presented. In order to accurately model a single piezoelectric element it is necessary to acquire the appropriate parameters. These parameters are obtained from a simple impedance measurement. The method used to obtain a first (rough) estimate of the piezoelectric parameter values is presented in section 2.3. Section 2.4 contains results of the parameter estimation. A distinction is drawn between ceramic and polymer transducers, because these two materials differ greatly in mechanical and electrical losses. Finally, measured and calculated data of a ceramic (PXE-5, a Philips grade) transducer are compared in section 2.5.

2.2 Transducer modeling

The KLM model [4] was modified to improve its performance, i.e. reduce the discrepancy between calculated and measured data. Subsequently, the modified KLM model was implemented in the simulation tool APLAC [14]. In conjunction with the modified KLM model a model for calculating the insertion loss and pulse-echo response are discussed in subsection 2.2.3.

2.2.1 The KLM model for a thickness mode transducer

The KLM model (figure 2–3) provides a powerful tool for analysis and simulation of a piezoelectric transducer element. However, the standard KLM model only allows modeling of mechanical losses in the transmission line through an attenuation coefficient a. Dielectric losses are not included in the standard model. First, the standard model and its equations will be presented [4]. Subsequently, in subsection 2.2.2 the standard model is expanded to include dielectric losses.

A piezoelectric transducer with a thickness t [m] and an area A [m^2] is considered. The acoustic impedance Z_0 [kg/s] of the transducer is the product of its area, the density ρ [kg/m^3] and the sound velocity v_p [m/s]:

$$Z_0 = A\rho v_p \qquad (2\text{–}1)$$

The impedances Z_B and Z_L correspond to the acoustic impedance of the back and load of the transducer and can be written similarly to equation (2–1):

$$\begin{aligned} Z_B &= A\rho_B v_B \\ Z_L &= A\rho_L v_L \end{aligned} \tag{2–2}$$

where ρ and v correspond to the density of and sound velocity in the back and load. The clamped capacitance C_0 can be written as:

$$C_0 = \frac{\varepsilon_0 \varepsilon^S A}{t} \tag{2–3}$$

where ε_0 is the permittivity of free space ($8.854 \cdot 10^{-12}$ [F/m]) and ε^S the clamped relative permittivity [-]. The inductance X_1 is:

$$X_1 = Z_0 M^2 \sin\left(\frac{t\omega}{v_p}\right) \tag{2–4}$$

where ω is the angular frequency [rad/s] and M is given by:

$$M = \frac{h_{33}}{\omega Z_0} \tag{2–5}$$

where h_{33} is a piezoelectric constant [V/m] that can be expressed as:

$$h_{33} = k_t \sqrt{\frac{c_{33}^D}{\varepsilon_0 \varepsilon^S}} \tag{2–6}$$

where c_{33}^D is the elastic stiffness constant [N/m^2], and k_t the thickness coupling factor [-]. The transform ratio Φ is:

$$\Phi = \frac{1}{2M} \sin^{-1}\left(\frac{t\omega}{2v_p}\right) \tag{2–7}$$

The input impedance at the electrical port of the KLM model (figure 2–3) Z_e can be written as:

$$Z_e = \frac{1}{j\omega C_0} + jX_1 + \frac{Z_a(a)}{\Phi^2} \tag{2–8}$$

where $Z_a(a)$ is the input impedance of the transmission line, and a is the attenuation coefficient [Np/m][2] of the transmission line.

2.2.2 The modified KLM model

The KLM model (figure 2–3) will be modified to provide modeling of both mechanical and dielectric losses, because these losses play an important role in piezopolymer transducers. A lossy transmission line and a complex elastic stiffness

[2] The attenuation is mostly given in [dB/mm]; to obtain the SI unit [Np/m] multiply by 1000 and divide by 20 log(e) (1 Np=8.686 dB).

c_{33}^{D*} are used to model the mechanical losses, whereas the dielectric loss is modeled by a complex dielectric constant ε^{S*}:

$$c_{33}^{D*} = c_{33}^{D}(1 + j\tan\delta_m) \tag{2–9}$$

$$\varepsilon^{S*} = \varepsilon^{S}(1 - j\tan\delta_e) \tag{2–10}$$

where tan δ_m and tan δ_e are the mechanical and dielectric loss tangent, respectively. The minus sign in equation (2–10) is a result of the complex impedance of a capacitor that is inversely proportional to the dielectric constant. The loss can then be represented by a resistor as will be shown below. Consequently, the equations (2–3) through (2–7) will become complex, resulting in a complex capacitance C_0 and inductance X_1, C_0' and X_1', respectively.

The modified KLM model as shown in figure 2–4 was implemented in APLAC [14], an object-oriented analog circuit simulation and design tool that allows modeling of frequency dependent component values, e.g. $R'=R(\omega)$ where ω is the angular frequency. This is required to model losses, since APLAC does not allow complex values for capacitors and inductors.

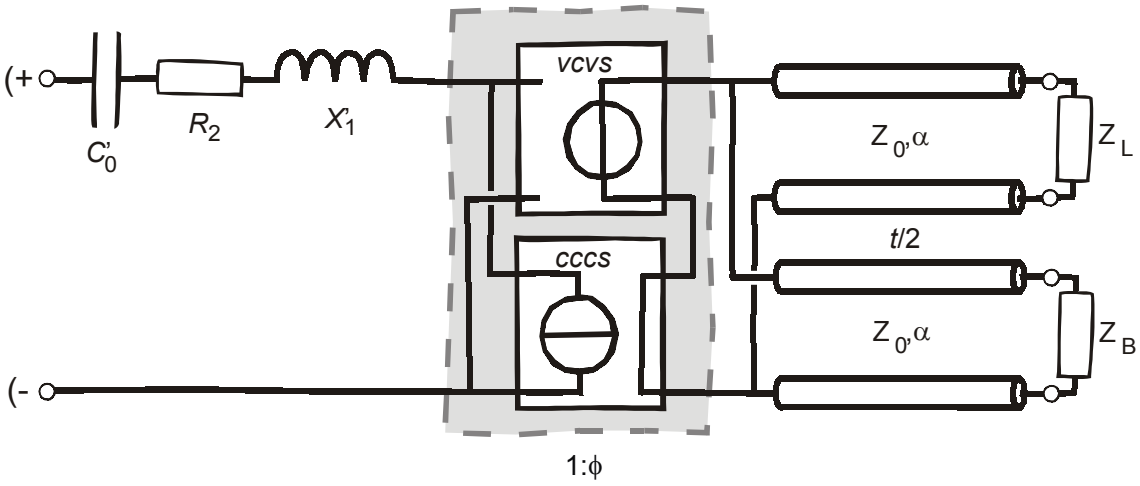

Figure 2–4 The modified KLM model as implemented in APLAC.

The impedance of the capacitance C_0 can be written as:

$$\frac{1}{j\omega C_0} = \mathrm{Re}\left\{\frac{1}{j\omega C_0}\right\} + j\,\mathrm{Im}\left\{\frac{1}{j\omega C_0}\right\} \tag{2–11}$$

and the impedance of the inductance X_1 can be written as:

$$jX_1 = \mathrm{Re}\{jX_1\} + j\,\mathrm{Im}\{jX_1\} \tag{2–12}$$

The resistor R_2 models the dielectric and mechanical losses in C_0 and X_1 of figure 2–3. R_2 can be written as sum of the real parts of the impedances of the capacitance C_0 (2–11) and inductance X_1 (2–12):

$$R_2 = \mathrm{Re}\left\{\frac{1}{j\omega C_0}\right\} + \mathrm{Re}\{jX_1\} \tag{2–13}$$

The admittance X_1' in figure 2–4 can be expressed as:

$$X_1' = \mathrm{Im}\{jX_1\} \tag{2–14}$$

The impedance of C_0' is equal to the imaginary part of equation (2–11):

$$\frac{1}{j\omega C_0'} = j\,\mathrm{Im}\left\{\frac{1}{j\omega C_0}\right\} \tag{2–15}$$

from which the following expression C_0' can be derived:

$$C'_0 = \left(-\mathrm{Im}\{C_0^{-1}\}\right)^{-1} \tag{2–16}$$

The transform ratio Φ is complex and because APLAC does not accept a complex transform ratio for a transformer it is modeled by two controlled sources. The currents through the primary (I_p) and secondary (I_s) side of a transformer with a transform ratio 1:Φ hold the following relationship:

$$I_p = \Phi I_s \tag{2–17}$$

whereas the voltages across the primary (V_p) and secondary (V_s) side of a transformer are related as:

$$V_s = \Phi V_p \tag{2–18}$$

This allows the modeling of the transformer by a *current-controlled-current-source* (*cccs*) and a *voltage-controlled-voltage-source* (*vcvs*), as shown in figure 2–4. In this case, Φ is allowed to be complex.

2.2.3 The transfer function, transient analysis and insertion loss

It is often easier to calculate the transfer function $H(\omega)$ of a system (frequency domain) than the transient response (time domain). However, once the transfer function is known the transient response can be calculated by applying the inverse Fourier transform. Figure 2–5 shows an arbitrary *network* connected to a voltage source with an internal resistance R_S. When V_S is the input voltage and V_{out} is the voltage of interest, the transfer function $H(\omega)$ of the system, including the source resistance R_S, is defined as:

$$H(\omega) = V_{out}(\omega) / V_S(\omega) \tag{2–19}$$

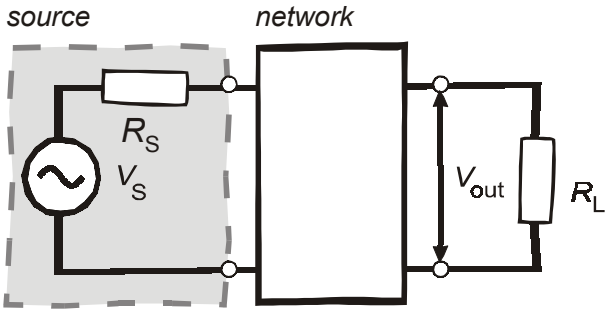

Figure 2–5 Arbitrary network with a voltage source for calculating the transfer function.

Now it is possible to calculate the time response of V_{out} by using the Fourier transform:

$$V_{out}(t) = F^{-1}\{H(\omega)F\{V_S(t)\}\} \tag{2–20}$$

where $F\{\ldots\}$ denotes the Fourier transform, and $F^{-1}\{\ldots\}$ the inverse transform.

In order to describe the performance of the network, the insertion loss –abbreviated by *IL*– of a network as shown in figure 2–5, is introduced. *IL* can be calculated as follows. The power delivered by the *source* having an internal resistance R_S, with the *network* inserted into a load R_L is P_i. With the *network* removed, the load R_L is directly connected to the *source* and the power delivered to the load is P_r. The power P_i can be written as:

$$P_i = \left(\frac{R_L}{R_L + R_S} V_S\right)^2 \frac{1}{R_L} \tag{2–21}$$

and the power P_r as:

$$P_r = (V_{out})^2 \frac{1}{R_L} \tag{2–22}$$

It is customary to define *IL* expressed in dB as [15]:

$$IL = 10\log\left(\frac{P_i}{P_r}\right) = 20\log\left|\frac{R_L + R_S}{R_L}\frac{V_{out}}{V_S}\right| \quad \text{dB} \tag{2–23}$$

and, in particular, for the case where R_S=R_L (usually 50 Ω):

$$IL = 20\log|2H(\omega)| \quad \text{dB} \tag{2–24}$$

Now that the definitions of the transfer function, pulse-echo response and insertion loss are given they must be applied to the piezoelectric transducer model. Figure 2–6(a) shows a transducer emitting a pulse that travels through a loss-less medium and is reflected by a perfect reflector. In this setup it is complicated to calculate the insertion loss from a simulation, because the voltage of interest (V_{out}) must be distinguished from the excitation voltage at the same node. Therefore, an equivalent setup is shown in figure 2–6(b). The left transducer emits an ultrasonic wave. The ultrasound travels through the loss-less delay medium before being detected by the (same) transducer, shown on the right side. This assumes that the ultrasound pulse has returned from a perfect reflector. In both cases the transducer receives the same amount of power. Now the voltage of interest (V_{out}) is clearly separated from the excitation voltage.

Figure 2–7 shows a simplified equivalent electrical circuit of figure 2–6b, where the KLM circuit has been replaced by a two port network in which the voltage V_L appears across the load Z_L. The input terminals of the right transducer are at the medium/load side whereas the voltage of interest V_{out} appears across a termination load R_L. It should be noted that the incoming ultrasonic signal is represented by a voltage source of $2V_L$. This maximum power transfer can only be achieved when the power received by the right transducer is equal to the power emitted

into the medium by the left transducer. This maximum emitted power (V_L^2/Z_L) can only be received by the input terminals of the receiving transducer when the input impedance (at the input terminals) of the right transducer is equal to Z_L, and the source representing the incoming ultrasound signal has a value of $2V_L$ [16].

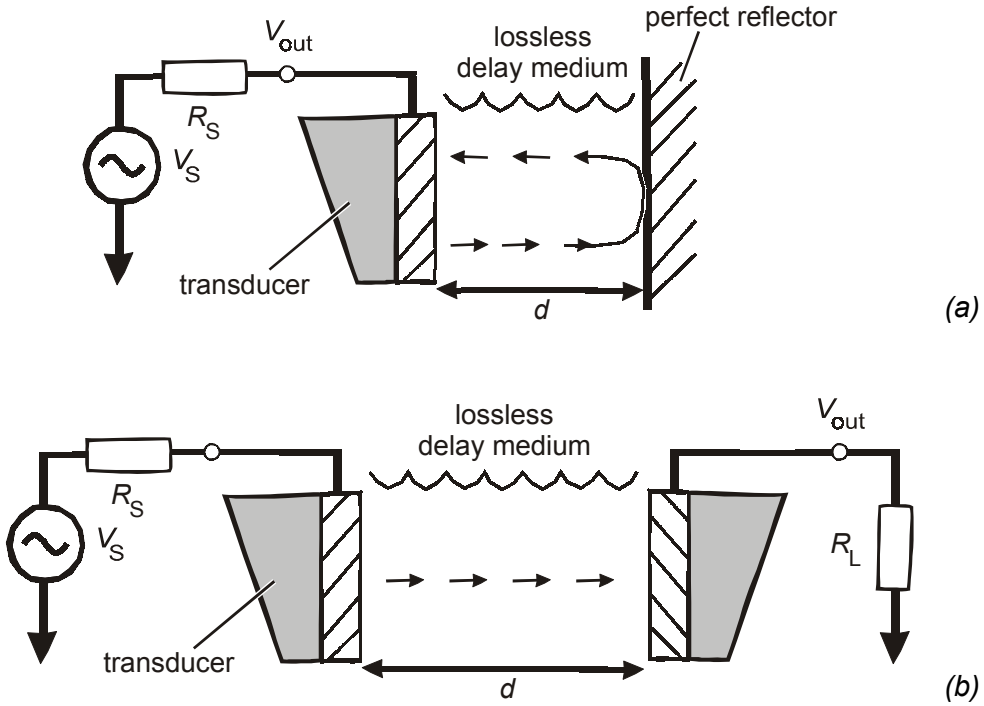

Figure 2–6 *Two situations where a transducer receives an equal amount of power: (a) a transducer emits a pulse through a loss-less medium that is reflected by a perfect reflector and is received by the same transducer and (b) the left transducer emits a pulse that is received by an identical transducer on the right side.*

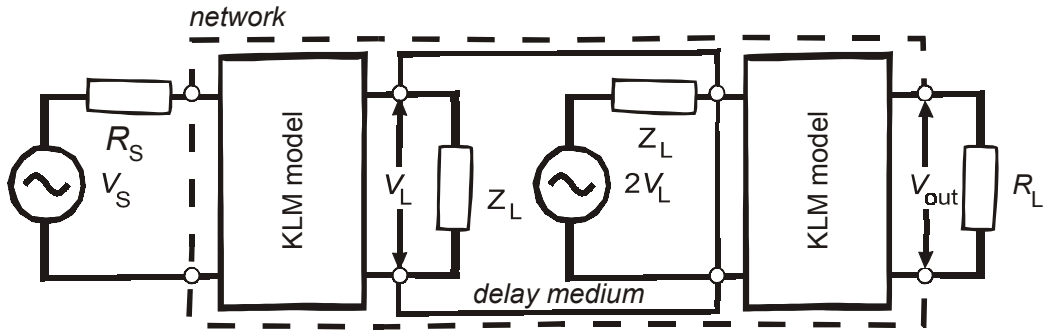

Figure 2–7 *Circuit for calculating the transfer function of a pulse-echo system.*

2.3 Transducer parameter extraction method

The material parameter values used in the KLM model can be estimated from an electrical impedance measurement. These measurements were made for both ceramic and polymer piezoelectric transducers, because polymers exhibit high

internal losses, whereas such losses are negligible in ceramics. For optimal modeling of the PVDF foil, smooth curves were experimentally obtained for the dielectric constant ε^S and the dielectric loss tangent tan δ_e. Due to the high internal losses in polymers, length and width resonances are unimportant, in contrast to ceramics, where these resonances are clearly observed. Therefore, the length and width of the ceramic transducer should be much larger than its thickness to reduce the resonances other then the first order thickness resonance. Impedance spectra are measured, from which material parameters are derived. The measured parallel and series resonance frequencies are important quantities for parameter evaluation. Different resonance frequencies will be discussed in the next subsection. The material parameters are obtained by a combination of the methods presented by Foster *et al.* [17], Ih *et al.* [18], the IEEE Std 176 [19], and Kwok *et al.* [20].

The transducer will be used at its first resonance, because this is the strongest resonance frequency of a piezoelectric transducer, and therefore the conversion from electrical to mechanical energy, and vice versa, has the highest efficiency. For a biomedical application two important parameters are: the penetration depth of the ultrasonic wave and the required spatial resolution, which was already mentioned in subsection 1.1.4. The penetration depth decreases with increasing frequency, because the attenuation of acoustic waves in water-like substances is proportional to the squared frequency [21]. The measurement resolution increases linearly with frequency. Therefore, a trade-off should to be made for the appropriate frequency, i.e. that the required resolution (0.5 mm) is met at the maximum penetration depth (10 mm).

2.3.1 Resonance frequency definitions

The different resonance frequencies of a piezoelectric transducer are important for parameter estimation. Before the six resonance frequencies discussed in this section are treated, the electrical input impedance of the transducer will be discussed, since the resonance frequencies are obtained from the impedance curves. The impedance Z can be written as the sum of the resistance R and the reactance X:

$$Z = R + jX \tag{2–25}$$

and the admittance Y as the sum of the conductance G and the susceptance B:

$$Y = G + jB \tag{2–26}$$

The relationship between the impedance Z and the admittance Y is:

$$Y = \frac{1}{Z} \tag{2–27}$$

Expressions can be found for the conductance G and susceptance B by substituting equations (2–25) and (2–26) into equation (2–27):

$$G = \frac{R}{|Z|^2}$$
$$B = \frac{-X}{|Z|^2} \qquad (2\text{–}28)$$

where $|Z|$ is the magnitude of Z. In table 2–1 the definitions of six resonance frequencies are listed. The frequency differences are related as follows [22]:

$$(f_m - f_n) > (f_p - f_s) > (f_a - f_r) \qquad (2\text{–}29)$$

For piezoelectric ceramics with high coupling factors and reasonably low dielectric loss factors, these three frequency differences are nearly equal. As an example, the simulated magnitude of the impedance Z of a ceramic transducer is shown in figure 2–8. The frequencies at maximum (f_m) and minimum (f_n) impedance can be obtained from the top figure. The parallel (f_p) and series (f_s) resonances are obtained from the resistance and conductance curves and are shown in figure 2–8 as well (bottom). The resonance (f_r) and anti-resonance (f_a) frequencies, obtained from the reactance and susceptance curves, are –in this case– nearly equal to the parallel and series resonance frequencies.

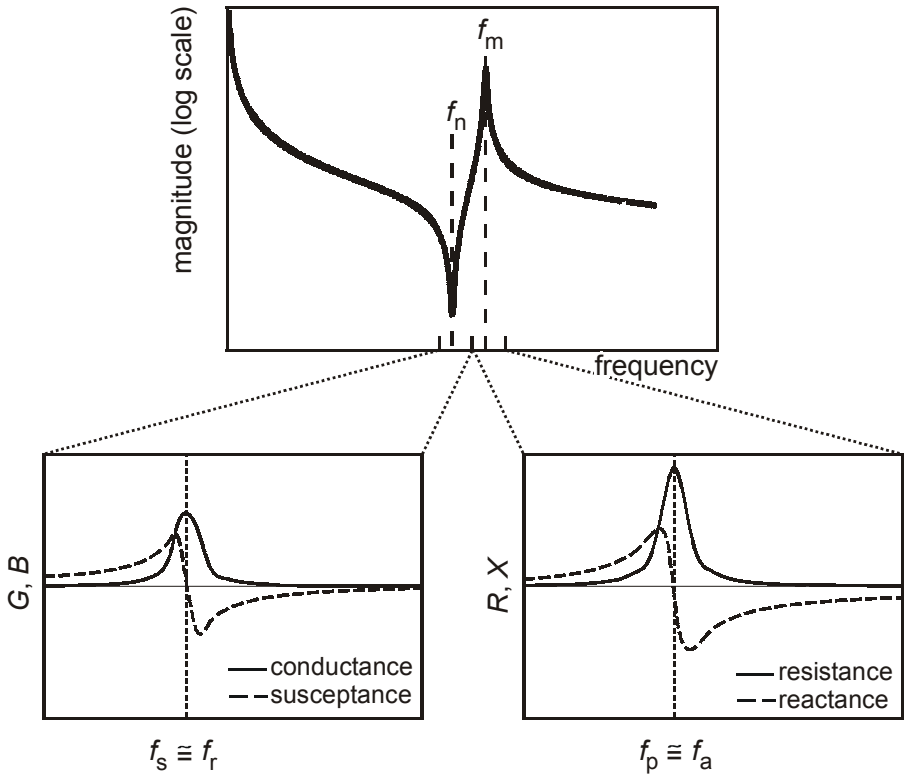

Figure 2–8 Resonance frequency definitions: frequency at maximum impedance (f_m), frequency at minimum impedance (f_n), frequency at maximum resistance (f_p), frequency at maximum conductance (f_s), anti-resonance frequency (f_a, zero reactance), and resonance frequency (f_r, zero susceptance). The curves are obtained from a simulation of a piezoelectric ceramic.

Table 2–1 Resonance frequencies definitions.

parameter	definition
f_m	frequency at maximum impedance
f_n	frequency at minimum impedance
f_p	frequency at maximum resistance
f_s	frequency at maximum conductance
f_a	anti-resonance frequency (zero reactance)
f_r	resonance frequency (zero susceptance)

2.3.2 Coupling coefficients and mechanical losses

The thickness mode coupling coefficient k_t and the mechanical losses of the piezoelectric material are critical factors in determining transducer performance [17]. The method most often used to determine k_t requires only the determination of the series f_s and parallel f_p resonance frequencies:

$$k_t = \frac{\pi}{2}\frac{f_s}{f_p}\tan\left(\frac{\pi}{2}\frac{f_p - f_s}{f_p}\right) \tag{2–30}$$

This method can introduce errors when applied to materials with high dielectric and mechanical losses [17]. Therefore, an additional optimization step is required for optimal parameter estimation. The optimization step consists of matching the measured and simulated electrical input impedance of a transducer by varying some model parameters and will be explained in section 2.4.3. First, the method to obtain the material parameters of a piezoelectric material with low losses is described [17-19].

For an air-resonator the parallel resonance frequency f_p is:

$$f_p = \frac{v_p}{2t} \tag{2–31}$$

where v_p is the sound velocity [m/s] and t the transducer thickness [m]. The elastic stiffness constant c_{33}^D [N/m^2] is given by:

$$c_{33}^D = v_p^2 \rho \tag{2–32}$$

To calculate c_{33}^D from f_p (obtained from an impedance measurement) equation (2–31) is substituted into the equation (2–32):

$$c_{33}^D = 4\rho(f_p t)^2 \tag{2–33}$$

The sound velocity v_p in the piezoelectric material can be computed by rewriting equation (2–32) into:

$$v_p = \sqrt{c_{33}^D / \rho} \tag{2–34}$$

The mechanical losses of the material have been incorporated into the KLM model via an effective attenuation coefficient a, which is computed by the method of Bui *et al.* [23]. This approach has the advantage that it is independent of k_t. The attenuation coefficient can be obtained in terms of the maximum input resistance and some other parameters that can easily be determined by an electrical impedance measurement [18]. Subtracting the effect of the bulk capacitance from the measured electrical impedance Z_e as stated in equation (2–8) gives:

$$Z_e' = Z_e - \frac{1}{j\omega C_0} = jX_1 + \frac{Z_a(a)}{\Phi^2} \tag{2–35}$$

It has been shown [23] that for small at, the ratio of the imaginary (X) to real (R) components of Z_e' near the resonance is given by:

$$\frac{X}{R} \cong -\frac{\pi}{at}\left(\frac{f}{f_a} - 1\right) \tag{2–36}$$

where f is the frequency and f_a the anti-resonant frequency (zero reactance). The slope of an X/R versus f/f_a plot is thus inversely proportional to the attenuation coefficient. The attenuation coefficient a can be converted to a more commonly reported mechanical quality factor Q_m via the expression:

$$Q_m = \frac{\omega}{2v_p a} \tag{2–37}$$

where a is in Np/m.

2.3.3 Dielectric loss tangent and dielectric constants

The dielectric loss tangent $\tan \delta_e$ can be calculated from:

$$\tan \delta_e = \frac{1}{|\tan\theta|} \tag{2–38}$$

where θ is the phase of the measured impedance. Since a piezoelectric material behaves as a capacitor in frequency ranges away from resonance, the magnitude of the relative dielectric constant ε^S may be calculated, using equation (2–3) and (2–10), from:

$$\varepsilon^S = \frac{t}{\omega |Z| \varepsilon_0 A\sqrt{1 + (\tan\delta_e)^2}} \tag{2–39}$$

where $|Z|$ is the measured impedance magnitude. The dielectric constant ε^S is determined by averaging $|Z|$ over a range of frequencies in the slowly varying region between the first and second harmonic. The loss tangent $\tan \delta_e$ is computed by averaging over the same frequency range as the dielectric constant.

The equations in this section are used to extract the parameters from an electrical input impedance measurement of a piezoelectric transducer.

2.4 Transducer parameter estimation

2.4.1 Electrical impedance measurements

From an electrical impedance measurement, using an HP 4192A Impedance/-Gain-Phase Analyzer with an HP 16047D test fixture, all required transducer parameters were obtained. A photograph of the PVDF transducer including connecting wires is shown in figure 2–9. Two wires, one at each electrode, are attached to the piezoelectric element. The influence of the wire impedance was compensated for by subtracting its value from the total measured impedance.

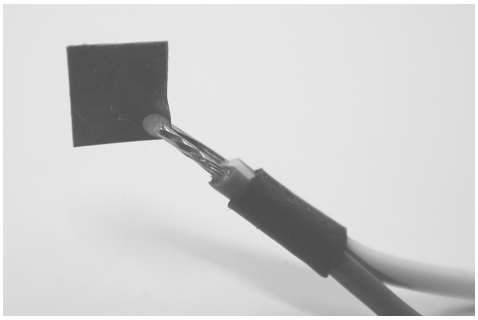

Figure 2–9 Photo of the PVDF transducer with two connecting wires.

The parameter estimation and KLM model verification are performed both for a ceramic (PXE-5, a Philips grade) and a polymer (PVDF, Kynar® AMP) transducer. In the next two subsections, the required material parameters will be deduced from input impedance measurements.

2.4.2 Parameter estimation of a PXE-5 transducer

The method presented in section 2.3 was used to obtain the model parameters. To obtain the PXE-5 material parameters it is necessary to use a sample of which the width and the length are much larger than the thickness, so width and length resonances do not influence the first thickness resonance. A PXE-5 sample with area A=2 cm × 2 cm, thickness t=0.3 mm, and density ρ=7800 kg/m^3 was used to obtain the material parameters. The following 3-step procedure was used to obtain accurate model parameters:

1. The electrical input impedance of the transducer is measured and compensated for the wire and contact impedance. Subsequently, the piezoelectric parameters are obtained using the method provided in section 2.3.
2. The obtained parameters are applied to the APLAC model. Subsequently, an optimization step is performed over a wide frequency range (varying ε^S, $\tan\delta_e$, k_t, Q_m and c_{33}^D) using the *downhill simplex method* according to Nelder and Mead that is implemented in APLAC [14]. During the optimization the real and imaginary parts of the input impedance are fitted. Similar methods were used by Kwok *et al.* [20] and Smits [24].

3. A similar optimization step is performed with the same parameters near the first resonance frequency.

The magnitude (solid line) and phase (dashed line) of the measured impedance are shown in figure 2–10. Three thickness resonance frequencies can be distinguished: the first one around 7 MHz, the second around 23.5 MHz and the third one at the right end at 39.5 MHz. Since the frequency range around the first resonance (6-9 MHz) contains the most relevant data for determining the material parameters, this part is magnified, as shown in figure 2–11. It shows: (a) conductance *G* and susceptance *B*, (b) magnitude *Z*, and (c) resistance *R* and reactance *X*. The different resonance frequencies can be found as explained in subsection 2.3.1.

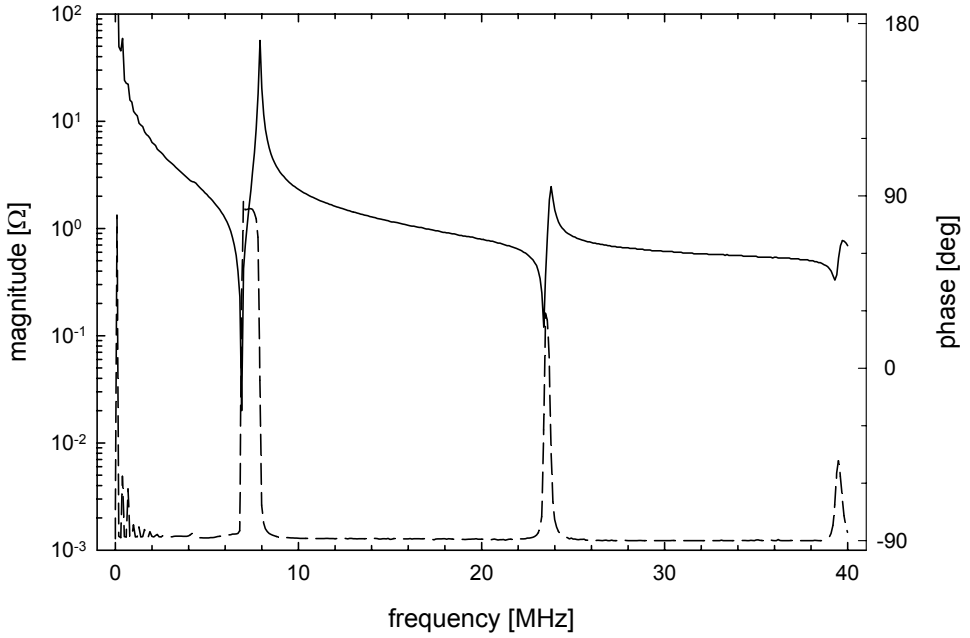

Figure 2–10 Measured impedance magnitude (solid line) and phase (dashed line) of a 0.3 mm thick PXE-5 transducer with an area of 2 cm × 2 cm.

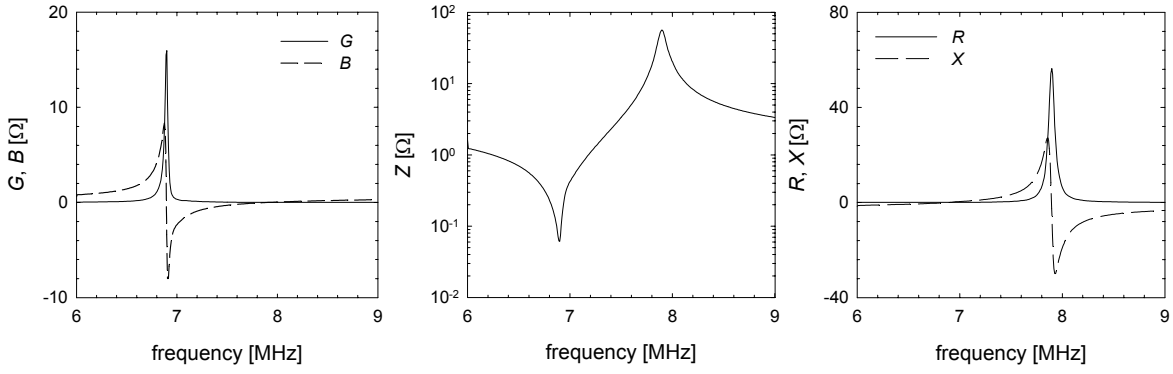

Figure 2–11 Measured: (a) conductance G and susceptance B, (b) magnitude Z, and (c) resistance R and reactance X of a 0.3 mm thick PXE-5 transducer with an area of 2 cm × 2 cm.

Now step 1, to find a first approximation of the material parameters, can be carried out. Substituting the observed parallel (f_p=6.90 MHz) and series (f_s= 7.91 MHz) resonance in equation (2–30) gives a coupling coefficient k_t of 0.53. The elastic stiffness constant c_{33}^D is calculated using equation (2–33) resulting in a value of $1.758 \cdot 10^{11}$ N/m^2. The sound velocity v_p in the piezoelectric material is computed from equation (2–34), giving a value of 4748 m/s. The measured impedance was also used to calculate the dielectric constant via equation (2–39). A plot of the relative dielectric constant ε^S as a function of frequency is shown in figure 2–12. The relative dielectric constant ε^S was determined by averaging over a range of frequencies, indicated in figure 2–12, and is 757. The loss tangent tan δ_e is 0.016. The measured anti-resonant frequency is 7.89 MHz. The slope of an X/R versus f/f_a plot is inversely proportional to the attenuation coefficient a according to equation (2–36), which is shown in figure 2–13. The slope was calculated within the region $0.99 < f/f_a < 1.01$. The calculated value of the attenuation coefficient a is 47.6 Np/m or 0.41 dB/mm. According to equation (2–37) the attenuation coefficient a can be converted into the mechanical quality factor Q_m. The computed Q_m is 110 at the anti-resonant frequency.

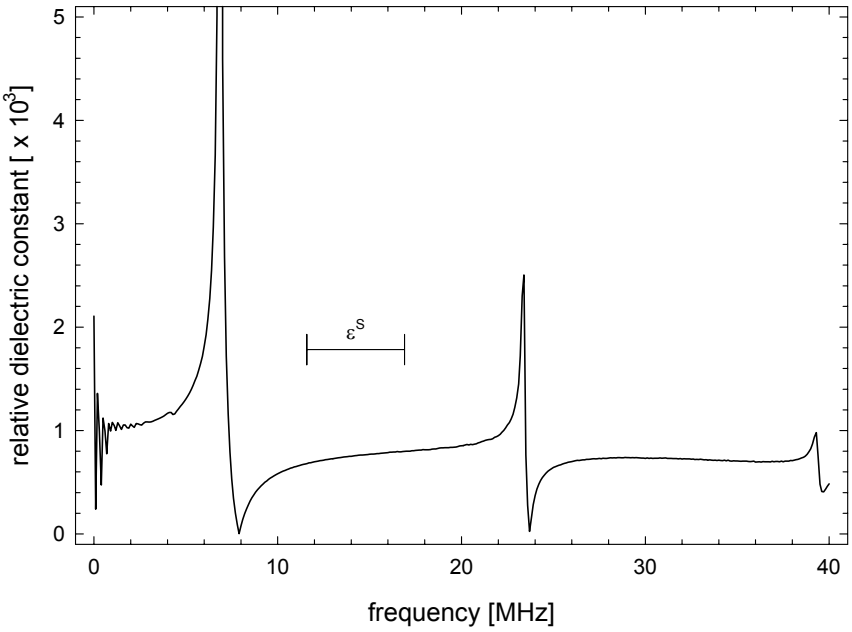

Figure 2–12 Measurement of the dielectric constant ε^S of a 0.3mm thick PXE-5 transducer with an area of 2 cm × 2cm. The dielectric constant ε^S is calculated by averaging the values within the region indicated in the figure.

The parameter values found in step 1 are now optimized in steps 2 and 3. The parameter values obtained after each optimization step are shown in table 2–2. Measured and simulated resistance and reactance are shown in figure 2–14 after each optimization step. The solid and dashed line correspond to the experimental resistance and reactance data, respectively. The simulated values are represented by the black circles and open triangles, respectively. The frequency interval used for measurement and simulation is 7.5 kHz. A difference of 15 kHz (two

sample points) for the parallel resonance frequency between the measured and simulated curves can be observed when using the parameter values of step 1 in the model (figure 2–14a). After fitting the parameters in step 2 (figure 2–14b) the parallel resonance frequency of simulated and measured curves coincide. The differences from the values found in step 1 are small. In step 3 the resistance and reactance are fitted near the first resonance frequency (6-9 MHz). The parameter values found after fitting are listed in table 2–2 (step 3) and the impedance plot is shown in figure 2–14c.

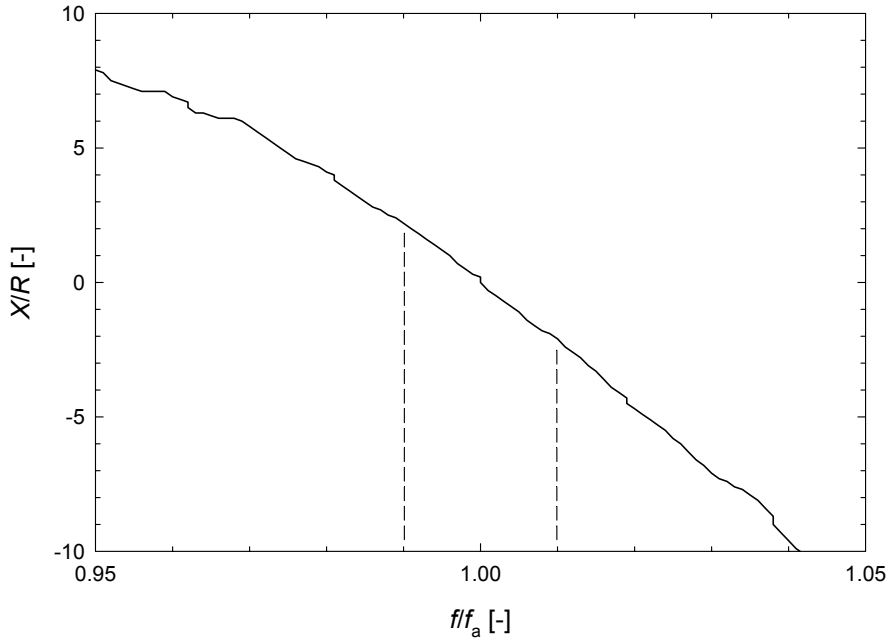

Figure 2–13 A plot of X/R versus f/f_a for the PXE-5 transducer, as calculated from the measured input impedance data, is inversely proportional to the attenuation coefficient at the anti-resonant frequency f_a (7.89 MHz). This slope was calculated within the region $0.99 < f/f_a < 1.01$.

The mismatch in parallel resonance frequency between measured and simulated data after step 1 can be explained considering c_{33}^D. This parameter value is decreased by $7 \cdot 10^8$ (0.4 %) by optimization step 2 and 3, with respect to step 1. Substituting this value in equation (2–33) gives a frequency shift of 26.5 kHz. When the sample frequency of 7.5 kHz is taken into account, the error of 26.5 kHz is within the range covered by two sample points (30 kHz). The relative biggest change occurred in the dielectric loss tangent, which decreased by 62.5 % (from 0.016 to 0.010), cannot be observed in the graphs shown. After step 3, the dielectric loss tangent almost returned to the value obtained with step 1.

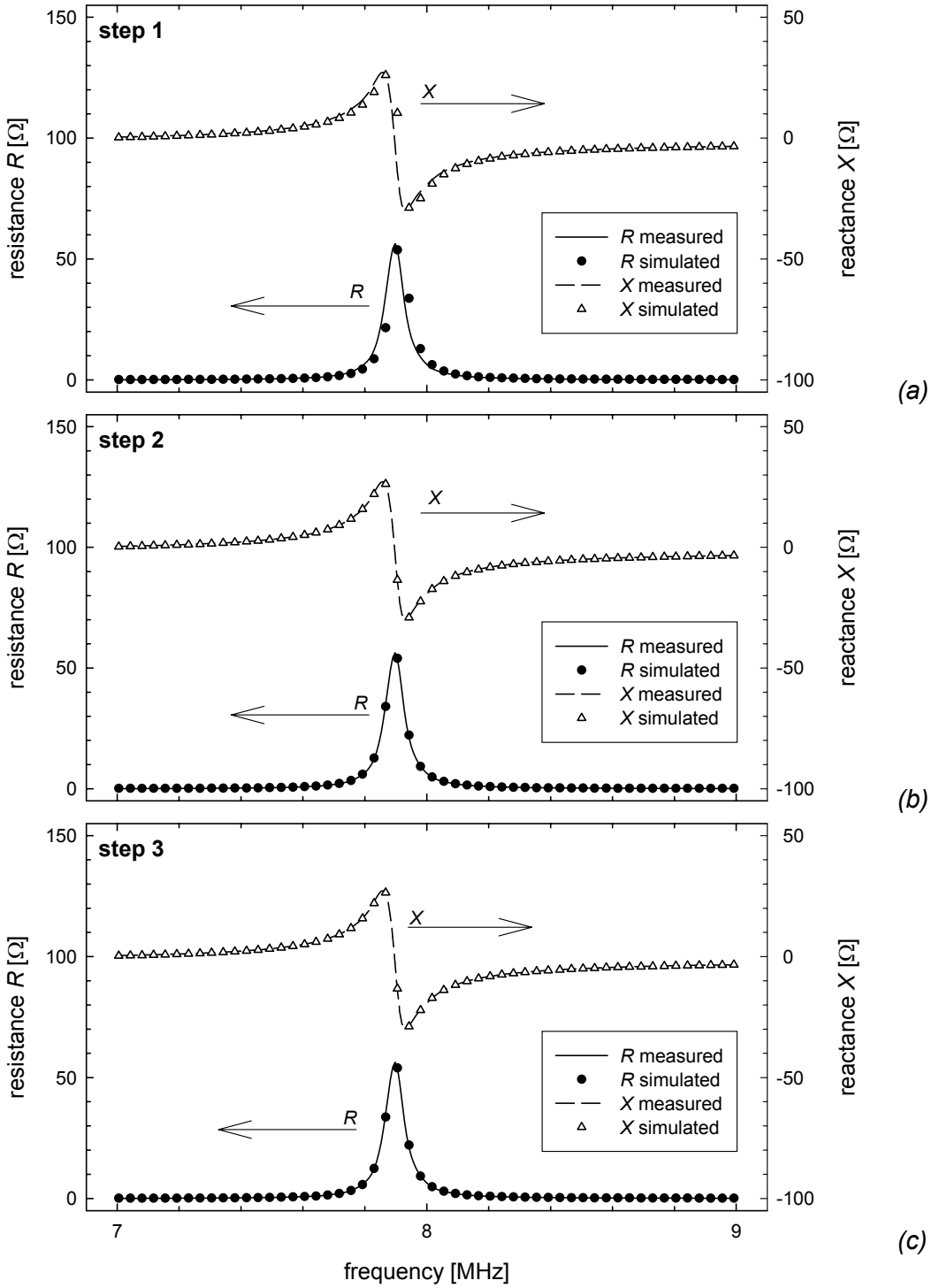

Figure 2–14 Comparison of simulated (dots) and experimental results (lines) of the 2 cm × 2 cm PXE-5 transducer near the first resonance frequency for step 1, 2 and 3. Resistance R (solid line, closed circles) and reactance X (dashed line, open triangles). Note: not all simulated data points are shown for clarity.

Table 2–2 Estimated material parameters of a 2 cm × 2 cm PXE-5 transducer after each step of the 3-step parameter estimation method.

			value			
parameter	**equation**	**definition**	**step 1**	**step 2**	**step 3**	**unit**
k_t	(2–30)	thickness coupling coefficient	0.53	0.53	0.53	[-]
c_{33}^D	(2–33)	elastic stiffness constant	$1.758 \cdot 10^{11}$	$1.751 \cdot 10^{11}$	$1.751 \cdot 10^{11}$	[N/m^2]
Q_m	(2–37)	mechanical quality factor	110	109	110	[-]
$tan\ \delta_e$	(2–38)	dielectric loss tangent	0.016	0.010	0.015	[-]
ε^S	(2–39)	permittivity	757	747	755	[-]

The values of k_t and Q_m did not change significantly during all optimization steps and can therefore accurately be estimated by step 1. The values found for ε^S and tan δ_e depend on the frequency range. In the range near resonance (6 MHz – 9 MHz, step 1 and 3) they result in almost the same values, but optimization over a wider frequency range (100 Hz – 40 MHz; step 2) gives lower values, see table 2–2. A PXE-5 transducer will be modeled using the values found in the column *step 2* to enable accurate modeling over a wide frequency range.

2.4.3 Parameter estimation of a PVDF transducer

The calculated input impedance for the standard KLM model (loss-less) is shown in figure 2–15. The complex dielectric constant and complex elastic stiffness (equations (2–10) and (2–9)) are not yet included in the model. The graph clearly shows a substantial mismatch between the measured and calculated curves. The phase difference between the calculated and measured impedance is approximately 14 degrees. The calculated and measured magnitude deviate 5 % for the shown frequency span. Adding losses, i.e. the complex dielectric constant and complex elastic stiffness, to the model reduces the mismatch significantly as will be shown below.

A similar 3-step procedure, as used in the previous section, was followed to obtain accurate model parameters for the PVDF transducer (Kynar, AMP) with an area of 4 mm × 4 mm and a thickness of 110 µm. The differences with respect to the previous method are that frequency dependent values for ε^S and $tan\ \delta_e$ are used and only one optimization step is performed. The 3-step procedure is:

1. To obtain the piezoelectric parameters, the input impedance of the transducer was measured using the methods described in section 2.3.
2. The measured ε^S and *tan* δ_e were both smoothly fitted by a power function and a 6th order polynomial (see figure 2–16), respectively.
3. Subsequently, the obtained parameters and smoothly fitted functions were applied to the model and an optimization step (changing k_t, Q and $c_{33}{}^D$) was performed using the *downhill simplex method* according to Nelder and Mead.

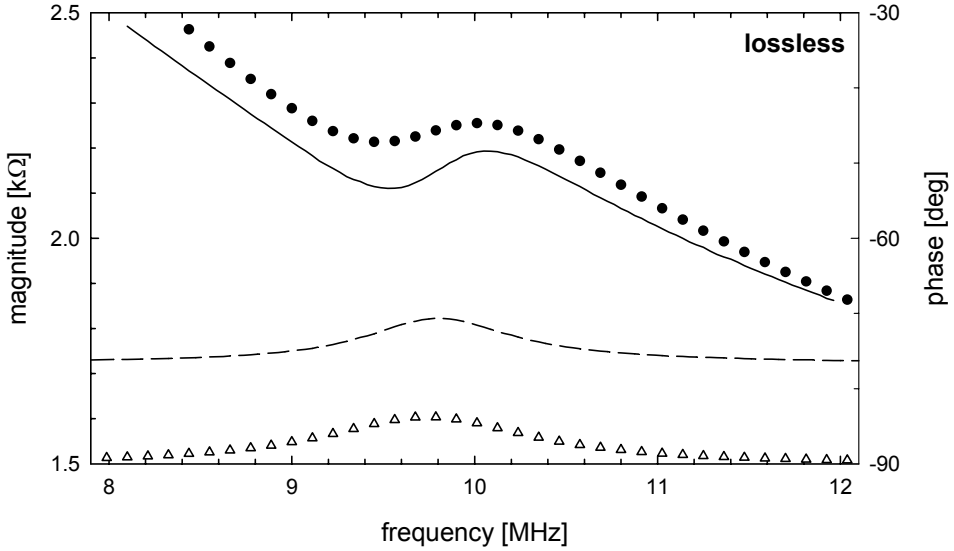

Figure 2–15 Measured (lines) and simulated (dots) magnitude using the standard KLM model (solid line and black circles, respectively) and phase (dashed line and open triangles, respectively) of the input impedance of the PVDF transducer.

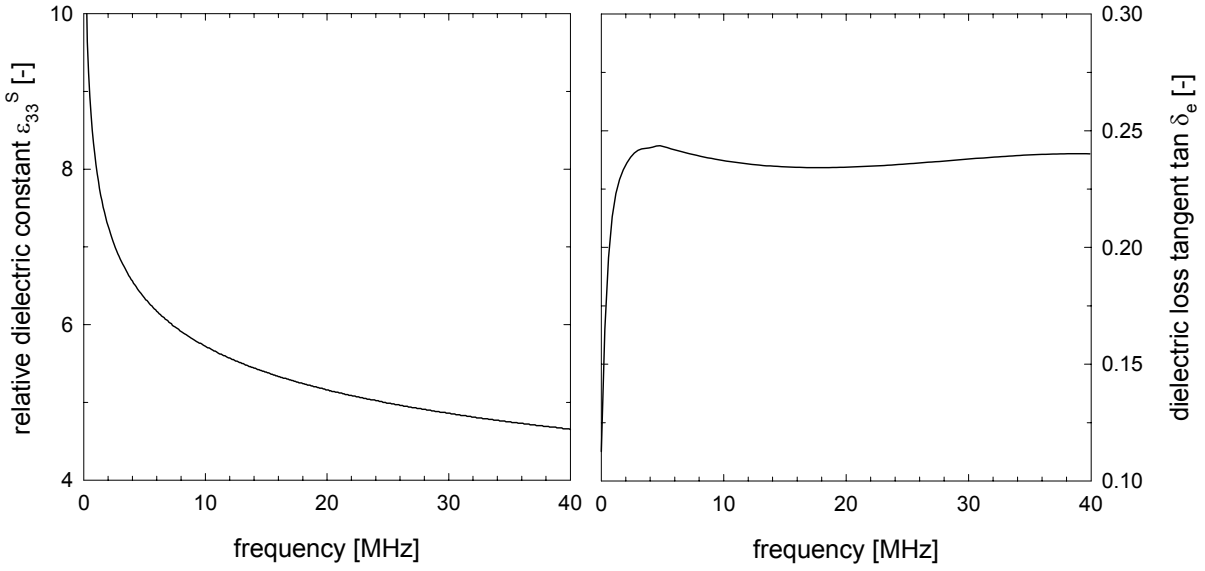

(a) *(b)*

Figure 2–16 Smoothly fitted (a) relative dielectric constant ε^S and (b) dielectric loss tangent tan δ_e calculated from the measured input impedance data of the PVDF transducer.

The model parameters found after step 1 are listed in table 2–3. The density ρ of the PVDF film is 1780 kg/m^3. In step 2, the constant values for ε^S and tan δ_e found during step 1 were replaced by the smoothly fitted curves shown in figure 2–16.

Table 2–3 Estimated material parameters of the 4 mm × 4 mm PVDF transducer after the first step of the 3-step parameter estimation method.

parameter	definition	value	unit
k_t	thickness coupling coefficient	0.137	[-]
c_{33}^D	elastic stiffness constant	$8.32 \cdot 10^9$	[N/m^2]
Q_m	mechanical quality factor	7.1	[-]
tan δ_e	dielectric loss tangent	0.24	[-]
ε^S	relative dielectric constant	5.64	[-]

The measured (lines) and simulated (dots) data of the modified model after step 1, 2 and 3 are shown figure 2–17. The error between the measured and simulated data decreases from 3.3 % (step 1), to 1.7 % (step 2) and to 0.26 % (step 3). Table 2–4 shows the parameters that are subject to change during the optimization steps, and the corresponding values after step 1 and 3. The values of the model parameters obtained after step 3 give the smallest error between measurement and simulation.

Table 2–4 Estimated material parameters of the 4 mm × 4 mm PVDF transducer after step 1 and 3 of the 3-step parameter estimation method.

parameter	description	step 1	step 3	unit
k_t	thickness coupling coefficient	0.137	0.115	[-]
Q_m	mechanical quality factor	7.1	9.5	[-]
c_{33}^D	elastic stiffness constant	$8.32 \cdot 10^9$	$8.28 \cdot 10^9$	[N/m^2]

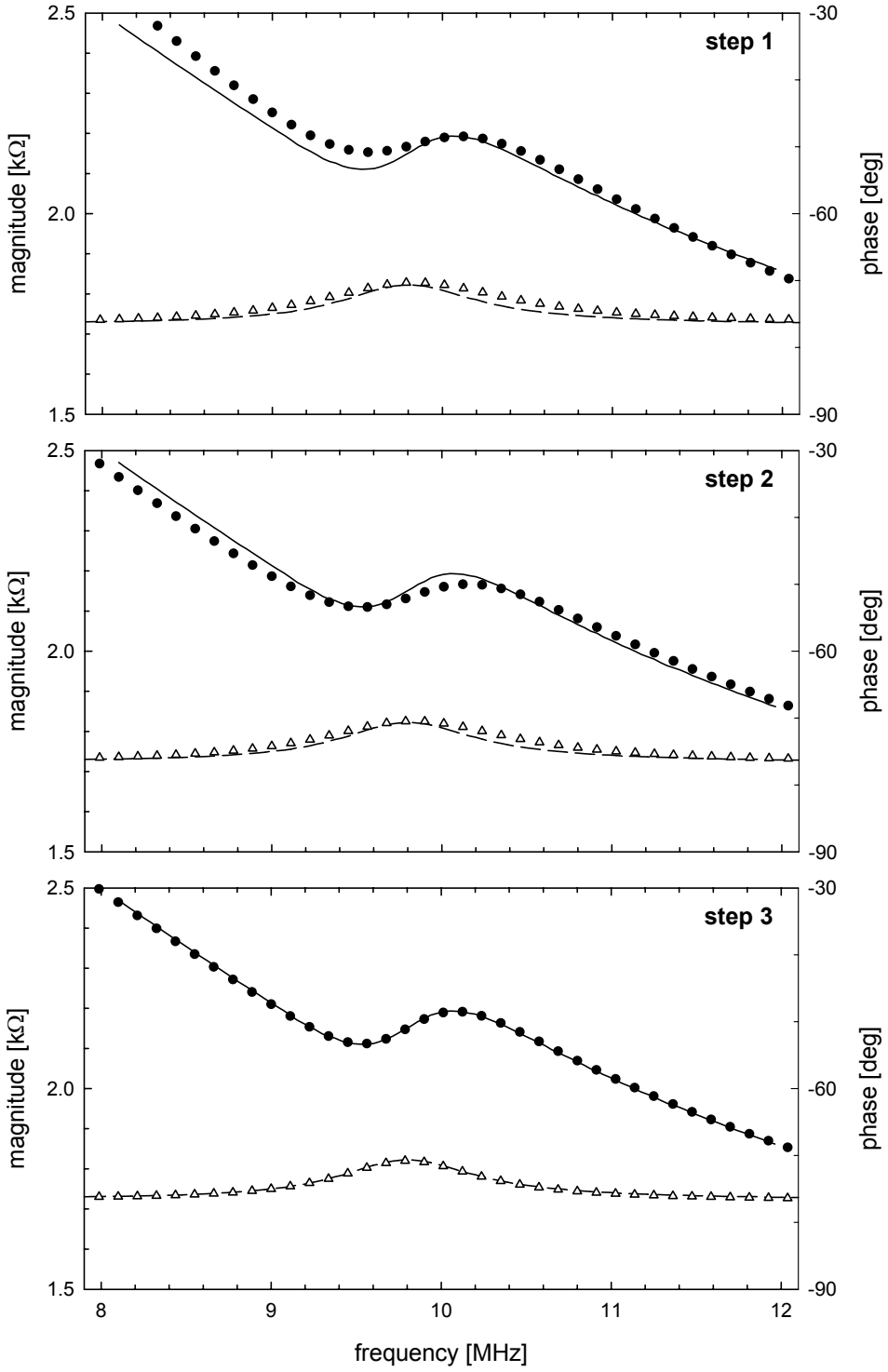

Figure 2–17 Measured and simulated magnitude (solid line and black circles, respectively) and phase (dashed line and open triangles, respectively) for step 1, 2, and 3.

2.5 Model verification using a PXE-5 transducer with backing

Some measurements and simulations in the frequency and time domain were performed to verify the modified KLM model for the PXE-5 transducer used in section 2.4.2 including a backing impedance. Three types of measurements were done: impedance measurement, insertion loss and pulse echo response. A 2 cm × 2 cm epoxy-backed transducer with a thickness of 0.3 mm was built using PXE-5 as the piezoelectric material. Figure 2–18 shows a schematic cross section of the transducer. The electrical input impedance of the transducer, measured using an HP 4192A Impedance/Gain-Phase Analyzer with an HP 16047D test fixture, is shown in figure 2–19. The graph shows that the measured and experimentally obtained data match. A more detailed description of transducer fabrication, measurement setup and data analysis can be found in chapters 4 and 5.

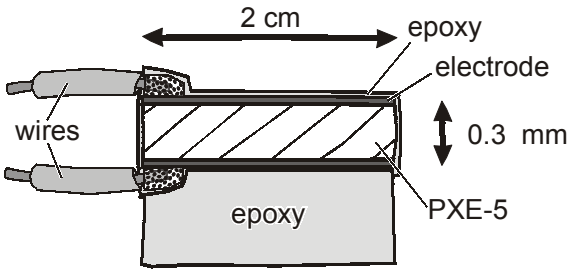

Figure 2–18 Schematic cross section of the PXE-5 transducer used for verification of the modified KLM model.

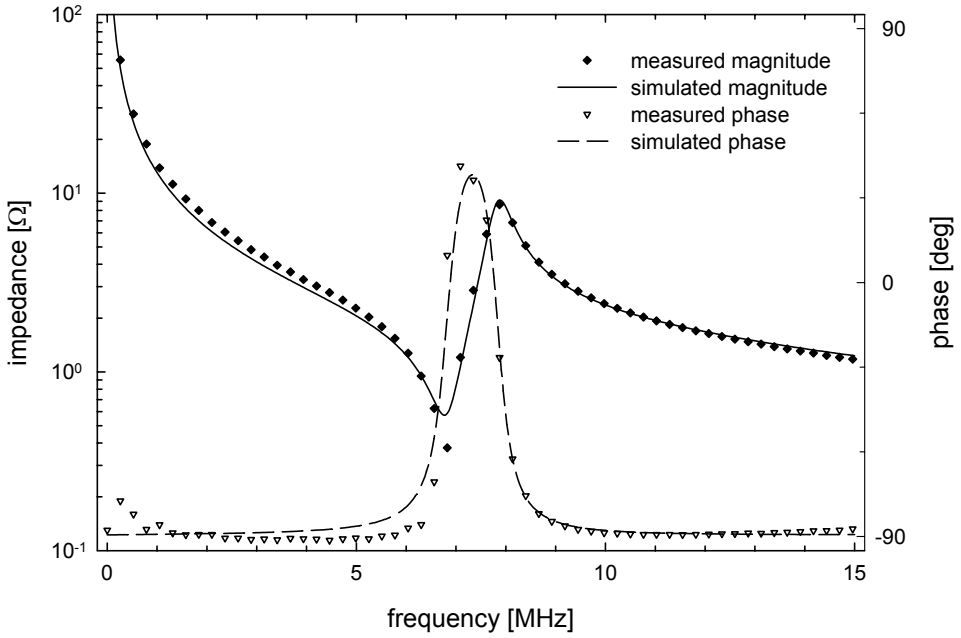

Figure 2–19 Electrical input impedance: comparison of measurement data (dots) and calculated data (lines) for a PXE-5 transducer (magnitude: solid line; phase: dashed line).

The setup for measuring the insertion loss and pulse-echo response is shown in figure 2–20. The insertion loss of the transducer was measured by transmitting an acoustic wave from the transducer, excited by a 50 Ω internal impedance pulse function generator (HP 8111A). The amplitude of the output of this generator into a 50 Ω load was measured at each frequency, so as to determine the available power. The transmitted energy was reflected by a perfectly reflecting air-water interface and received by the transducer loaded by the same 50 Ω generator. A high impedance oscilloscope (HP 54520A) was used to measure both the transmitted and received electrical signals. The insertion loss was calculated by comparing the available transmitted power and the received power as a function of the frequency, and was compared to the theoretical values, as shown in figure 2–21. The insertion loss of the transducer was -24.4 dB at 7.8 MHz and the theoretical value was -18.7 dB. The experimental values were fitted by shifting the theoretical curve -5.5 dB. The -6 dB bandwidth (BW) was 780 kHz, as predicted.

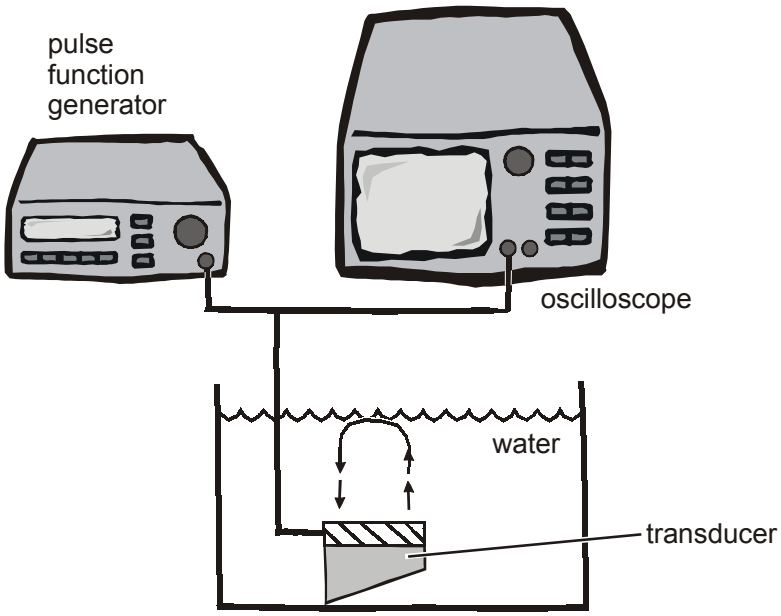

Figure 2–20 Measurement setup for determining the insertion loss and pulse-echo response of a piezoelectric transducer. The air-water interface is used as the reflector for the ultrasonic wave.

A comparison of the experimental and theoretical impulse response of the transducer is shown in figure 2–22. The theoretical impulse response was calculated by taking a fast Fourier transform of the transducer transfer function as described in subsection 2.2.3. The experimental results were obtained by applying one period of a 7.35 MHz sine wave with an amplitude of 7.5 V to the transducer using an HP 8111A pulse function generator and digitizing the reflected echo with an HP 54520A oscilloscope at a sample rate of 250 MSamples per second (MSa/s). The measured signal was averaged 256 times. The peak-peak ampli-

tude of the measured and simulated pulse-echo response are 61 mV and 99 mV, respectively. The difference between these values correspond to -5.5 dB.

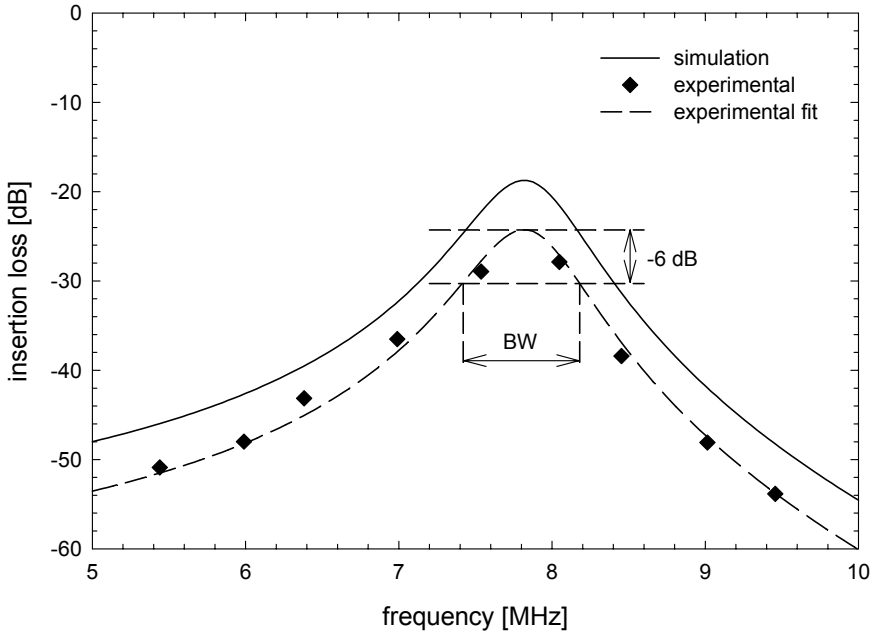

Figure 2–21 Insertion loss: comparison of measurement data (dots) and theoretical data (line) for a PXE-5 transducer.

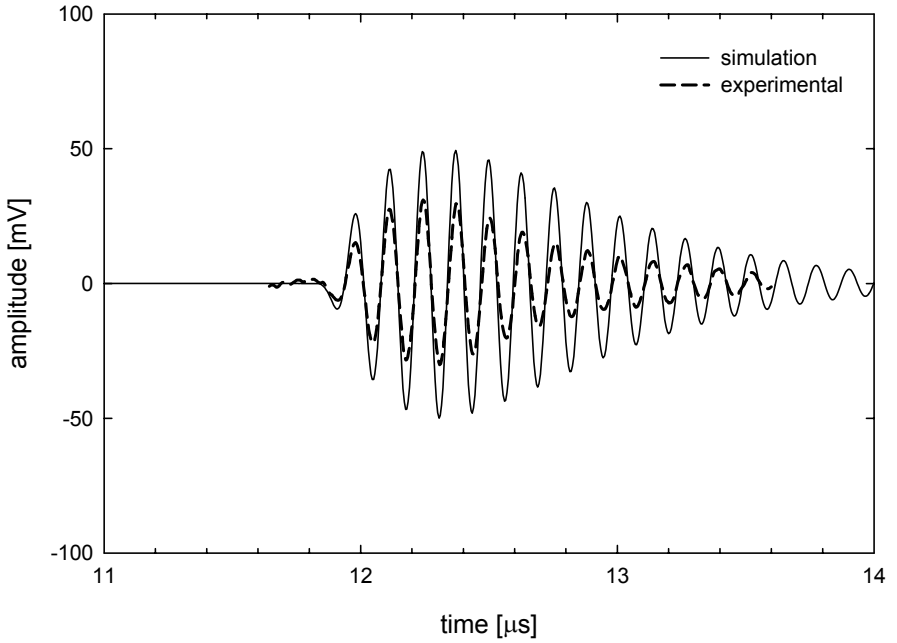

Figure 2–22 Impulse response: comparison of measured signal (dots) and theoretical signal (line) for the PXE-5 transducer.

Although the experimentally found data shows a greater loss than the theoretically predicted values, the model is useful to predict the transducer's behavior qualitatively as well as quantitatively.

2.6 Conclusions

APLAC offers a straightforward implementation of the (modified) KLM model and accurate modeling of both ceramic and polymer piezoelectric transducers, since it is capable of modeling frequency dependent components. The model verification shows that the model is useful to predict the transducer's behavior when the transducer construction is altered (adding backing impedance).

References

[1] K.S. Van Dyke, "The electric network equivalent of a piezoelectric resonator," *Physical Review*, vol. 25, pp. 895, 1925.

[2] W.P. Mason, *Electromechanical Transducers and Wave Filters*, 2nd ed. New York: Van Nostrand Company, Inc., 1948.

[3] M. Redwood, "Transient Performance of a Piezoelectric Transducer," *The journal of the Acoustical Society of America*, vol. 33, no. 4, pp. 527-536, 1961.

[4] R. Krimholtz and D.A. Leedom, "New Equivalent Circuits for Elementary Piezoelectric Transducers," *Electronics letters*, vol. 6, no. 13, pp. 398-399, 1970.

[5] E.K. Sittig, "Transmission Parameters of Thickness-Driven Piezoelectric Transducers Arranged in Multilayer Configurations," *IEEE transactions on sonics and ultrasonics*, vol. SU-14, pp. 167-174, 1967.

[6] G. Hayward and M.N. Jackson, "Discrete-Time Modeling of the Thickness Mode Piezoelectric Transducer," *IEEE transactions on sonics and ultrasonics*, vol. SU-31, no. 3, pp. 137-150, 1984.

[7] L. Capineri and L. Masotti, "Ultrasonic Transducer as a Black-Box: Equivalent Circuit Synthesis," *IEEE transactions on ultrasonics, ferroelectrics and frequency control*, vol. 40, no. 6, pp. 694-703, 1993.

[8] C.G. Hutchens and S.A. Morris, "A three port model for thickness mode transducers using Spice II," *Ultrasonics symposium proceedings*, pp. 897-902, 1984.

[9] R. Schwarz, "Digital computer simulation of a piezoelectric thickness vibrator," *The journal of the Acoustical Society of America*, vol. 62, no. 2, pp. 463-467, 1977.

[10] S.A. Morris and C.G. Hutchens, "Implementation of Mason's Model on Circuit Analysis Programs," *IEEE transactions on ultrasonics, ferroelectrics and frequency control*, vol. UFFC-33, no. 3, pp. 295-298, 1986.

[11] W.M. Leach, "Controlled-Source Analogous Circuits and SPICE Models for Piezoelectric Transducers," *IEEE transactions on ultrasonics, ferroelectrics and frequency control*, vol. 41, no. 1, pp. 60-66, 1994.

[12] A. Püttmer and P. Hauptmann, "SPICE Model for Lossy Piezoceramic Transducers," *IEEE transactions on ultrasonics, ferroelectrics and frequency control*, vol. 44, no. 1, pp. 60-65, 1997.

[13] E. Maione and P. Tortoli, "PSpice Modelling of Ultrasound Transducers: Comparison of Software Models to Experiment," *IEEE transactions on ultrasonics, ferroelectrics and frequency control*, vol. 46, no. 2, pp. 399-406, 1999.

[14] Aplac Solutions Corporation. Aplac. [7.60]. 2000.
Ref Type: Computer Program

[15] E.K. Sittig, "Definitions Relating Conversion Losses in Piezoelectric Transducers," *IEEE transactions on sonics and ultrasonics*, vol. SU-18, pp. 231-234, 1971.

[16] M.D. Sherar and F.S. Foster, "The Design and Fabrication of High Frequency Poly(vinyldene fluoride) Transducers," *Ultrasonic Imaging*, vol. 11, pp. 75-94, 1989.

[17] F.S. Foster, L.K. Ryan, and D.H. Turnbull, "Characterization of Lead Zirconate Titanate Ceramics for Use in Miniature High-Frequency (20-80 MHz) Transducers," *IEEE transactions on ultrasonics, ferroelectrics and frequency control*, vol. 38, no. 5, pp. 446-453, 1991.

[18] J.H. Ih and B.H. Lee, "Attenuation coefficient of a piezoelectric resonator in a thickness mode," *Electronic Letters*, vol. 22, pp. 357-358, 1986.

[19] "IEEE Standard on Piezoelectricity, ANSI/IEEE Std 176-1987," *IEEE transactions on ultrasonics, ferroelectrics and frequency control*, vol. 43, no. 5, pp. 717-772, 1996.

[20] K.W. Kwok, H.L.W. Chan, and C.L. Choy, "Evaluation of the Material Parameters of Piezoelectric Materials by Various Methods," *IEEE transactions on ultrasonics, ferroelectrics and frequency control*, vol. 44, no. 4, pp. 733-742, 1997.

[21] P.N.T. Wells, *Ultrasonics in Clinical Diagnosis* Edinburg: Churchill Livingstone, 1977.

[22] B. Jaffe and W. Cook, *Piezoelectric Ceramics* New York: Academic Press, 1971.

[23] L.N. Bui and H. Shaw, "Study of Acoustic Wave Resonance in Piezoelectric PVF_2 Film," *IEEE transactions on sonics and ultrasonics*, vol. SU-24, pp. 331-336, 1977.

[24] J.G. Smits, "Iterative Method for Accurate Determination of the Real and Imaginary Parts of the Materials Coefficients of Piezoelectric Ceramics," *IEEE transactions on sonics and ultrasonics*, vol. SU-23, pp. 393-402, 1976.

Chapter 3

Design criteria and transducer optimization

3.1 Introduction

A reversible electromechanical transducer is a device that converts mechanical energy into electrical energy and vice versa. When designing such a transducer for a specific application the choice of the transducer material is critical. This section gives an overview of several piezoelectric materials (lead zirconate titanate, bariumtitanate, polymers, copolymers and lead metaniobate). Their strong and weak points and significant material parameters are compared.

For biomedical ultrasonic imaging applications, piezoelectric composites should transmit a strong acoustic pulse, and then detect the weak echoes reflected from the internal organ of the human body. Typical medical ultrasonic transducer probes are a few centimeters in size and operate in the low megahertz range. Ideally, the properties of such transducers include high piezoelectric response in both transmission and receiving modes, while maintaining acoustical matching and ease of use. Biomedical transducers require resonance frequencies of approximately 1.5 MHz - 30 MHz, high electromechanical coupling coefficients, low acoustic impedance, and a broad bandwidth [1,2].

To characterize a piezoelectric transducer the signal-to-noise-ratio is considered. First, the transducer signals will be described in subsection 3.1.2, followed by a short description of the noise sources in the transducer in subsection 3.1.3. Subsequently, the *SNR* of the proposed piezoelectric transducers will be presented.

After these definitions, three transducer types are presented in addition to the single element transducer. The three transducer types were simulated in APLAC to predict their performance. The latter includes power transfer and *SNR*.

3.1.1 Transducer materials and their properties

Lead zirconate titanate ceramic (PZT) is widely used as a transducer material because of its high piezoelectric coefficients. However, for hydrophone applications, PZT is a non-optimum material for several reasons. The hydrostatic piezoelectric charge coefficient ($d_h = d_{33} + 2d_{31}$), which reflects the ability to convert electrical energy into mechanical energy, is low due to opposite signs of the piezoelectric strain coefficients d_{33} and d_{31} even though both d_{33} and d_{31} are large. The hydrostatic piezoelectric voltage coefficient ($g_h = d_h/\varepsilon_0\varepsilon^S$), representing the ability to convert mechanical energy into electrical energy, is also low because of the high relative dielectric permittivity ε^S of PZT (1800). Moreover, the acoustic matching of PZT with water is poor because of its high density ρ (7800 kg/m^3), and the mechanical properties are far from favorable because it is a brittle, inflexible ceramic [1].

Although the piezoelectric properties of another group of materials, namely polymers, were already investigated in 1924, it was not until the work of Fukada in the 1950s and 1960s that this topic received attention. The breakthrough came in 1969, when Kawai discovered the strong piezoelectric effect in polyvinylidenefluoride (PVDF). PVDF exhibits considerably stronger piezoelectric activity than other polymers such as PVC and PVF [3]. More recently, Ohigashi *et al.* [4] found a much better electromechanical coupling in copolymers of vinylidene fluoride and trifluorethylene P(VDF-TrFE), see also page 11.

Polymers and copolymers have a very low dielectric constant in comparison to ceramic materials. The result is that the electrical input impedance of polymers is very high compared to that of ceramics. To generate an equal amount of acoustic output power a much higher driving voltage is required for polymers. The dielectric losses of polymers are large at high frequencies (>500 kHz). Since this loss is responsible for the dissipation of most of the electrical input power, only a relatively small fraction appears at the acoustic port [5].

The largest electromechanical coupling coefficient k_t reported for polymers (P(VDF-TrFE)) is 0.3 [6] whereas for ceramics it is 0.55 (PZT-5H) [7]. The square of k_t is a measure of the ratio of the transferred electromechanical energy to the total input energy. Therefore, with equal amounts of available electrical input power the ceramic transducer will generate more acoustic output than the polymer transducer [5].

To overcome the disadvantages of PZT, composites have been fabricated [8-12]. In composites a portion of the ceramic is replaced by a polymer, which reduces the acoustic impedance of the transducer, bringing it closer to that of water and

thus of the human body. Composites have improved properties with respect to homogeneous ceramics. The hydrostatic piezoelectric properties of these composites are superior to those of single phase PZT. Varaprasad [9] prepared PZT-silicone rubber composites with a g_{33} that was about four to five times that of PZT. However, fabrication of composites is rather delicate and time consuming [1,13].

A 3D plot with the coupling coefficient k_t on the x-axis, the acoustic impedance Z_0 on the y-axis and the dielectric constant ε_r on the z-axis is shown in figure 3–1 for five different types of piezoelectric materials: lead zirconate titanate (PZT), bariumtitanate, polymers (PVDF), copolymers (P(VDF-TrFE) and lead metaniobate. The material parameters summarized in this graph are obtained from [3,5-7,14-30]. Compared to lead zirconate titanate, bariumtitanate and lead metaniobate have a slightly lower acoustic impedance, approximately 34 MRayl compared to 20 MRayl [15,28] and 31.2 MRayl [14], respectively. However, the coupling coefficient of bariumtitanate and lead metaniobate is significantly lower as can be observed in figure 3–1. This will make these materials less suitable for transducer applications.

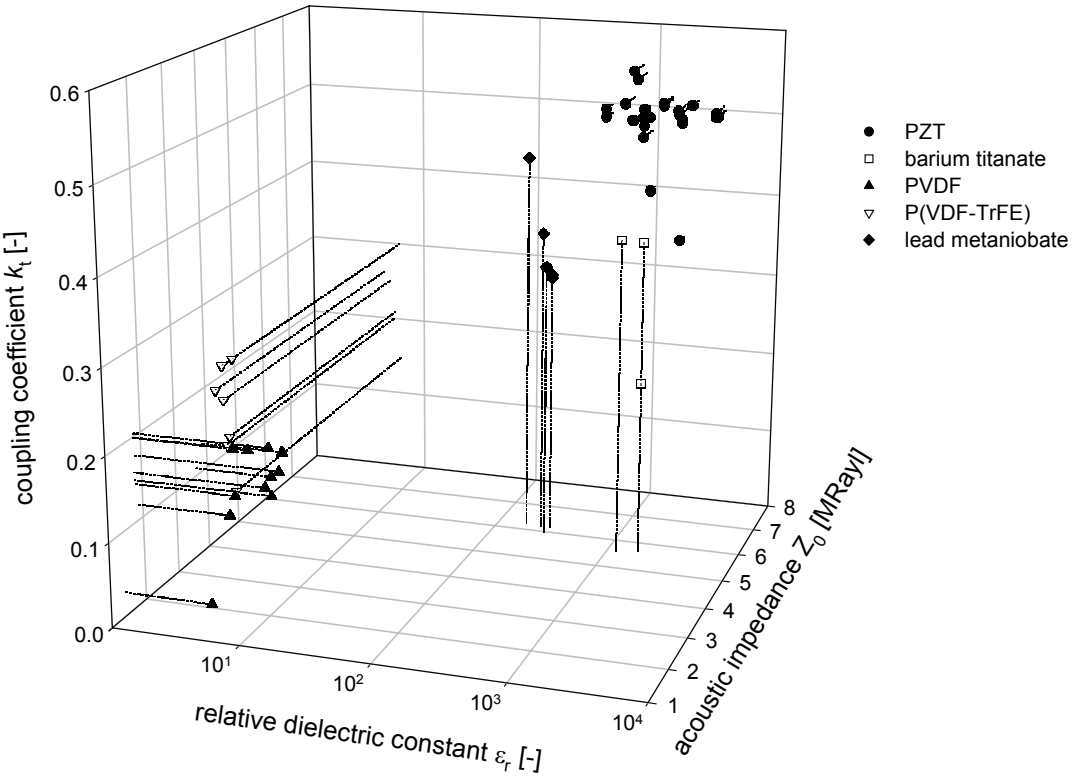

Figure 3–1 The coupling coefficient versus the relative dielectric constant versus the acoustic impedance for some piezoelectric materials (lead zirconate titanate, bariumtitanate, polymers, copolymers and lead metaniobate). Data is obtained from [3,5-7,14-30].

It is concluded that PZT is the best choice as an ultrasonic emitter, and that (co)polymers offer the best choice for receiving ultrasound. In sections 3.2.2 and

3.2.3 is described how these two materials can be integrated into one transducer.

3.1.2 Transducer signal

The amplitude of the electrical signal generated by a piezoelectric transducer is related to the axial pressure. A piezoelectric material shows a linear relation between the change in induced surface charge ΔQ and the change in applied force ΔF [31]:

$$\Delta Q = d\,\Delta F \tag{3–1}$$

where d is the charge sensitivity [C/N]. Assuming that the piezoelectric transducer is a parallel plate capacitor with a capacitance C_0 defined as:

$$C_0 = \frac{\varepsilon_0 \varepsilon^S A}{t} \tag{3–2}$$

where A is the area [m^2], t the thickness [m], and $\varepsilon_0\ \varepsilon^S$ the dielectric constant [F/m]. Since the potential difference ΔV across a plate capacitor is:

$$\Delta V = \frac{\Delta Q}{C_0} \tag{3–3}$$

it follows that:

$$\Delta V = \frac{td}{\varepsilon_0 \varepsilon^S}\frac{\Delta F}{A} = \frac{td}{\varepsilon_0 \varepsilon^S}\Delta P \tag{3–4}$$

which is independent of the area A.

3.1.3 Transducer noise

Noise will be defined as any unwanted signal that includes RF and acoustic interference as well as the random noise associated with the transducer and electronic circuitry. Random noise produced by a transducer includes shot noise, flicker or 1/f noise, and Johnson or thermal noise, [32,33].

Shot noise

An electric current is the flow of discrete electric charges q ($1.6\cdot10^{-19}$ C), which results in statistical fluctuations of the current. If the discrete charges flow randomly, the fluctuating rms current I_{sn} is given by:

$$I_{sn} = \sqrt{2qI_{DC}\Delta f} \tag{3–5}$$

where I_{DC} is the DC current. In piezoelectric transducers there is no steady state current. Shot noise can therefore be neglected for ultrasonic transducers.

Flicker noise

Flicker or 1/f noise, in contrast to Johnson and shot noise, is not generated according to well known physical principles, and thus not well understood. There-

fore, it is hard to discount its importance on theoretical grounds. Flicker noise has approximately a 1/*f* spectrum (equal power reduction per decade of frequency) and is sometimes called 'pink noise'.

Flicker noise is not significant for ultrasonic transducers operating in the megahertz range, because the 1/*f* frequency dependence does not extend into the megahertz range.

Johnson noise

Johnson noise is the most important noise source in an ultrasonic transducer operating in the MHz range [32]. Johnson noise can be represented by a voltage source in series with a resistance *R*. The open circuit voltage E_{jn} can be expressed as:

$$E_{\text{jn}} = \sqrt{4kTR\Delta f} \tag{3–6}$$

where *k* is the Boltzman constant, *T* is the temperature in degrees Kelvin, *R* is the real part of the series impedance and Δ*f* is the bandwidth in Hz. It can also be represented by a current source in parallel with the impedance where the short circuit current I_{jn} can be expressed as:

$$I_{\text{jn}} = \sqrt{\frac{4kT\Delta f}{R}} \tag{3–7}$$

where *R* is the inverse of the real part of the parallel admittance.

3.1.4 Signal-to-noise ratio

The signal-to-noise ratio (*SNR*) is defined here as:

$$SNR = 20\log\left(\frac{V_{\text{S}}}{E_{\text{n}}}\right) \quad \text{[dB]} \tag{3–8}$$

where V_{S} is the maximum value of the discrete signal and E_{n} the rms value of the noise. It is important to define the bandwidth of the signal, especially when the signal has a narrow spectrum. In such a case, a larger bandwidth will reduce the *SNR*, because the signal power remains constant, whereas the noise power increases.

Equation (3–4) shows that the output signal of a piezoelectric transducer does not depend on its area, when the incident pressure Δ*P* is kept constant. The output signal of one transducer is V_{L}. Adding the signals of *n* transducers will result in an output signal V_{out} that linearly increases with the number of transducers:

$$V_{\text{out}} = nV_{\text{L}} \tag{3–9}$$

If all *n* noise sources are considered uncorrelated, [32] the squared amplitudes add:

$$E_{\text{r}} = \sqrt{\sum_{i=1}^{n}\left(E_{\text{n},i}\right)^2} = \sqrt{n\left(E_{\text{n}}\right)^2} \tag{3–10}$$

where E_r is the rms noise amplitude. E_r increases proportional with $\sqrt{n}$ [32] and the signal amplitude increases proportional with n. The signal-to-noise ratio SNR can now be written as [33]:

$$SNR = 20\log\left(\frac{nV_L}{E_r\sqrt{n}}\right) = 20\log\left(\frac{V_L}{E_r}\right) + 10\log(n) \qquad (3\text{–}11)$$

Consequently, the SNR of n transducers is calculated by adding $10\log(n)$ to the SNR of a single transducer. The noise must be integrated over the appropriate bandwidth.

3.2 Transducer types

Different piezoelectric materials and design configurations are considered to examine the effect on transducer efficiency. First, the single element transducer, consisting of either a ceramic or a polymer piezoelectric material with an optional backing layer, is considered. Second, transducers consisting of a ceramic and polymer piezoelectric material are presented: the dual element and the stacked transducer. The dual element transducer consists of two separate elements: one element for sending and one for receiving an ultrasonic signal. The materials used for the elements can be identical or different. The stacked transducer consists of two elements, which are made of different materials. In this chapter, a ceramic emitter with a polymer receiver on top is presented. Schematic representations of the described transducer types are shown in figure 3–2. Finally, the multi-element transducer–also shown in figure 3–2– is discussed. A multi-element transducer consists of several, identical transducer elements. The elements are connected electrically in parallel when in emitting mode and in series when in receiving mode.

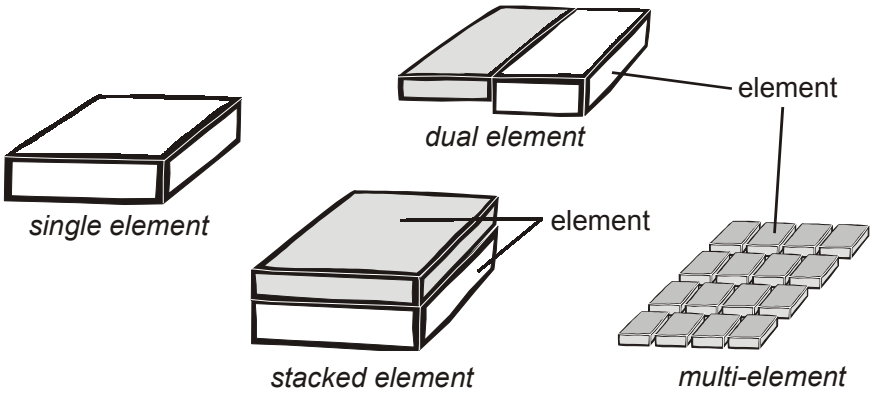

Figure 3–2 *Four transducer types: single, dual, stacked and a multi-element transducer, which all have the same total area. The single element transducer is made of one kind of material. The dual element transducer consists of two separate elements, which can be made of one or two types of material. The stacked element transducer is made of two different materials: a polymer on top of a ceramic. The multi-element transducer consists of an array of elements of the same material.*

3.2.1 Single element transducer

Introduction

The single element transducer has been described extensively in the previous chapter. One piezoelectric element is used for generation as well as for detection of an ultrasonic pulse. The transducer materials used for simulations are PXE-5, PVDF and P(VDF-TrFE). The parameters used for the simulations with these three materials are listed in table 3–1.

Table 3–1 Material parameters of PXE-5, PVDF and P(VDF-TrFE).

parameter	PXE-5	PVDF	P(VDF-TrFE)	unit
ρ (density)	7800	1780	1880	[kg/m^3]
v_p (sound velocity)	4738	2157	2318	[m/s]
Z_0 (acoustic impedance)	$3.7\cdot10^7$	$3.8\cdot10^6$	$4.4\cdot10^6$	[Rayl]
ε^S (relative permittivity)	755	5.64	4.38	[-]
Q_m (quality factor)	110	9.5	19.6	[-]
k_t (coupling coefficient)	0.53	0.12	0.26	[-]
tan δ_e	0.015	0.24	0.11	[-]
c_{33}^D	$1.751\cdot10^{11}$	$8.28\cdot10^9$	$10.1\cdot10^9$	[N/m^2]

Model

The model of the single element transducer has been described in chapter 2, but this will be repeated here briefly for convenience. The KLM model as presented by Krimholtz *et al*. [34] and shown in figure 3–3, can be used to model a single element transducer. Resistors should be added to the transmission line to model the substance that is present at the back and front face of the transducer.

The complete macro model for calculating the impulse response and the insertion loss of the transducer is given in figure 3–4. The transducer is actuated by the electrical source with amplitude V_S with an internal resistance R_S (usually 50Ω). The electrical energy is converted to mechanical energy and the resulting ultrasonic wave travels through a medium (load), is reflected and returns to the transducer that converts the wave into an electric signal across the load resistor with value R_L. The complete model can be found in chapter 2.

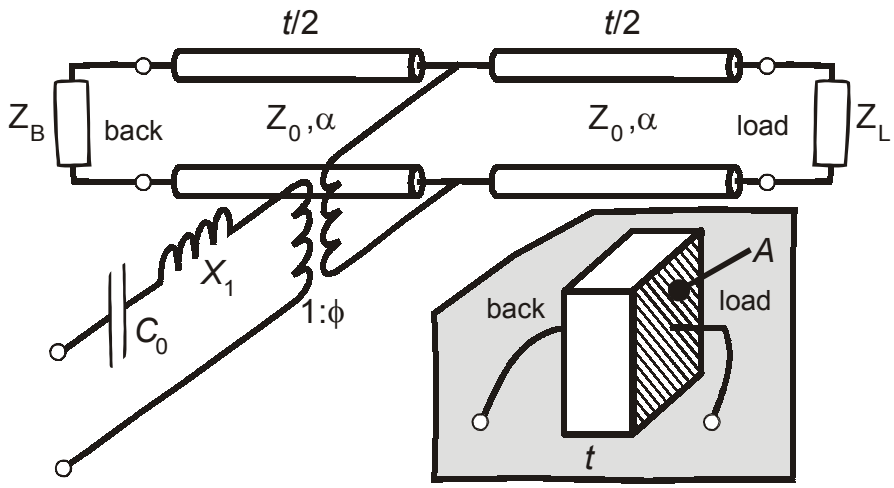

Figure 3–3 *KLM model for a single element transducer [34].* $C_0 = \varepsilon_0 \varepsilon^S A/t$, $Z_0 = A\rho v_p$, $X_1 = Z_0 M^2 \sin(t\omega/v_p)$, $M = h_{33}/(\omega Z_0)$, $h_{33} = k_t\sqrt{c_{33}{}^D/(\varepsilon_0\varepsilon^S)}$, $\Phi = 1/(2M)\sin^{-1}\left(\frac{1}{2}t\omega/v_p\right)$, *A = transducer area,* h_{33} *= piezoelectric constant,* v_p *= acoustic wave velocity,* $\varepsilon_0\varepsilon^S$ *= permittivity,* $c_{33}{}^D$ *= the elastic stiffness constant,* k_t *= thickness coupling factor, ρ = density, ω = angular frequency.*

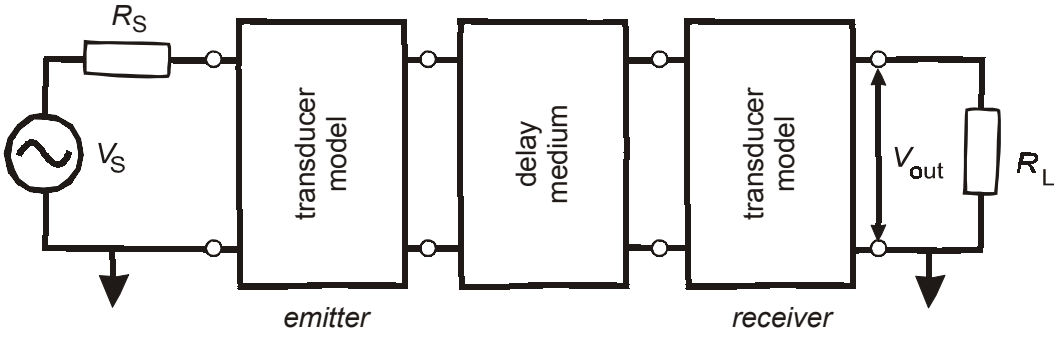

Figure 3–4 *Macro model based on the KLM model for a single element transducer for pulse-echo response and insertion loss calculations. The model includes a source with an internal resistance, a delay medium and a load resistor across which the reflected echo signal can be measured.*

The pulse-echo response and the insertion loss are obtained by first calculating the transfer function (frequency domain) of the entire system:

$$H(\omega) = \frac{V_{out}(\omega)}{V_S(\omega)} \tag{3–12}$$

The insertion loss *IL* of a network is defined as the ratio of power delivered by a source to a load with and without the network inserted. In this case, *IL* can be written as a function of the transfer function (see section 2.2.3):

$$IL = 20\log\left|\frac{R_L + R_S}{R_L}H(\omega)\right| \quad \text{dB} \tag{3–13}$$

The pulse-echo response in the time domain can be found by taking the inverse Fourier transform of the product of the transfer function $H(\omega)$ and the actuating signal $V_S(\omega)$:

$$V_{\text{out}}(t) = F^{-1}\{H(\omega)V_S(\omega)\} \tag{3–14}$$

In this model, it is assumed that all the emitted power will also be received by the transducer. This means that there are no losses in the medium, nor that the emitted wave diverges. Furthermore, it is assumed that the acoustic wave is reflected from a perfect reflector, which means that all incident power is reflected.

3.2.2 Dual element transducer

Introduction

Dual element transducers consist of an emitting and a receiving element in a single housing allowing emitter and receiver to operate independently. With single element transducers, operating in pulse-echo mode, the receiving electronics can be saturated during the transmission pulse. Receivers require a finite amount of time to recover from saturation. The advantage of two separately operating elements is that the returning echo can be detected faster compared to a single element transducer. In addition, the electronics become less complicated: saturation of the receiver does not have to be prevented when the transducer is activated. Moreover, the emitter and the receiver can be optimized separately for their specific function (sensor or actuator).

The dual element transducer considered here consists of a ceramic emitter and a polymer receiver. Figure 3–5 shows a possible setup in which the ceramic emitter is placed next to the polymer receiver.

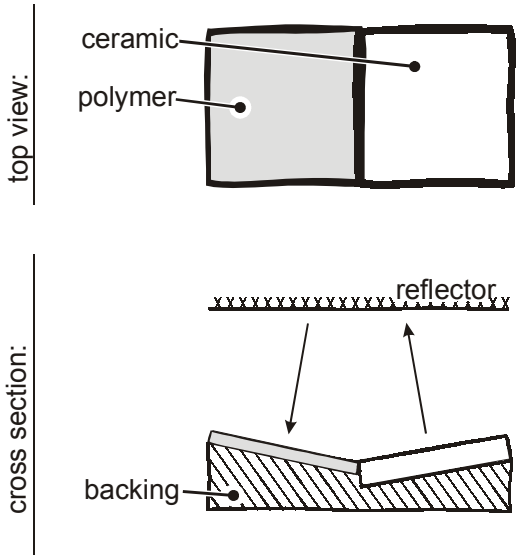

Figure 3–5 Dual element transducer setup consisting of a ceramic emitter with a polymer receiver.

Model

Modeling of the dual element transducer is analogous to modeling of a single element transducer. The difference is that the emitting element and the receiving element are not identical. The area of both the emitter and receiver are equal.

3.2.3 Stacked transducer

Introduction

In several patents a stacked transducer is described in which a ceramic piezoelectric material is used as an emitter of acoustic energy, and a polymer piezoelectric material for receiving the reflected acoustic energy [35-37]. An addition to this configuration is presented by Bui [38]: the front and back layers are made of piezoelectric materials, and are acoustically matched by the intermediate layers. The back layer functions as an ultrasound emitter while the front layer operates both as a matching layer and an ultrasound receiver.

The stacked transducer, which is depicted in figure 3–6, consists of a stack of three layers: a backing material on which an emitter is deposited and on top a receiver. The receiver thickness ideally equals one quarter of a wavelength of sound at the frequency emitted by the emitter. The receiver thus also forms a matching layer for optimal energy transfer from the emitter to the medium. The emitter consists of a plate of a piezoelectric ceramic material, preferably lead zirconate titanate, and two electrodes, one on each side. The receiver consists of a piezoelectric polymer material, for example PVDF, and two electrodes. The central electrode is a common electrode.

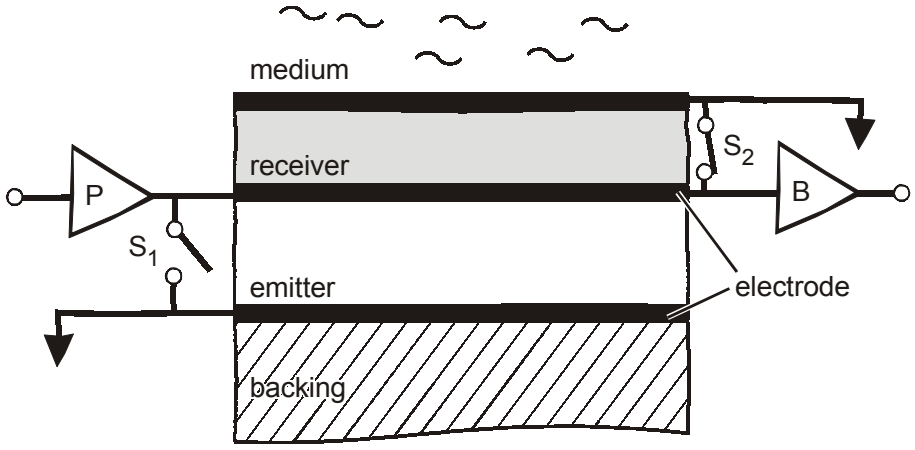

Figure 3–6 Cross sectional view of a stacked transducer.

During emission, the receiver is short-circuited, the switch S_2 is closed, and a short voltage excitation pulse is applied to the emitter via the amplifier P. After the excitation pulse is applied, the emitter is short-circuited by closing switch S_1 and the switch S_2 is opened. Now the acoustic waves that are reflected by the

object to be examined and are incident on the receiver produce a voltage between the electrodes, which is buffered by amplifier B. Ricketts [39] presented a similar transducer with the difference that during reception the emitter is not short-circuited, but loaded with an electrical impedance that optimizes receiver response and minimizes transducer noise.

Model

The model of a stacked transducer is more complicated than that of a single element transducer although there are many similarities. The stacked model consists of two parts: the ceramic (PZT) and polymer (PVDF) part. These two parts are clearly distinguished in figure 3–7, where each part can be identified as a separate KLM model. The front of the ceramic transducer is attached to the back of the polymer layer, as indicated in the inset. The outer electrodes (1 and 2) now become the electrical port of the stacked model, whereas the central electrode is connected to ground. The back of the ceramic and the front of the polymer are the two acoustical ports. This model can be treated like the single element as discussed in chapter 2.

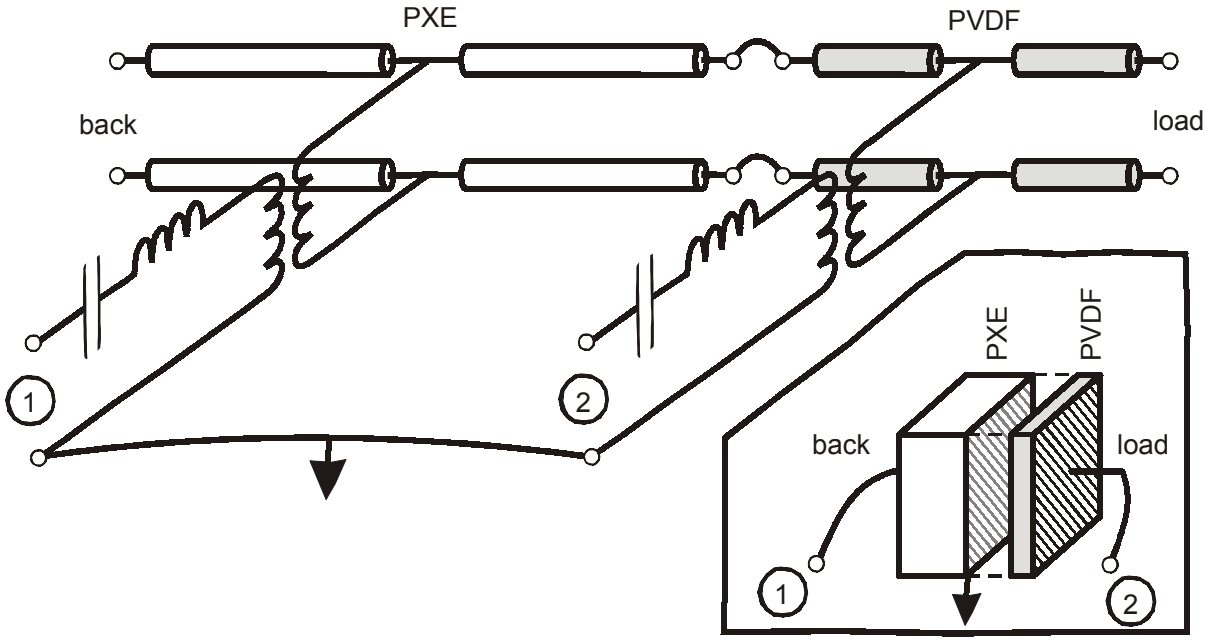

Figure 3–7 KLM model of the stacked transducer consisting of a PXE-5 emitting and a PVDF receiving element.

The setup presented in figure 3–8 was used to simulate the insertion loss and pulse-echo response of the stacked transducer. During activation, the electrical port of the ceramic transducer is connected to the source (V_S), while this port is connected to ground (with S_1) when in receiving mode (left side of figure 3–8). The polymer part is connected to ground (with S_2) during activation and to a load resistance (R_L) during receiving mode.

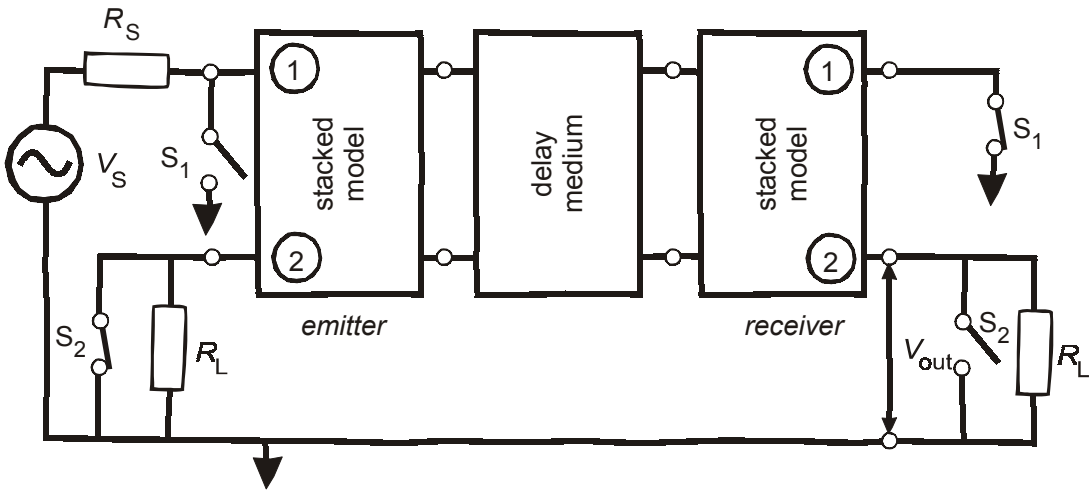

Figure 3–8 Macro model for insertion loss and pulse-echo response calculations. The 'stacked model' consists of the model shown in figure 3–7.

3.2.4 Multi-element transducer

Introduction

A multi-element transducer is proposed to enhance the *SNR* at equal power consumption. A schematic representation of a multi-element transducer, consisting of 16 transducer elements, a signal adder and a pulse generator is shown in figure 3–9. The transducer elements are connected in parallel when in emitting mode (left side). However, when the echo signal returns to the same transducer, the transducer elements are uncoupled and connected to the adder and the transducer element signals are added (right side of figure 3–9). Transducer optimization is the focus of this section. The multi-element transducer is therefore simulated in APLAC.

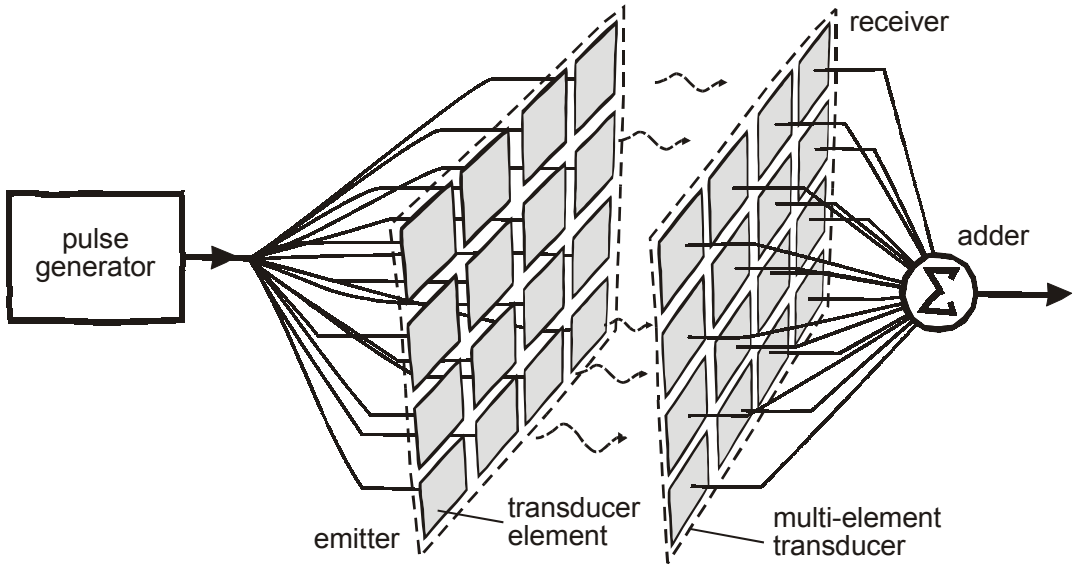

Figure 3–9 Schematic representation of a multi-element transducer consisting of 16 transducer elements.

Model

The model required to simulate the multi-element transducer is more complicated than the previous models. With some modifications, the model of a single element transducer can be used for a multi-element transducer. The main difference is that the area of the emitting and receiving elements is not equal. This induces a change in the power transfer model from the emitter to the receiver. Two transducer models with unequal area are connected by a delay medium, which consists of a voltage controlled voltage source. For modeling, the following assumptions are made. The emitter has an area A_E that is larger than the area of the receiver A_R. The fraction of power that is incident on the receiver is equal to the power that is produced by the same area of the emitter, as illustrated in figure 3–10a.

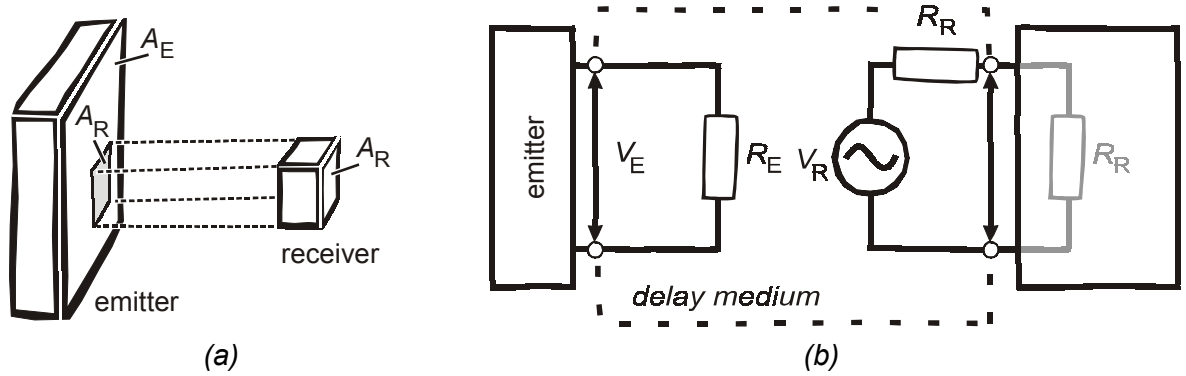

Figure 3–10 (a) Power transfer from a large emitter to a small receiver and (b) the electrical equivalent model of the power transfer.

The electrical equivalent circuit of the power transfer is depicted in figure 3–10b. The resistor values R_E and R_R are related proportional to the product of the area of the transducer and the acoustic impedance of the delay medium. Only a fraction of the power P_E

$$P_E = \frac{V_E^2}{R_E} \tag{3–15}$$

delivered to the resistor with value R_E is received by the receiver, which is:

$$P_R = \frac{A_R}{A_E} P_E \tag{3–16}$$

As already described in chapter 2, the voltage source V_R should be capable of delivering this power to the receiver if the receiver has a resistance of R_R, which is illustrated by the gray resistor in figure 3–10b. In that case, the power delivered to the receiver can be written as:

$$P_R = \frac{V_R^2}{4R_R} \tag{3–17}$$

Combining the three previous equations leads to:

$$V_R = 2V_E\sqrt{\frac{R_R}{R_E}\frac{A_R}{A_E}} \tag{3–18}$$

There is a linear relationship between the area of the transducer and the resistance R_E or R_R. Assuming that the area of the emitter is n times that of the receiver

$$A_E = nA_R \tag{3–19}$$

simplifies equation (3–18) to:

$$V_R = \frac{2}{n}V_E \tag{3–20}$$

Thus, a transducer that is divided into n elements, which are connected in parallel when in emitting mode and when in receiving mode the signals of the individual elements are added, can be modeled by the circuit presented in figure 3–11. The output signal is simply the product of the number of elements n and the signal per element. The noise at the output is the sum of the output noise of the individual elements. The *SNR* of a transducer consisting of n elements can be calculated using equation (3–11). This equation is also illustrated on the right hand side of figure 3–11.

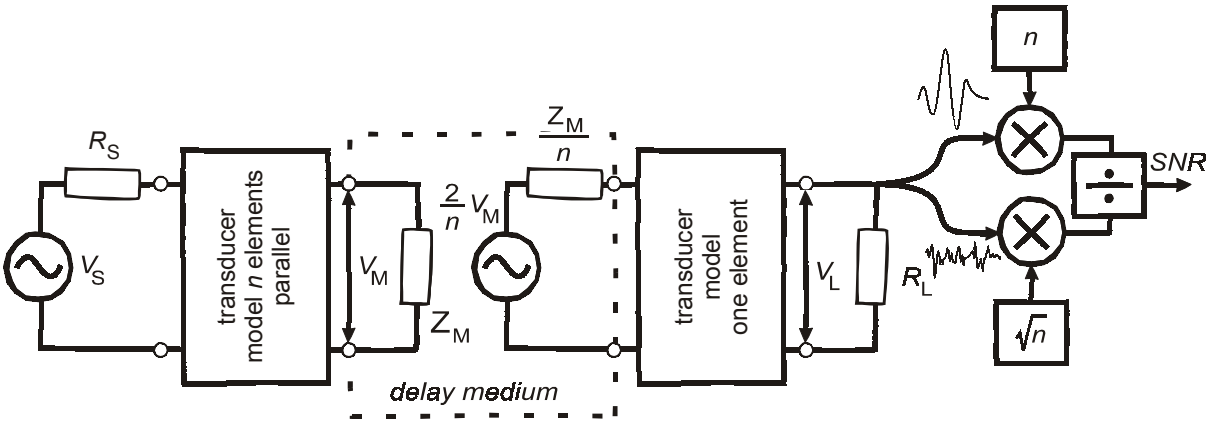

Figure 3–11 Simplified circuit for modeling of a multi-element transducer consisting of n elements.

3.3 Simulation results

This section is divided into two parts. First, the simulation results for the single element transducers (ceramic and polymer), a dual element transducer and a stacked transducer are presented. Second, the simulation results of the multi-element transducer are shown. This subdivision is made because modeling and operation of the first group of transducers differs significantly from that of the multi-element transducer.

The following simulation parameters were used: the load impedance and the backing impedance were taken 1.5 MRayl (water) and 4 MRayl (epoxy), respectively. The transducer area was 16 mm^2. Other parameters of the ceramic (PXE-5) and polymer (PVDF) transducer can be found in table 3–1. The transducer electrodes were not modeled. The source and load resistance were 50 Ω. For pulse-echo experiments a single cycle sine wave with a peak-peak amplitude of 20 V and a period of 137 ns (corresponding to 7.3 MHz) was used for all transducers except the PVDF transducer that was stimulated by a 10 MHz single sine wave. These values are listed in table 3–2.

Table 3–2 Simulation parameters.

parameter	value	unit
Z_B (backing impedance)	4.0	[MRayl]
Z_L (load impedance)	1.5	[MRayl]
R_S (source resistance)	50	[Ω]
R_L (load resistance)	50	[Ω]
excitation pulse amplitude	20	[V]
excitation pulse frequency (except PVDF transducer)	7.3	[MHz]
excitation pulse frequency (only PVDF transducer)	10	[MHz]

3.3.1 Single, dual and stacked element transducers

The insertion loss (*IL*) can be used to calculate the efficiency of an ultrasonic transducer in a certain medium (e.g. water). In chapter 2, it is described how the insertion loss is calculated from a simple network. The insertion loss of the four transducers was calculated from 100 Hz to 15 MHz using APLAC [40]. The results are shown in figure 3–12. The PVDF transducer shows the highest insertion loss (-72 dB at 7.3 MHz), followed by the dual element transducer (-42 dB). The stacked transducer has an insertion loss (-39 dB) that is only 3 dB less than the dual element transducer. The PXE-5 transducer has the lowest insertion loss (-12 dB). The -6 dB bandwidth of the PVDF transducer (10.2 MHz) is much larger than the bandwidth of the PXE-5 transducer (1.8 MHz). The bandwidth of the dual element and stacked transducer is 2.9 MHz and 3.9 MHz, respectively.

The simulated pulse-echo responses of the four setups are shown in figure 3–13. The PXE-5 transducer has a peak-peak amplitude (737 mV), which is about 350 times that of PVDF transducer (2.1 mV). The dual element transducer has a peak-peak amplitude of 33.2 mV, which is slightly lower than that of the stacked transducer (40.9 mV).

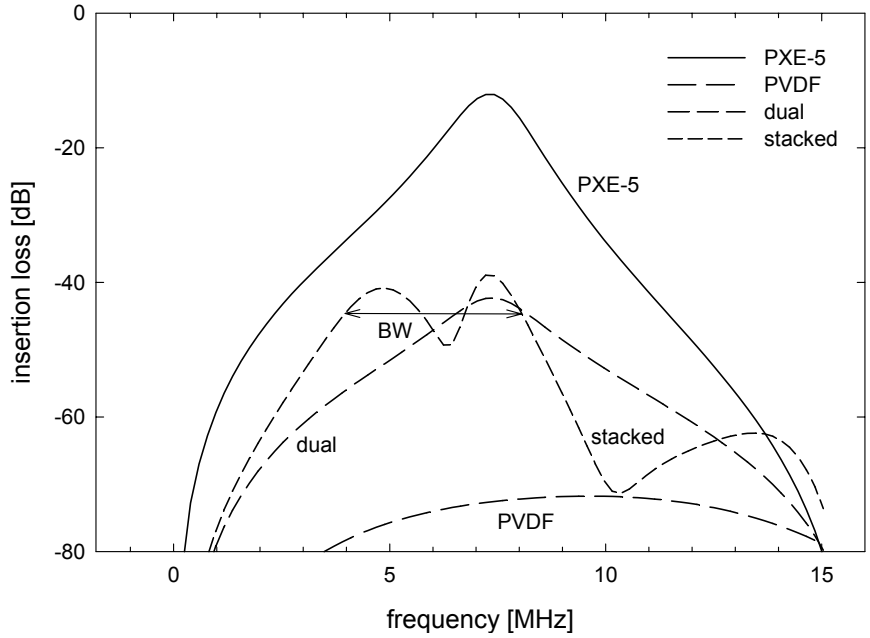

Figure 3–12 Insertion loss of the four transducer setups as a function of the frequency. Note that a high value of the insertion loss (less negative) corresponds to low insertion loss, see equation (3–13).

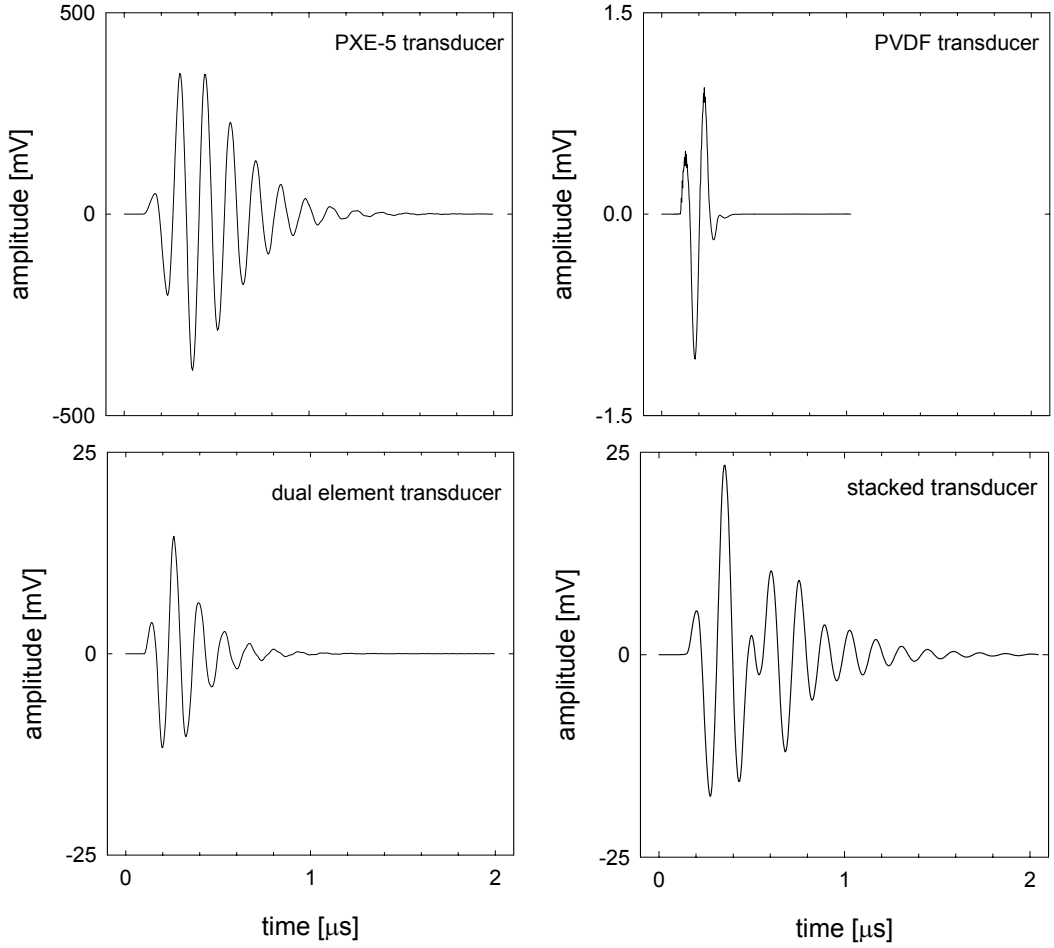

Figure 3–13 Pulse-echo response of the four transducer setups PXE-5, PVDF, dual element and stacked transducer.

For transducers consisting of only one material a strong (inverse) correlation between the maximum insertion loss and the bandwidth is found (figure 3–14). For the stacked and dual element transducer such a relation cannot be shown.

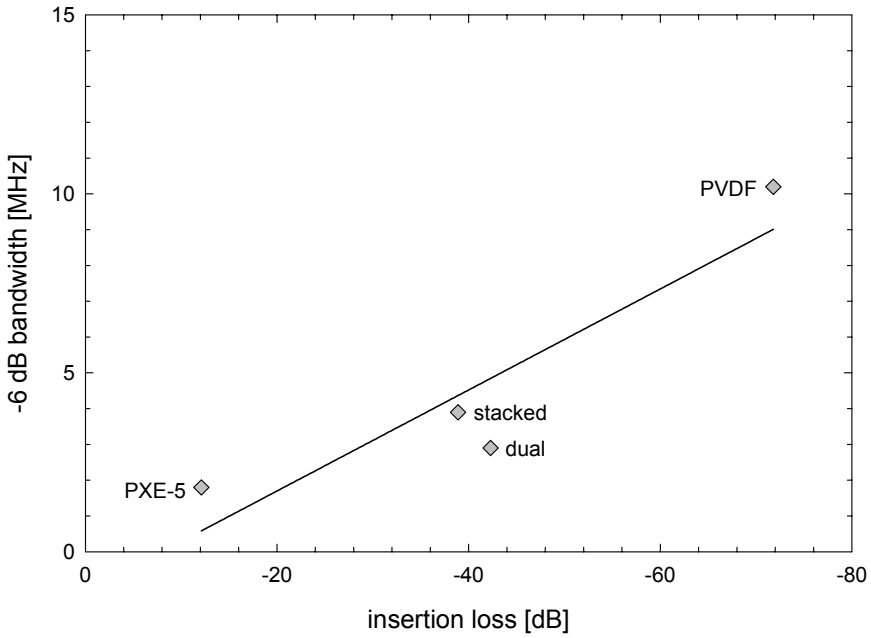

Figure 3–14 Comparison of the four transducer types: the -6 dB bandwidth versus the maximum insertion loss obtained from figure 3–13.

The high internal losses of the PVDF cause the transducer to be less efficient than the PXE-5 transducer. Obviously, when the dielectric and mechanical losses in the PVDF would be less the performance of the stacked transducer would improve. The copolymer P(VDF-TrFE) has properties similar to that of PVDF, regarding acoustic impedance and input impedance. However, the coupling coefficient of P(VDF-TrFE) is approximately twice that of PVDF [28]. A comparison between the material parameters of interest is shown in table 3–1. The parameters of P(VDF-TrFE) are obtained from Kwok [28].

To examine the better piezoelectric properties of P(VDF-TrFE) with respect to PVDF a stacked transducer with this polymer layer was simulated. The insertion loss and pulse-echo response are shown in figure 3–15. The maximum insertion loss is -25 dB, which means a loss of 14 dB less than that of the PVDF stacked transducer (-39 dB), but more than twice the insertion loss of the PXE-5 transducer (-12 dB). The peak-peak amplitude of the echo signal is 243 mV, which is one third of that of the PXE-5 transducer, but almost six times higher than the response of the PVDF stacked transducer.

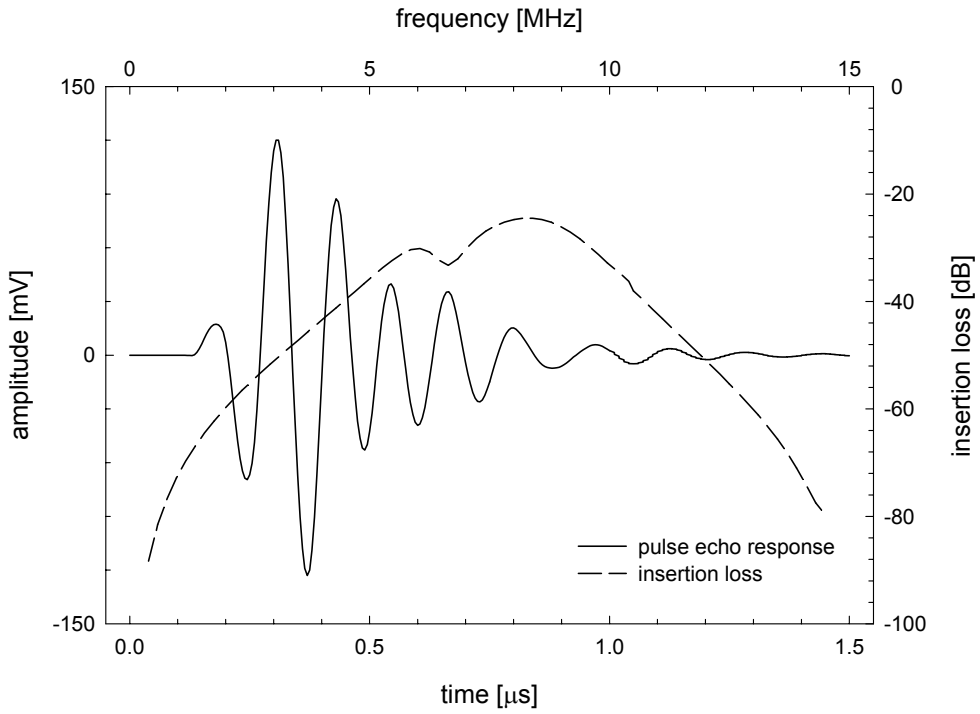

Figure 3–15 (a) insertion loss and (b) pulse-echo response of a stacked transducer with a P(VDF-TrFE) polymer layer.

Until this point, the *SNR* has not been considered. The echo signals of the proposed transducers (PVDF, dual element and stacked transducer) are smaller than that of the single element PXE-5 transducer, i.e. for a 50 Ω load resistor. If the load resistor is taken 1 MΩ the signal output of the polymer transducers will increase significantly. However, not only the signal amplitude is important, but the generated noise as well. Due to their high internal impedance polymer transducers will also generate more noise than the ceramic transducer with a much lower internal impedance. The *SNR* of the four transducer types, i.e. the PXE-5, PVDF, dual element and stacked transducer, is now calculated by using a 1 MΩ load resistor. This modeled resistor is noiseless to allow the determination of only the transducer noise, because the rms noise of a 1 MΩ resistor amounts 500 μV according to equation (3–6). The *SNR* was calculated over the frequency range 100 Hz to 15 MHz. The noise at the output was calculated by Richardson Interpolation using Simpson's Rule. This method gives an accurate result within 2 to 5 minutes on a Pentium II – 266 MHz, depending on the configuration. The noise simulation results are shown in figure 3–16. The PVDF transducer shows the lowest *SNR*, whereas the PXE-5 and stacked transducer have the highest *SNR*. The *SNR* of the PXE-5 transducer is 11 dB higher than that of the stacked transducer.

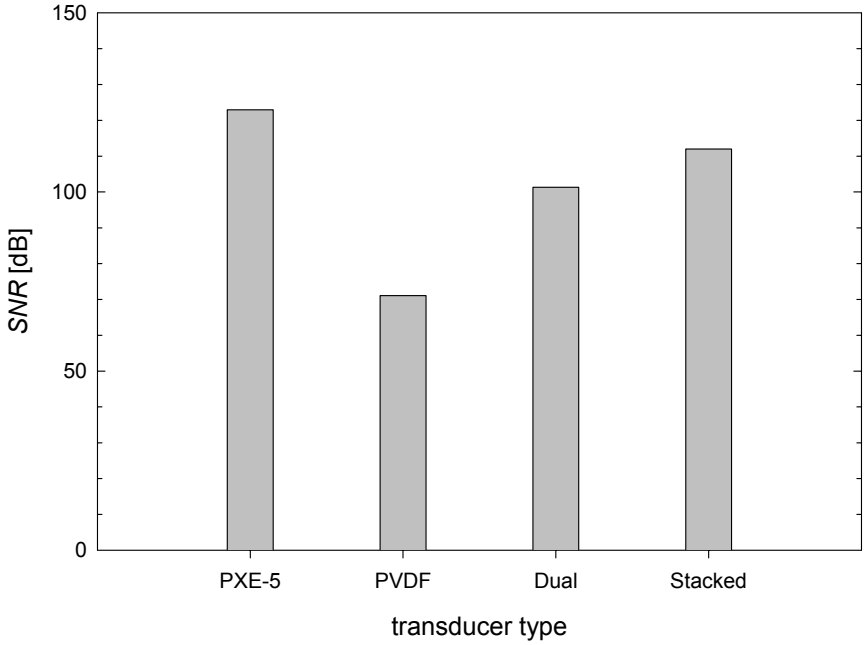

Figure 3–16 Calculated signal-to-noise-ratio of the PXE-5, PVDF, dual element and stacked transducer.

3.3.2 Single and multi-element transducer

The models for a single element transducer and a multi-element transducer were implemented in APLAC. Both transducer models use PXE-5 piezoelectric material parameters as listed in table 3–1. The simulation parameters are given in chapter 2. For the AC analysis, ranging from 100 Hz to 15 MHz, the peak-peak voltage of the sine wave was 10 V. The noiseless load resistor R_L had a value of 1 MΩ. The noise at the output of one element was calculated by Richardson Interpolation using Simpson's Rule.

In the first simulations, the area of the single element transducer was varied from the smallest usable element (0.3 mm × 0.3 mm; 0.3 mm is the half wavelength) up to 20 mm × 20 mm. The input impedance of the transducer was calculated for these and intermediate transducer areas and plotted in figure 3–17. The power transfer from the source to the transducer is maximal if the transducer's input impedance is equal to that of the source (usually 50 Ω, which corresponds to an area of 45 mm^2, as indicated in the graph). The transducer impedance is inversely proportional to its size indicating that the noise will, according to equation (3–6), increase for smaller transducers.

The output noise and output signal are plotted as a function of the transducer area in figure 3–18. The output signal is more or less constant for smaller transducer areas and decreases rapidly for larger areas (>4 mm × 4 mm). This is because for larger transducer areas the input impedance of the transducer drops below that of the source, which significantly decreases the power transfer to the transducer. The output signal amplitude is limited for smaller transducers, be-

cause the load resistance R_L is small compared to the transducer impedance. The output noise decreases with increasing transducer area, due to the smaller impedance of larger transducers.

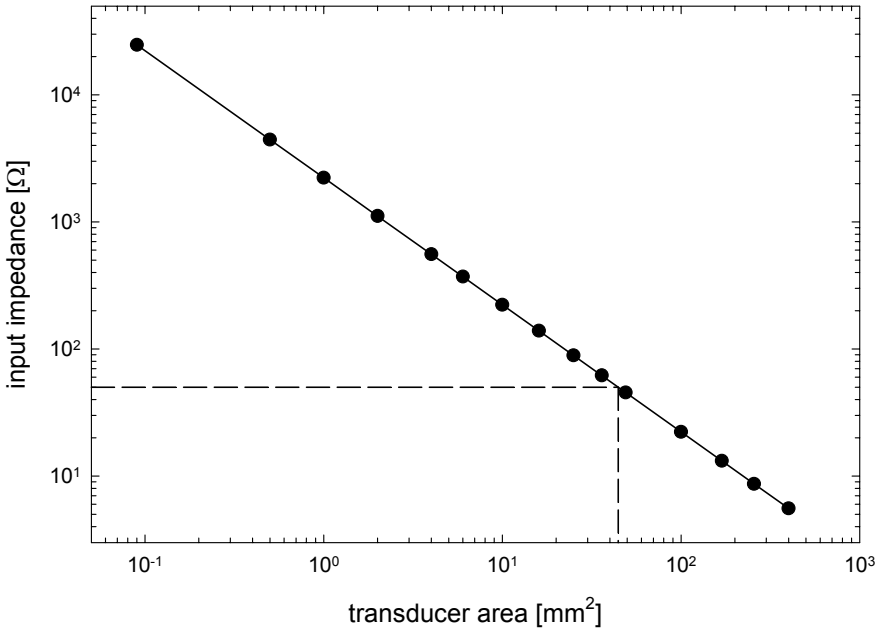

Figure 3–17 Calculated transducer input impedance versus the transducer area. The transducer model used for the simulations was a PXE-5 transducer with an epoxy backing of 4 MRayl immersed in water.

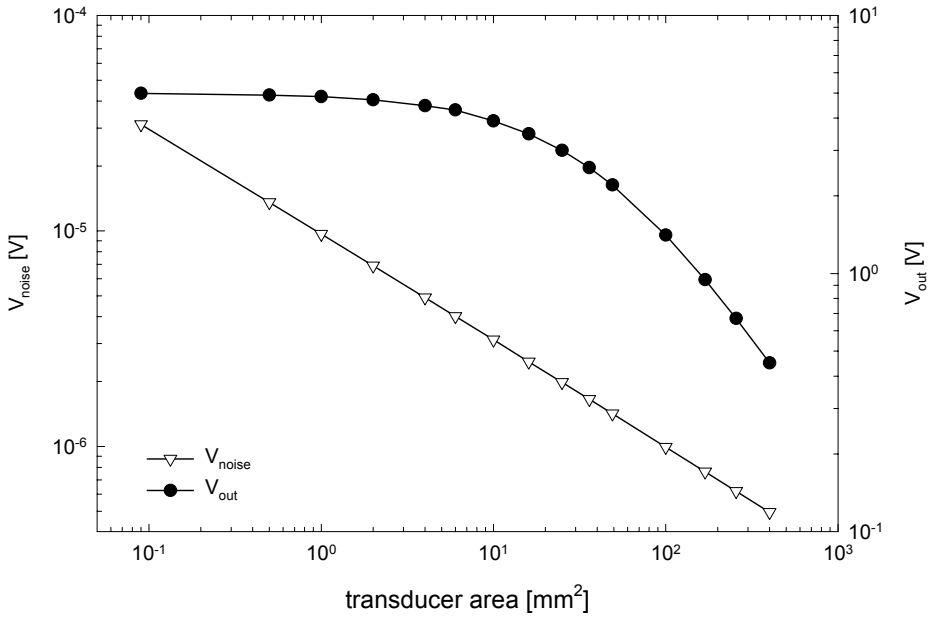

Figure 3–18 Output signal and output noise versus the transducer area.

Next, the *SNR* is plotted versus the transducer area in figure 3–19. Starting at the left side of the x-axis (small transducer area) the *SNR* increases, because the power transfer from the source to the transducer improves and the transducer noise decreases. Then, the *SNR* reaches a maximum and drops for larger

transducers due to a worse power transfer from source to load, decreasing the output signal. The smallest transducer has an *SNR* of 104.1 dB. The *SNR* reaches a maximum of 123.8 dB for a transducer area of 6 mm × 6 mm, and drops 5.0 dB for the largest transducer (20 mm × 20 mm). The transducer with an impedance closest to 50 Ω (45 mm^2) does not have the best *SNR*.

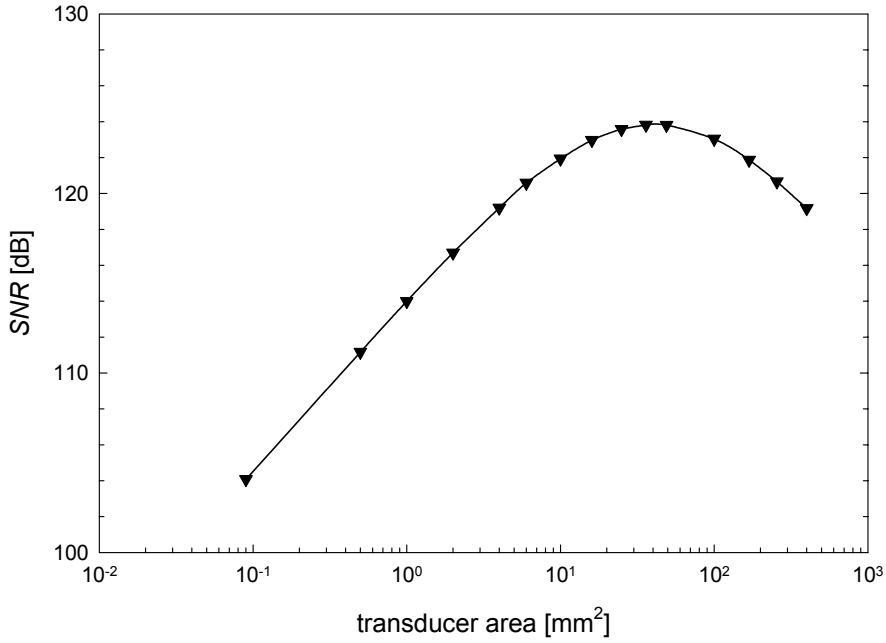

Figure 3–19 Calculated SNR versus the transducer area for a single element transducer.

The maximum area of the total transducer should be 5 mm × 5 mm as already stated in chapter 1. The effective area of a multi-element transducer is smaller, because the elements are separated by a non-piezoelectric material. Therefore, the maximum effective transducer area is chosen 4 mm × 4 mm.

In the following simulations, the *SNR* was calculated for four different transducer sizes, while the number of elements per transducer was varied. Figure 3–20 shows the *SNR* simulation results for four transducers with total areas of 2 mm × 2 mm, 4 mm × 4 mm, 6 mm × 6 mm and 20 mm × 20 mm. The graph shows that the *SNR* of the 4 mm × 4 mm transducer is approximately 0.8 dB lower than of the 6 mm × 6 mm transducer. The graph also shows that increasing the number of elements infinitely does not improve the *SNR* accordingly. Considering the 6 mm × 6 mm transducer shows that the *SNR* for 16 elements is only 0.12 dB less than for 25 elements.

In figure 3–21, the *SNR* is plotted as a function of the total transducer size of a single element transducer and a multi-element transducer consisting of 16 elements. The maximum *SNR* for the single and multi-element transducer are 123.8 dB and 126.2 dB, respectively. The difference between the two curves varies between 2.0 dB and 2.5 dB.

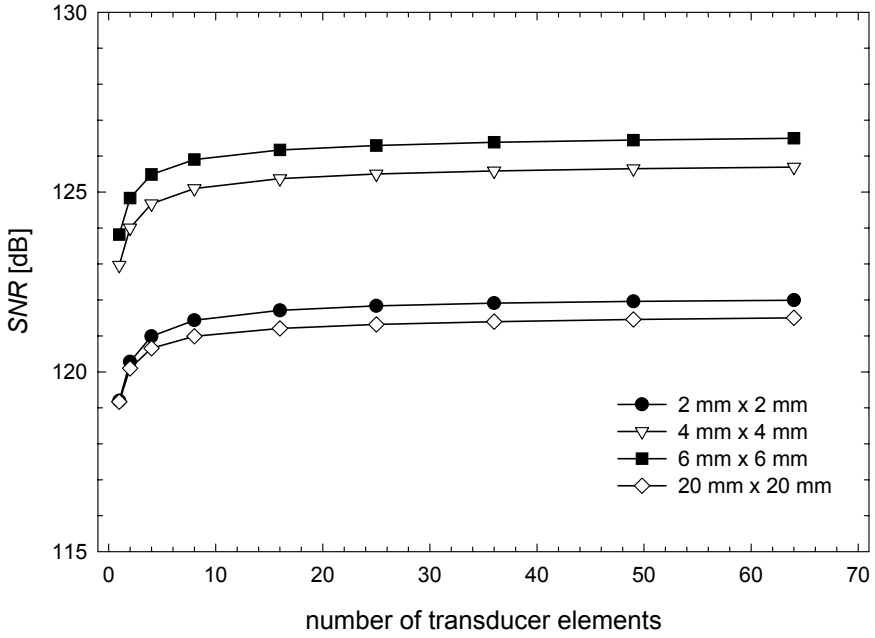

Figure 3–20 Calculated SNR as a function of the number of PXE-5 transducer elements for three multi-element transducers with total areas of 2 mm × 2 mm (black circles) 4 mm × 4 mm (white triangles), 6 mm × 6 mm (black squares) and 20 mm × 20 mm (white diamonds).

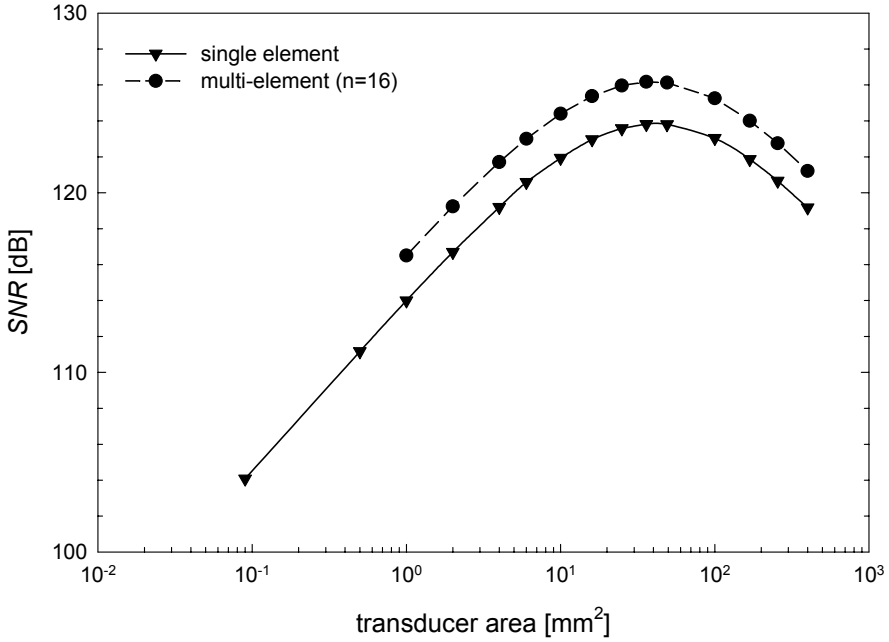

Figure 3–21 Calculated SNR versus the PXE-5 transducer area for a single element transducers and a multi-element transducer consisting of 16 elements.

3.4 Conclusions

The best transducer can be characterized as the transducer having the lowest insertion loss, the highest *SNR* and the broadest bandwidth, resulting in the best pulse-echo response. Since a low insertion loss and a broad bandwidth are incompatible a trade-off must be made between insertion loss and bandwidth. This choice is easily made if one wants to make a power efficient transducer, which is only used for distance detection of a pulse at a single frequency. Thus, the optimum transducer is the transducer with the lowest insertion loss, a pulse-echo response with highest peak-peak amplitude and the highest *SNR*. Table 3–3 lists the minimum insertion loss (IL_{min}), -6 dB bandwidth (BW) and *SNR* of the pulse-echo response of the simulated transducer types presented in this chapter. The PXE-5 transducer has superior pulse-echo response behavior and *SNR*. Improvement in the transducer's performance may only be achieved by optimizing a PXE-5 transducer.

Table 3–3 Minimum insertion loss, -6dB bandwidth and signal-to-noise-ratio of the simulated transducer configurations.

transducer type	IL_{min} [dB]	BW [MHz]	*SNR* [dB]
PXE-5	-12	1.8	123
PVDF	-72	10.2	71
dual element	-42	2.9	101
stacked	-39	3.9	112

APLAC simulations predict that a PXE-5 transducer consisting of multiple elements gives a better *SNR* than a single element transducer with the same total area. However, increasing the number of transducer elements does not result in an unlimited *SNR* increase. A transducer with an effective area of 4 mm $\times$ 4 mm consisting of 16 elements has an *SNR* that is only 0.3 dB lower than an equivalent transducer consisting of 64 transducer elements. On the other hand, a 16-element transducer with an effective area of 4 mm $\times$ 4 mm has an *SNR* that is 2.4 dB higher than a single element transducer of equal area.

The maximum possible *SNR* is limited by two factors. First, the maximum transducer area is restricted to 5 mm $\times$ 5 mm (design criterion). Second, fabrication of a transducer with a large number of transducer elements is hard to realize (connections and electronics), but nevertheless a technological challenge.

References

[1] J.F. Fernandez, A. Dogan, Q.M. Zhang, J.F. Tressler, and R.E. Newnham, "Hollow piezoelectric composites," *Sensors and Actuators A*, vol. 51, no. 2-3, pp. 183-192, 1996.

[2] T.R. Gururaja, "Piezoelectrics for Medical Ultrasonic Imaging," *American Ceramic Society bulletin*, vol. 73, no. 5, pp. 50-55, 1994.

[3] G.M. Sessler, "Piezoelectricity in polyvinylidenefluoride," *The journal of the Acoustical Society of America*, vol. 70, no. 6, pp. 1596-1608, 1981.

[4] H. Ohigashi and K. Koga, "Ferroelectric Copolymers of Vinylidenefluoride and Trifluoroethylene with a Large Electromechanical Coupling Factor," *Japanese journal of applied physics*, vol. 21, pp. L455-L457, 1982.

[5] R.G. Swartz and J.D. Plummer, "On the Generation of High-Frequency Acoustic Energy with Polyvinylidene Fluoride," *IEEE transactions on sonics and ultrasonics*, vol. SU-27, no. 6, pp. 295-303, 1980.

[6] H. Ohigashi, K. Koga, M. Suzuki, T. Nakanishi, K. Kimura, and N. Hashimoto, "Piezoelectric and ferroelectric properties of P(VDF-TrFE) copolymers and their application to ultrasonic transducers," *Ferroelectrics*, vol. 60, pp. 263-276, 1984.

[7] S. Saitoh and M. Izumi, "A Dual Frequency Ultrasonic Probe for Medical Applications," *IEEE transactions on ultrasonics, ferroelectrics and frequency control*, vol. 42, no. 2, pp. 294-300, 1995.

[8] A. Safari, R.E. Newnham, L.E. Cross, and W.A. Schulze, "Perforated PZT-polymer composites for piezoelectric transducer applications," *Ferroelectrics*, vol. 41, pp. 197-205, 1982.

[9] A.M. Varaprasad and R. Krishnan, "PZT-polymer composites for transducers of hydrophone systems," *Sensors and Actuators*, vol. 14, pp. 361-368, 1988.

[10] Y. Hirata and H. Okuyama, "Piezoelectric composites for micro-ultrasonic transducers realized with deep-etch x-ray lithography," *Proceedings IEEE*, pp. 191-196, 1995.

[11] D.P. Skinner and R.E. Newnham, "Flexible Composite Transducer," *Mat. Res. Bull.*, vol. 13, pp. 599-607, 1978.

[12] T.R. Gururaja, W.A. Schulze, L.E. Cross, R.E. Newnham, B.A. Auld, and Y.J. Wang, "Piezoelectric Composite Materials for Ultrasonic Transducer Applications. Part I: Resonant Modes of Vibration of PZT Rod-Polymer Composites," *IEEE transactions on sonics and ultrasonics*, vol. SU-32, no. 4, pp. 481-497, 1985.

[13] H.P. Savakus and K.A. Klicker, "PZT-Epoxy Piezoelectric Transducers: A Simplified Fabrication Procedure," *Materials research bulletin*, vol. 16, pp. 677-680, 1981.

[14] G. Kossoff, "The Effects of Backing and Matching on the Performance of Piezoelectric ceramic Transducers," *IEEE transactions on sonics and ultrasonics*, vol. SU-13, pp. 20-30, 1966.

[15] J.W. Hunt and M. Arditi, "Ultrasound Transducers for Pulse-Echo Medical Imaging," *IEEE transactions on bio-medical engineering*, vol. BME-30, no. 8, pp. 453-481, 1983.

[16] S. Saitoh, T. Kobayashi, K. Harada, S. Shimanuki, and Y. Yamashita, "Simulation and Fabrication Process for a Medical Phased Array Ultrasonic Probe using a $O.91Pb(Zn_{1/3}Nb_{2/3})O_3$-$0.09PbTiO_3$ Single Crystal," *Japanese journal of applied physics*, vol. 37, no. 5, pp. 3053-3057, 1998.

[17] G. Hayward and C.J. MacLeod, "A systems model of the thickness mode piezoelectric transducer," *The journal of the Acoustical Society of America*, vol. 76, no. 2, pp. 369-382, 1984.

[18] C.S. Desilets and J.D. Fraser, "The Design of Efficient Broad-Band Piezoelectric Transducers," *IEEE transactions on sonics and ultrasonics*, vol. SU-25, no. 3, pp. 115-125, 1978.

[19] F.S. Foster, L.K. Ryan, and D.H. Turnbull, "Characterization of Lead Zirconate Titanate Ceramics for Use in Miniature High-Frequency (20-80 MHz) Transducers," *IEEE transactions on ultrasonics, ferroelectrics and frequency control*, vol. 38, no. 5, pp. 446-453, 1991.

[20] A. Fukumoto, "The application of piezoelectric ceramics in diagnostic ultrasound transducers," *Ferroelectrics* , vol. 40, pp. 217-230, 1982.

[21] Splitt, A.G. Piezocomposite Transducers - a Milestonde for Ultrasonic Testing. 1997.
Ref Type: Conference Proceeding

[22] G.S. Kino and C.S. Desilets, "Design of slotted transducer arrays with matched backings," *Ultrasonic Imaging*, vol. 1, pp. 189-209, 1979.

[23] J.H. Goll, "The Design of Broad-Band Fluid-Loaded Ultrasonic Transducers," *IEEE transactions on sonics and ultrasonics*, vol. SU-26, no. 6, pp. 385-393, 1979.

[24] G. Hayward and M.N. Jackson, "Discrete-Time Modeling of the Thickness Mode Piezoelectric Transducer," *IEEE transactions on sonics and ultrasonics*, vol. SU-31, no. 3, pp. 137-150, 1984.

[25] R.G. Swartz and J.D. Plummer, "Integrated Silicon-PVF2 Acoustic Transducer Arrays," *IEEE transactions on electron devices*, vol. ED-26, no. 12, pp. 1921-1931, 1979.

[26] T. Ikeda, *Fundamentals of Piezoelectricity* Oxford: Oxford University Press, 1989.

[27] M.D. Sherar and F.S. Foster, "The Design and Fabrication of High Frequency Poly(vinyldene fluoride) Transducers," *Ultrasonic Imaging*, vol. 11, pp. 75-94, 1989.

[28] K.W. Kwok, H.L.W. Chan, and C.L. Choy, "Evaluation of the Material Parameters of Piezoelectric Materials by Various Methods," *IEEE transactions on ultrasonics, ferroelectrics and frequency control*, vol. 44, no. 4, pp. 733-742, 1997.

[29] Y. Yiquan and S. Binwen, "A New Multilayer Planar PVDF Standard Hydrophone and its Applications," *IEEE transactions on ultrasonics, ferroelectrics and frequency control*, vol. 42, no. 5, pp. 958-963, 1995.

[30] T. Bui and H.L.W. Chan, "Specific acoustic impedances of piezoelectric ceramic and polymer composites used in medical applications," *The journal of the Acoustical Society of America*, vol. 83, no. 6, pp. 2416-2421, 1988.

[31] R.S.C. Cobbold, *Transducers for Biomedical Measurements, Principles and Applications* New York: J. Wiley & Sons, Inc., 1974, pp. 168-174.

[32] C.G. Oakley, "Calculation of Ultrasonic Transducer Signal-to-Noise Ratios Using the KLM Model," *IEEE transactions on ultrasonics, ferroelectrics and frequency control*, vol. 44, pp. 1018-1026, 1997.

[33] P. Horowitz and W. Hill, *The Art of Electronics* Cambridge: Cambridge University Press, 1989, pp. 428-455.

[34] R. Krimholtz and D.A. Leedom, "New Equivalent Circuits for Elementary Piezoelectric Transducers," *Electronics letters*, vol. 6, no. 13, pp. 398-399, 1970.

[35] Trzaskos, C.R. Hybrid ultrasonic transducer. [5,389,848]. 1995.
Ref Type: Patent

[36] Borburgh, J. and Feigt, I. Ultrasonic transducer with a plastic piezoelectric receiving layer and a non plastic transmitting layer. [4,354,132]. 1980.
Ref Type: Patent

[37] Maanen, G.A. Acoustic transducer. [4,356,422]. 1980.
Ref Type: Patent

[38] Bui, T.S. and Sherlock, J.A. Ultrasound transducer for enhancing signal reception in ultrasound equipment. [4,427,912]. 1984.
Ref Type: Patent

[39] Ricketts, D. Composite transducer. [4,737,939]. 1988.
Ref Type: Patent

[40] Aplac Solutions Corporation. Aplac. [7.60]. 2000.
Ref Type: Computer Program

Chapter 4

Materials and methods

4.1 Introduction

In this section a brief outline of this chapter is presented, preceded by the reasons to use two transducer types, i.e. the single and multi-element transducer, and a large and small realization of both types. The large transducers were made to verify the principle of the multi-element transducer, i.e. the enhancement of the *SNR*. The small transducers have more realistic dimensions but are more difficult to process, whereas signal processing is more complex.

Consider two piezoelectric elements with dimensions of 20 mm × 20 mm and 4 mm × 4 mm called the large and small transducer, respectively. If the first thickness resonance frequency of both transducers is 7 MHz and the sound velocity in the 1 and 2 direction (see figure 4–1) is 4000 m/s then the width resonances become 200 kHz and 1 MHz for the large and small transducer, respectively. Also, additional resonances that are a multiple of the stated resonances will occur. The influence of width and length resonances will thus interfere less with the thickness resonance for the large transducer than for the small transducer. Therefore, a set of large transducers was made to be able to perform measurements with a reduced influence of width and length resonances. A schematic diagram of the processed ceramic transducers is listed in table 4–1.

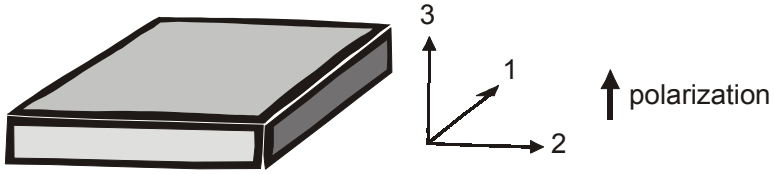

Figure 4–1 *Standard notation for translation displacement of a piezoelectric transducer.*

Two single-element transducers have been realized with areas of 20 mm × 20 mm and 4 mm × 4 mm. Two multi-element transducers were made as well: one consisting of 4 elements and one having 16 elements. The first is easy to fabricate and four signals can be processed faster than 16. For the initial ex-

periments this transducer should be sufficient to verify the noise reduction in the summed output signal of multi-element transducers.

Table 4–1 Schematic diagram of the processed transducer types and sizes.

	type	
size	**single**	**multi**
large	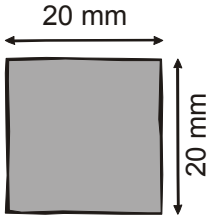	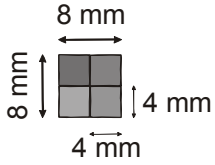
small	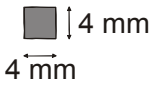	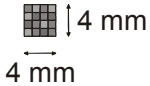

The measurement setup is determined by the measurements that are relevant for a sufficient characterization of the device, being the determination of the impedance and the pulse-echo response.

The noise was obtained by measuring the pulse-echo response (time domain) and calculating the rms value of the signal after the ringing diminishes and before the echo appears.

The pulse-echo response from a 'perfect' reflector was measured, i.e. a water-air interface, to compare the various transducer types. For testing the transducer performance a phantom of the spinal cord, a cylinder of silicone rubber, was used. All experiments were carried out at room temperature (25 °C).

4.2 Device processing

All the piezoelectric transducers used were made of PXE-5, a piezoelectric ceramic made by Philips. The chemical composition of PXE is Pb (ZrTi) Ox (lead titanate zirconate) with some minor dopants of, for example La, Sr or Fe and is listed in table 4–2.

Table 4–2 PXE-5 main composition (weight percent).

symbol	**percentage**
PbO	66 %
ZrO_2	21 %
TiO_2	11 %

A PXE-5 plate of 74 mm × 43 mm was used to process the large single-element transducer, whereas the other transducers were made of plates with an area of (4±0.15) mm × (4±0.15) mm. The piezoelectric plates all have a thickness of (0.3±0.05) mm and are poled at the factory; the positive pole is marked. The electrodes made of nickel, combined with some chromium, have a thickness of about 0.5 µm.

4.2.1 Single element transducer

Two sizes single-element transducers were made: 4 mm × 4 mm and 20 mm × 20 mm, the small and large transducer, respectively. The small transducer was made using the standard 4 mm × 4 mm plates. The larger transducer was obtained by sawing the plate of 74 mm × 43 mm with a diamond saw with a thickness of 70 µm. figure 4–2 shows a cross sectional view of the fabrication process of a PXE-5 single-element transducer (1). The wires with a length of 7 cm were soldered to both sides of the elements (2). Then the piezoelectric element was attached to a preprocessed epoxy backing (3).

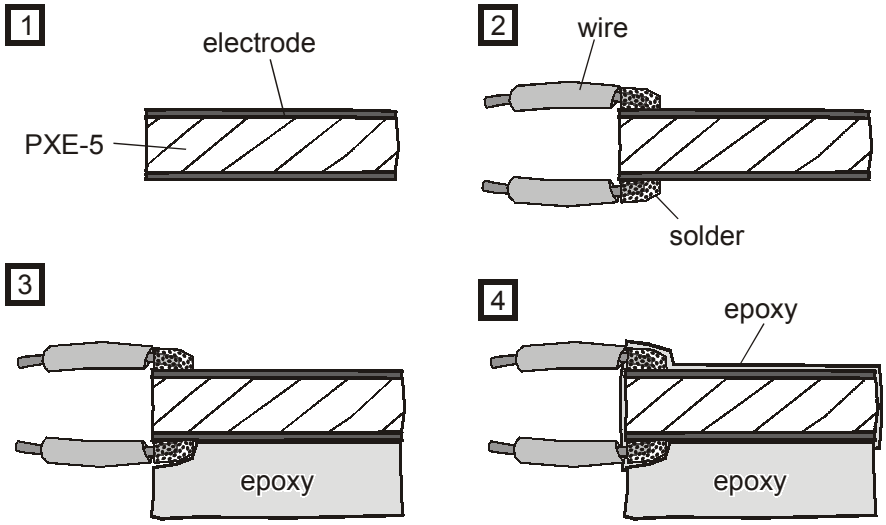

Figure 4–2 Cross sectional view of the fabrication process of the single-element transducer.

This preprocessed epoxy backing was made by pouring Hysol C8-W795/HW796 in a round mould with a diameter of 50 mm. The epoxy was cured at 60 °C for 1 hour. The thickness d_s of the disc was measured at 4 places on the disc as indicated in figure 4–3a. The average thickness was 2650 µm (standard deviation: 90 µm). The roughness of the disc was measured by a DEKTAK surface profiler and found to be between 200 nm and 300 nm. The disc had a mass of 5.97 g, giving a density of 1150 kg/m^3. The sound velocity was obtained by the method depicted in figure 4–3b, which is similar to the method used by Selfridge [1]. The disc was immersed in water together with an ultrasonic transducer. An ultrasonic pulse was emitted towards the epoxy disc. The emitted pulse will be partially reflected by the water-epoxy interface and return to the transducer giv-

ing a first echo signal (signal 1). The second echo signal will occur due to the reflection at the epoxy-water interface (signal 2). This signal has traveled twice trough the epoxy disc and thus the sound velocity v_s in the disc can be written as:

$$v_s = \frac{2d_s}{t_s} \tag{4–1}$$

where t_s is the time between the successive pulses. The measured time t_s was 2.04 µs, which results in a sound velocity of 2600 m/s. Together with the measured density the acoustic impedance of the backing then becomes 3 MRayl. A square of 20 mm × 20 mm was cut out of the epoxy disc to create the epoxy backing for the transducer.

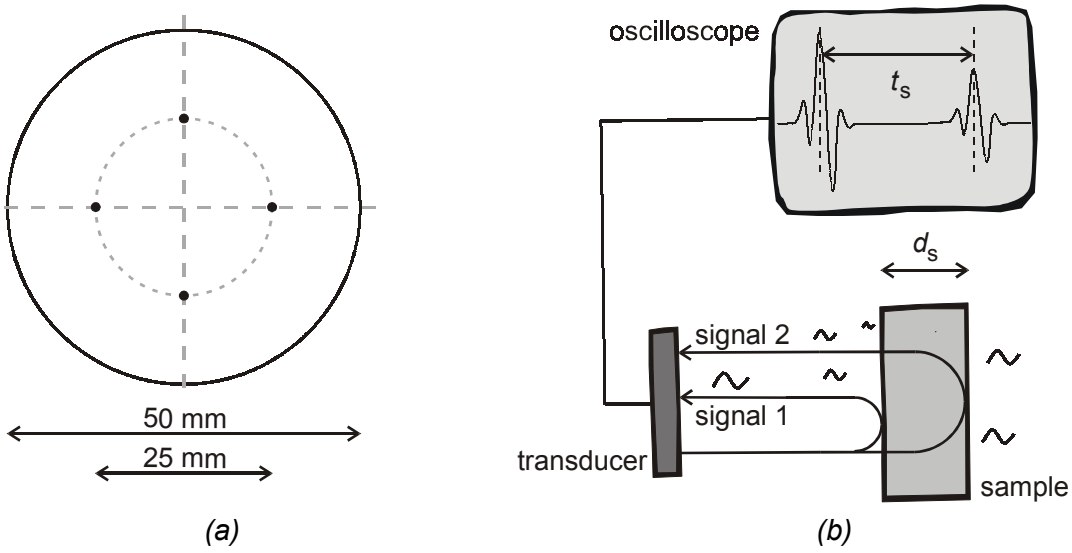

Figure 4–3 *(a) top view of the preprocessed backing with the points where its thickness was measured and (b) the method to measure the sound velocity of the backing (only the signal paths of interest are shown; transit signals are omitted).*

Epoxy was also used to adhere the backing to the transducer element. Subsequently, the epoxy was cured at 60 °C for one hour. Finally, the top electrode was covered by a thin layer (≈ 40 µm) of epoxy, and cured at 60 °C for 1 hour (figure 4–2 (4)). A photograph of the large device is shown in figure 4–4.

Figure 4–4 *Photograph of the large single-element PXE-5 transducer with an epoxy backing.*

4.2.2 Multi-element transducer

Two different multi-element transducers were realized:

- the large multi-element transducer consisting of 4 elements with an area of 4 mm × 4 mm per element, and
- the small multi-element transducer consisting of 16 elements with an area of 1 mm × 1 mm per element.

Fabrication of the large multi-element transducer is similar to that of the single element transducers. Two approximately 17 cm long wires were soldered to both electrodes of a 4 mm × 4 mm PXE-5 element. This was done for four elements. Then the elements were glued onto a preprocessed epoxy (Hysol) backing using a cyanoacrylate adhesive from Pattex. Finally, the elements were covered with epoxy and cured at 60 °C for 1 hour. A picture of the realized multi-element transducer is shown in figure 4–5.

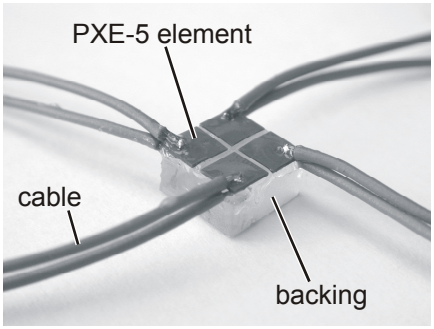

Figure 4–5 Photograph of the large multi-element transducer.

The fabrication process of the small multi-element transducer, depicted in figure 4–6, is more complicated, because of the size of the individual elements and the number of connections to be made. The starting point for this transducer is a 4 mm × 4 mm transducer (PXE-5) (step 1). This element is put on SWT 20 sawing foil (Nitto Denko) (step 2) and diced into 16 elements (step 3) using a diamond saw with a thickness of 70 µm. The size of the individual elements is approximately 1 mm × 1 mm. Next the diced elements were attached on a printed circuit board (PCB) using conductive silver epoxy; this electrode is the common electrode. Subsequently, bond wires were attached to the individual elements and contact was made to the common electrode (step 5). Finally, epoxy was applied over the elements (step 6) to isolate the elements and the bond wires from any liquid.

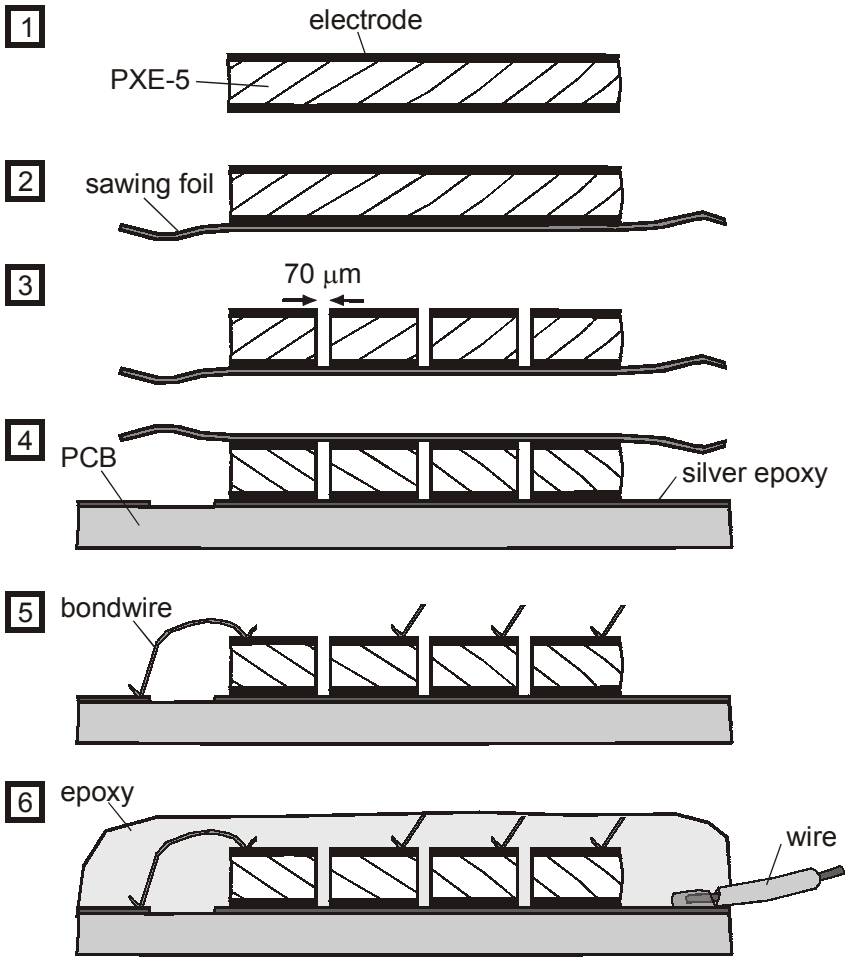

Figure 4–6 *Transducer fabrication process of the small multi-element transducer consisting of 16 elements: (1) the PXE-5 element (2) on sawing foil and (3) diced after which it is (4) glued on the PCB and (5) the individual elements are connected to the copper by bond wires and finally (6) the transducer is encapsulated with epoxy.*

4.3 Measurement setup

4.3.1 Impedance analysis

The emphasis of the transducer performance lays on the *SNR* of the pulse-echo response. Therefore, the transducer performance at its resonance frequency is important, because at this frequency the signal response reaches its maximum magnitude at a constant input level. To determine the resonance frequency of the transducer its input impedance was measured using the HP 4194A Gain-Phase/Impedance Analyzer with the HP16047D test fixture. This simple setup is shown in figure 4–7. The impedance data is transferred over the IEEE-488 bus to a PC. The impedance analyzer is set to measure 401 data points over a frequency range from 100 Hz to 15 MHz and another frequency sweep from 100 Hz to 40 MHz was made. To compare the measured data with the simulation results

the impedance of the cables between the transducer and the impedance analyzer must be taken into account. This can be done by modeling the cables in the simulation. The cable impedance will play a role in modeling of the transducer especially at higher frequencies (>10 MHz). Therefore, the cable impedance will be modeled by a series inductor (L_{cable}) and series resistor (R_{cable}). The clamped capacitance C_0 of the transducer is very large compared to a parallel parasitic capacitance due to the cables and is therefore omitted. The model for this circuit is depicted in figure 4–8. The *source* is the impedance analyzer (HP 4194A).

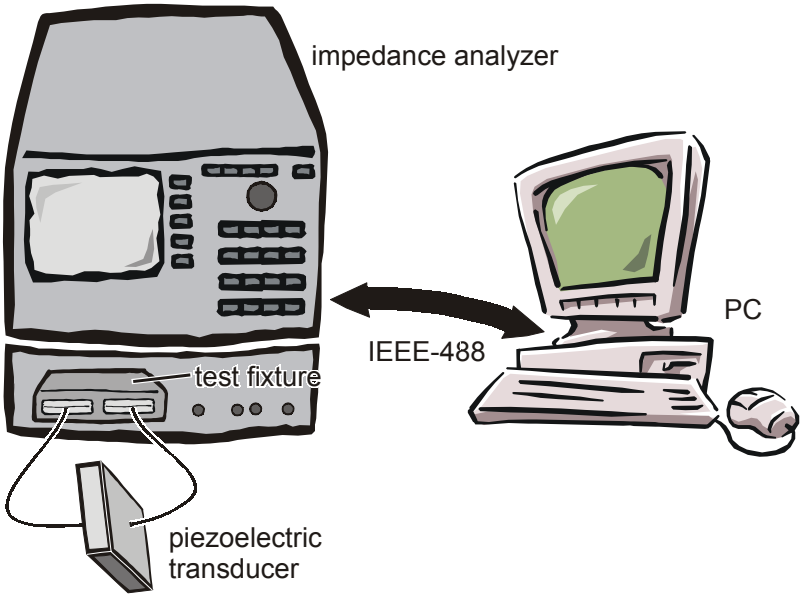

Figure 4–7 Measurement setup to determine the transducer's input impedance using an HP 4194A Gain-Phase/Impedance Analyzer with the HP16047D test fixture. The data is transferred to the PC over an IEEE-488 bus.

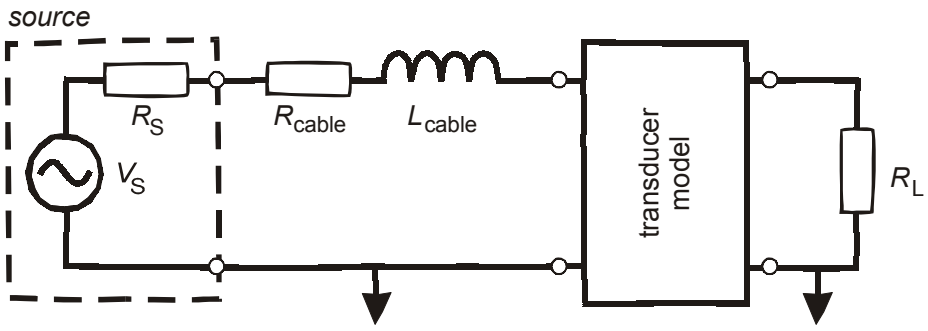

Figure 4–8 Model for the transducer including the cable impedance and the impedance analyzer as the source.

4.3.2 Insertion loss

Measuring the insertion loss of a transducer is ideally performed by a continuous wave measurement. However, this is not a practical solution using one transducer as the emitter and receiver. Therefore, a pulse train consisting of a number of continuous sine cycles will be applied to the transducer. The number of

cycles required is determined by the transducer parameters, e.g. the transducer area. The number of cycles required for a specific transducer can be found by simulation.

Figure 4–9 depicts the pulse-echo measurement setup for a single-element transducer. The pulse function generator (HP 8111A) applied a pulse train consisting of *n* cycles. The frequency of the applied pulse train was swept. The transducer was immersed in water, facing the water-air interface at a distance of approximately 1 cm. At this interface most of the incident power will be reflected towards the transducer due to the large difference between the acoustic impedance of water and air, 1.5 MRayl and 400 Rayl, respectively. The signal reflection coefficient is 99.9 %. The attenuation coefficient of water has an approximately linear dependence on frequency, i.e. the higher the frequency the larger the attenuation. The attenuation coefficient of water is approximately 0.002 dB/-(cm·MHz). Thus, at 10 MHz the attenuation over a distance of 2 cm will be 0.04 dB, which will therefore be neglected.

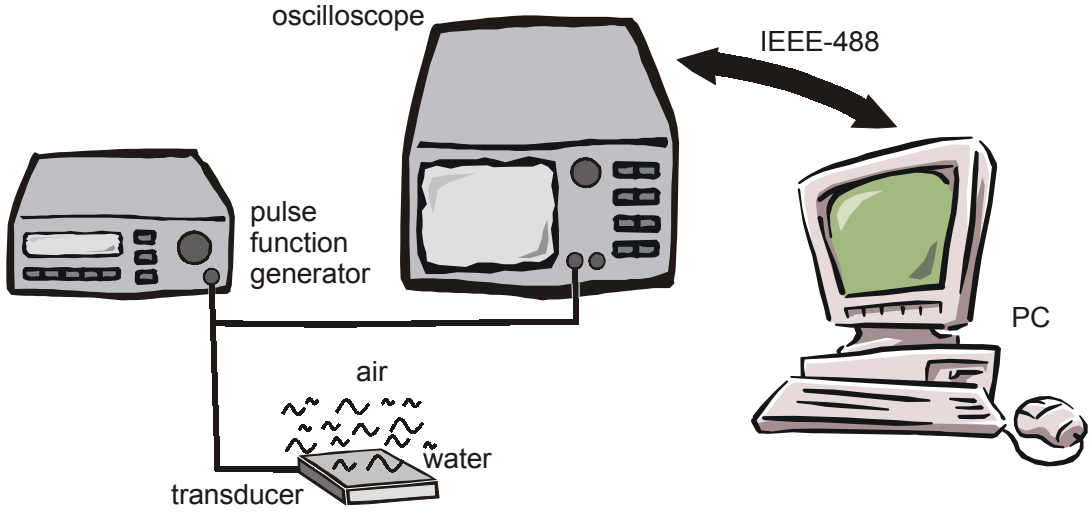

Figure 4–9 Measurement setup to measure the insertion loss and the pulse-echo response of a single piezoelectric transducer. The data is transferred to the PC over an IEEE-488 bus.

To ensure that the emitted ultrasonic wave will not diverge and a considerable amount of power will therefore not reflect on the transducer, the water-air interface should be well within the near field. The near field or Fresnel diffraction region is the region where the emitted waves form a plane-wave front normal to the direction of propagation. The far field or Fraunhofer region starts where the ultrasound beam starts to diverge. The length of the near field L_{near} can be written as:

$$L_{near} = \frac{D^2 - \lambda^2}{4\lambda} \approx \frac{D^2}{4\lambda} \qquad (4–2)$$

where D is the diameter of the transducer and λ the wavelength of the emitted wave. For the small transducer D=4 mm at a frequency of 10 MHz λ=150 µm,

the near field is approximately 2.6 cm. For the large single element transducer (D=2 cm) the near field is more than 65 cm.

4.3.3 Measurement setup for a single element transducer

Pulse-echo measurements are more complicated than impedance measurements, although the principle is simple: Induce an ultrasonic wave by applying an electrical pulse to the piezoelectric transducer and measure the reflected ultrasonic wave that will excite the transducer and produce an electrical echo signal. Figure 4–9 depicts the pulse-echo measurement setup for a single-element transducer. The pulse function generator (HP 8111A) excited a single sine pulse with the appropriate frequency to the transducer. The peak-peak amplitude of the pulse was 15 V. The internal impedance of the arbitrary waveform generator is 50 Ω. The trigger of the generator is set to internal if averaging is required or to manual if only one shot is required.

The transducer was immersed in water, facing the water-air interface. At this interface most of the incident power will be reflected towards the transducer due to the large difference between the acoustic impedances of water and air, 1.5 MRayl and 400 Rayl, respectively. The signal reflection coefficient is 99.9 %. The excitation and echo signal are measured by the oscilloscope (HP51520A) and transferred to the PC over the IEEE-488 bus. The input impedance of the oscilloscope is 1 MΩ parallel to 8 pF. The electrical equivalent circuit of the measurement setup above is presented in figure 4–10. The 50 Ω parallel to the 1 MΩ resistor is not ideal for maximum signal transfer as used for pulse-echo experiments, but it can be used for insertion loss measurements. Therefore, an additional experiment was performed in which the influence of the load resistance on the signal amplitude was examined. A setup similar to the one used for the multi-element transducer was used. Two single element transducers were immersed in water and the receiving element was connected to the scope with an input impedance of either 50 Ω or 1 MΩ.

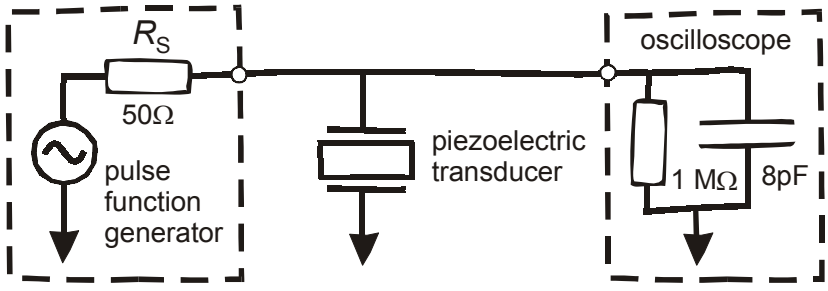

Figure 4–10 Electrical equivalent circuit of the measurement setup shown in figure 4–9.

To perform delay time measurements, the distance between the transducer and the air-water interface was varied by adding or removing water with a pipette. If

the transducer is immersed in a beaker with radius r the variation in distance Δd between the water-air interface and the transducer can be written as:

$$\Delta d = \frac{\Delta v}{\pi r^2} \tag{4–3}$$

where Δv is the volume of water added or removed.

4.3.4 Measurement setup for a multi-element transducer

The measurement setup for a multi-element transducer is more complicated than for a single-element transducer. A setup is discussed in which two transducers are used: one for emitting an ultrasonic pulse that is received by the second transducer, i.e. the multi-element transducer. The presented setup was used for pulse-echo measurements as well as for insertion loss measurements.

The two transducers were positioned opposite of each other and immersed in water as shown in figure 4–11. The transducers were aligned such that the signal transfer is maximal. A single element transducer was used as the actuator and was driven by the pulse generator (HP 8111A) with a single sine wave with a peak-peak amplitude of 15 V. The induced ultrasonic wave propagates towards the multi-element transducer where it is detected by all the elements. The response of the elements was recorded in pairs (two elements at once) by the oscilloscope (HP 54520A). Subsequently, the signals of the individual elements can be processed, e.g. added or filtered.

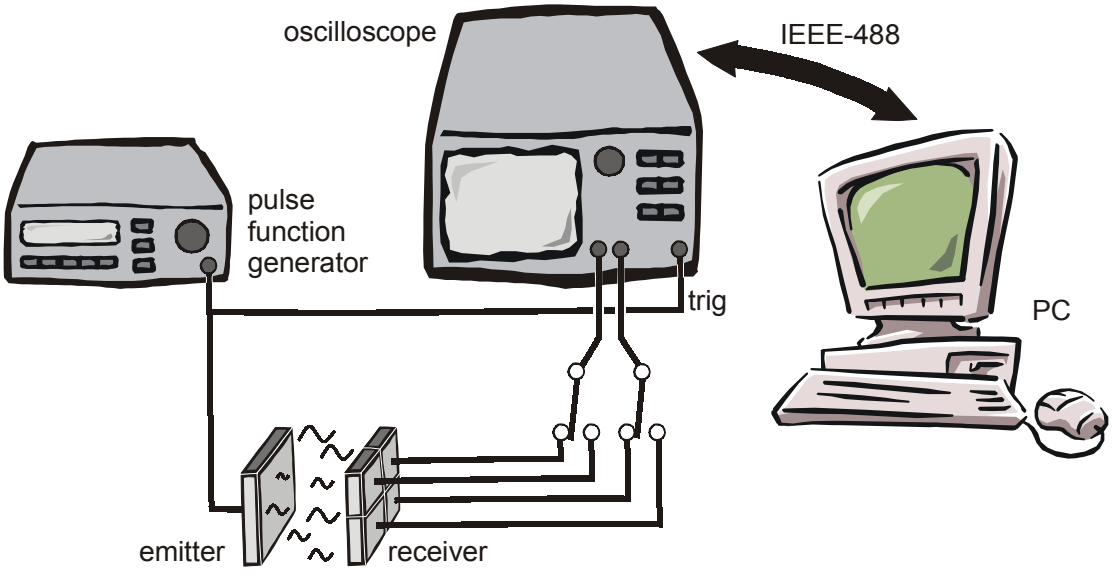

Figure 4–11 Measurement setup to measure the response of a multi-element transducer on an ultrasonic pulse of a separate single-element transducer.

4.3.5 Phantom of the spinal cord

Instead of the air-water interface a more realistic (CSF-spinal cord) reflecting interface was used. For laboratory experiments a phantom of the spinal cord in

CSF, with realistic dimensions and acoustic impedance, was used. The spinal cord phantom consists of a cylinder of silicone rubber with a diameter of 9.5 mm, immersed in water. The dimensions were obtained from the MRI study [2].

Table 4–3 shows that the acoustic impedance of silicone rubber is close to the value of soft biological tissue. The reflection coefficient of silicone rubber immersed in water is approximately 12 %. The transducer is connected as shown in figure 4–12. The spinal cord phantom was attached to a precision manipulator with a resolution of 0.5 mm. The manipulator was used to vary the distance *d* between the transducer and the spinal cord phantom.

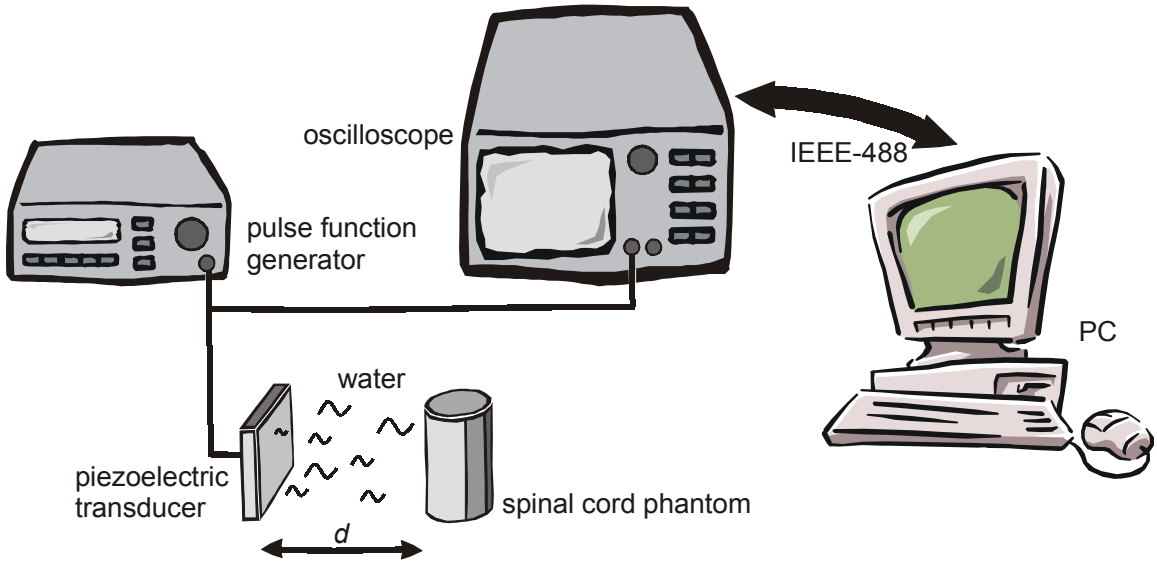

Figure 4–12 Measurement setup for delay time versus distance measurements with a silicone rubber spinal cord phantom.

Table 4–3 Acoustic impedances of some materials and biological tissue.

substance	acoustic impedance [MRyal]
water [3]	1.52
soft tissue (except muscle) [3]	1.35 - 1.68
perspex [3]	3.2
Sylgard silicone rubber [1]	1.04 - 1.34
silicone rubber [4]	1.91

4.4 Measurement protocol

4.4.1 Transducer input impedance

The transducer input impedance was measured using the HP 4194A Gain Phase/-Impedance Analyzer. The number of points was set to 401 (maximum) and the frequency range was set to either 6 MHz to 9 MHz or 100 Hz to 15 MHz. The averaging of the apparatus was set to 1 and the integration time to short.

4.4.2 Insertion loss

The input impedance of the oscilloscope was set to 50 Ω. A pulse-train was applied to the transducer for measuring the insertion loss. The pulse train generated by the pulse function generator was measured by the oscilloscope without the transducer connected and averaged 256 times and send to the PC. Afterwards the exact frequency and amplitude of the pulse-train can be obtained. Subsequently, the transducer was connected to the generator and the reflected pulse train was recorded by the oscilloscope and averaged also 256 times before it was send to the PC. In case of the single element transducer, see figure 4–9, the input impedance of the oscilloscope was set to 1 MΩ. The input impedance of the oscilloscope was not changed (50 Ω) for the multi-element transducer setup, see figure 4–11.

The first resonance frequency is approximately 7 MHz. The insertion loss of the large single element transducer was measured from 5 MHz to 10 MHz with a step size of 500 kHz (total 11 points). For the other transducers the frequency range was 4 MHz to 10 MHz. The step was also 500 kHz resulting in 13 points. The number of cycles for the pulse-train was set to 40 for the large transducers and 20 cycles were taken for the small transducers.

4.4.3 Pulse-echo response

For pulse-echo response measurements two types of experiments can be distinguished: single shot and averaging. For the single shot experiment, the trigger of the function generator was set to single and the trigger of the oscilloscope was set to triggered. The oscilloscope measured real time and 2^n samples at each trigger. At t_0 the function generator was triggered. To determine the time of arrival the time corresponding to the maximum of the echo signal was obtained.

For the averaging type of measurements, the trigger of the function generator was set to internal and the scope was set to repetitive to enable averaging. The number of averages was set to 256 and the number of points was 500.

4.4.4 Signal-to-noise ratio

To obtain the *SNR* of the transducer response signal it is necessary to first find the rms value of the noise and the peak-peak voltage of the echo signal, see equation (3–8) on page 49. A typical transducer signal is depicted in figure 4–13. On the left side the actuation of the transducer is present followed by ringing of the transducer. Then a period follows in which the noise is presented without any other signals. Finally, the echo appears. The noise was calculated in the period between ringing and presence of the echo. The rms noise $E_{n,rms}$ can be obtained from:

$$E_{n,rms} = \sqrt{\frac{1}{T}\int_0^T {V_{noise}}^2 dt} \cong \sqrt{\frac{1}{n}\sum_{i=0}^{n-1}\left(V_{noise,i}\right)^2} \qquad (4–4)$$

For the *SNR* measurements 20 or 100 single shot responses were obtained for the small multi-element transducer and the other transducers, respectively. Each response consisted of 8192 samples and the sample rate was set to 500 MSa/s. These responses were averaged to calculate the peak-peak amplitude V_{pp} of the echo. Then, for each response the rms noise was calculated and the *SNR* for each response was obtained using:

$$SNR = 20\log\left(\frac{V_{pp}}{E_{n,rms}}\right) \qquad (4–5)$$

Two types of *SNR* experiments were performed. First, the *SNR* of the echo from the spinal cord phantom was obtained using the small single element transducer. Second, the *SNR* of the multi-element transducer was measured for parallel and series connection of the elements.

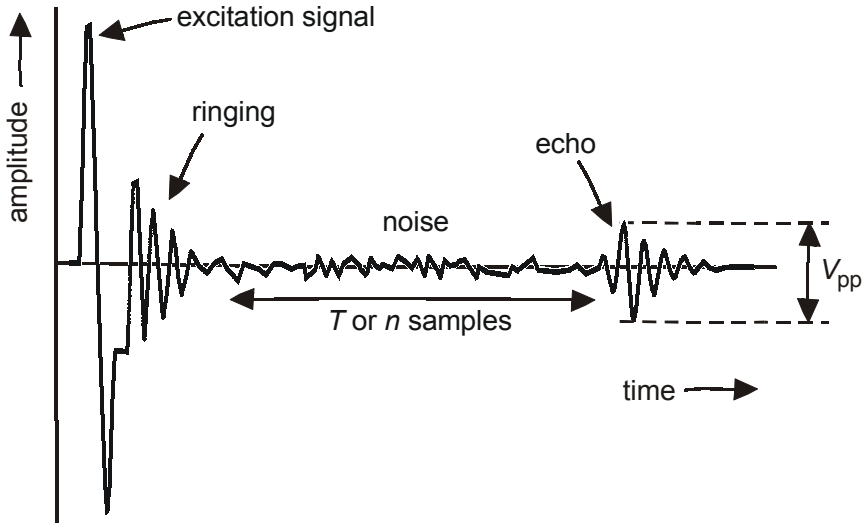

Figure 4–13 Typical transducer signal consisting of the excitation signal plus ringing, noise and the echo.

The *SNR* experiments were performed for the single element transducer with the spinal cord phantom as the reflector. The distance between the transducer and the spinal cord phantom was varied between 4 mm and 10 mm. The setup used for this experiment is shown in figure 4–12. The pulse function generator (HP 8111A) applied a single sine wave with a frequency of 6.8 MHz and a peak-peak amplitude of 15 V to the transducer.

Another set of *SNR* experiments was performed for the small and large multi-element transducer with the experimental setup shown in figure 4–11. The transmitting transducer was either the large or small single element transducer corresponding to the size of the multi-element transducer. The distance between the single and multi-element transducers was set to approximately 1 cm. A single sine wave with a frequency of 8.7 MHz and a peak-peak amplitude of 15 V was applied by the pulse function generator (HP 8111A) to the single element transducer. The input impedance of the oscilloscope was set to 1 MΩ. The experiments were carried out with each element connected to the oscilloscope's input and with the elements connected in parallel.

References

[1] A.R. Selfridge, "Approximate Material properties in Isotropic Materials," *IEEE transactions on sonics and ultrasonics*, vol. SU-32, no. 3, pp. 381-394, 1985.

[2] J. Holsheimer, J.A. Den Boer, J.J. Struijk, and A.R. Rozeboom, "MR Assessment of the Normal Position of the Spinal Cord in the Spinal Canal," *American Journal of Neuroradiology*, vol. 15, pp. 951-959, 1994.

[3] P.N.T. Wells, *Ultrasonics in Clinical Diagnosis* Edinburg: Churchill Livingstone, 1977.

[4] G.L. Wojcik and D.K. Vaughan, "Time-domain modeling of composite arrays for underwater imaging," *IEEE Int. Ultrasonics Symp. Proc.*, pp. 1027-1032, 1994.

Chapter 5

Experimental results and discussion

5.1 Introduction

In this chapter experimental results together with simulations will be presented and discussed. First, the transducer impedance will be described. The simulated impedance will be fitted to the measured impedance by varying some material parameters to obtain the best possible fit. Next, the measured and simulated insertion loss will be presented using the parameters obtained from the impedance analysis. Subsequently, the pulse-echo response will be presented both from simulations and measurements. The pulse-echo measurement data were used to calculate the signal-to-noise ratio.

5.2 Transducer impedance analysis

The transducer impedance was measured and the model parameter values were varied to fit the experimental data. The model consists of the KLM model, modified as discussed in chapter 2. A cable impedance consisting of a resistor and an inductance was added to the model as shown in figure 5–1. The parameter values for PXE-5 that will be used throughout this chapter were already determined in chapter 2 and are listed in table 2–2 (column: step 2). To fit the modeled impedance to the measured data the thickness of the transducer, the backing impedance, the series resistor and series inductance were varied. To obtain the best possible fit the resistance and reactance of the measured and simulated input impedance were compared. First, in the 40 MHz frequency sweep, the reactance was fit by varying the inductance L_{cable}. Second, the simulated resistance was adapted to the measured value by varying the series resistor value R_{cable}.

The value of R_{cable} can easily be obtained by measuring the resistance between the first and second thickness resonance. In the 15 MHz frequency sweeps the thickness of the transducer was varied until the first thickness resonance peaks coincided. The thickness of the transducers is (0.3±0.05) mm. Finally, the acoustic backing impedance Z_{back} was chosen such that the magnitude of the resonance peaks of simulation and measurement matched. The acoustic impedance Z_{front} was equal to Z_{back} except for the large single element transducer, where Z_{front} was set to the acoustic impedance of air. The initial value was taken 3 MRayl as was obtained by the measurement described in subsection 4.2.1 on page 73. For each transducer the resistance and reactance as a function of frequency including the cable impedance will be presented, along with the parameter values that give the best possible fit.

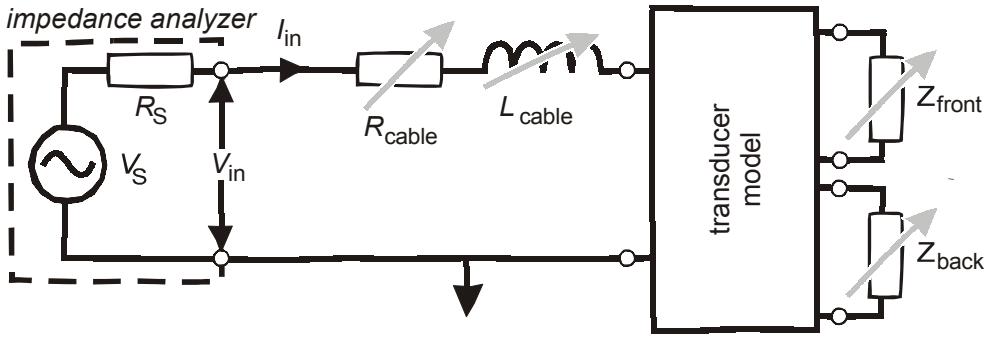

Figure 5–1 Model for matching the simulated input impedance to the measured input impedance. The arrows indicate the parameter values that are varied.

First, the impedance of the large (20 mm × 20 mm) transducer will be discussed followed by the small (4 mm × 4 mm) transducer. After that the impedances of the large and small multi-element transducers will be shown. The impedances of the individual elements as well as the impedance of the connected elements in parallel will be shown.

5.2.1 Large single element transducer

Figure 5–2 shows the measured (dots) and simulated (lines) resistance R (•) and reactance X (▵) of the transducer, in which the cable impedance is included. The values that were found to get the best possible fit are listed in table 5–1.

Table 5–1 Parameters used for modeling the large single element transducer.

parameter	definition	value	unit
L_{cable}	cable inductance	109	[nH]
R_{cable}	cable resistance	3.5	[Ω]
Z_B	acoustic backing impedance	3	[MRayl]
t	thickness	303	[µm]

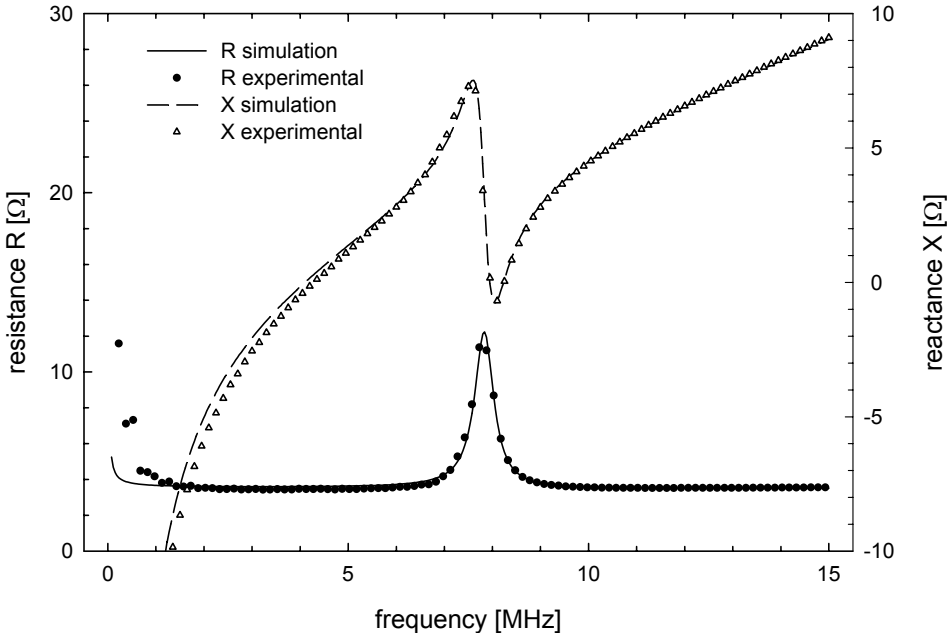

Figure 5–2 Measured and simulated resistance R (●) and reactance X (▲) of the large single element transducer with an epoxy backing and cable.

The acoustic impedance of the front side Z_{front} was set to that of air (400 Rayl). The series inductance L_{cable} has a value of 109 nH and the series resistance a value of 3.5 Ω. This means that the inductance overrules the resistance at frequencies above 5 MHz, and thus plays a role at the first resonance frequency. This effect is illustrated in figure 5–3, where the impedance magnitude of the transducer is shown with and without the cable impedance. For obtaining the real resonance frequencies it is important to compensate for parasitic impedances. However, in a system these parasitic impedances will be present and should therefore be taken into account. Note that the exact value of L_{cable} is very sensitive to the position of the wires. The experimental and calculated data are in good agreement.

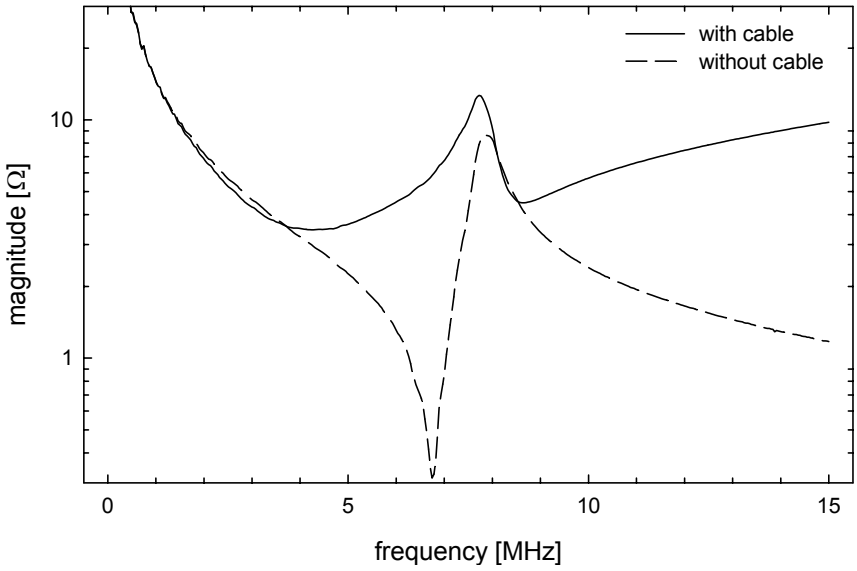

Figure 5–3 Measured impedance magnitude of the large single element transducer with and without the cable impedance.

5.2.2 Small single element transducer

The measured and fitted resistance and reactance of the input impedance of the small single element transducer are shown in figure 5–4. The model parameters for the best fit between simulation and measurement are listed in table 5–2. The deviation of the optimized transducer thickness from the thickness given by Philips is within the error range.

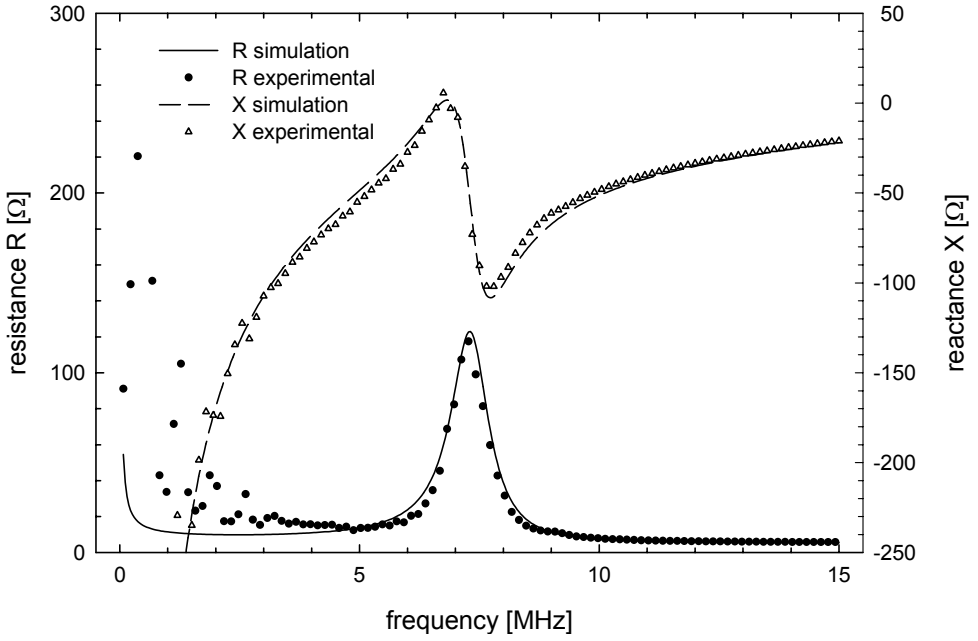

Figure 5–4 Measured and simulated resistance R (•) and reactance X (▵) of the small single element transducer with an epoxy backing and cable.

Table 5–2 Parameters used for modeling the small single element transducer.

parameter	definition	value	unit
L_{cable}	cable inductance	110	[nH]
R_{cable}	cable resistance	5.1	[Ω]
Z_B	acoustic backing impedance	3.5	[MRayl]
t	thickness	324	[µm]

The deviation of acoustic impedance of the backing from the experimentally obtained value can be explained by the following. The influence of the solder area for a small element is much larger than that for large elements. Assume that the transducer area A is 16 mm^2 and that the soldered contact A_{solder} is 1 mm^2. Further, the backing of the transducer is Hysol (3 MRayl) and covers an area A_{Hysol} of 15 mm^2. The average acoustic backing impedance $Z_{back,av}$ can be calculated by:

$$Z_{back,av} = \frac{A_{Hysol}Z_{Hysol} + A_{solder}Z_{solder}}{A} \qquad (5\text{-}1)$$

Selfridge [1] gives an acoustic impedance of 24.2 MRayl for solder. Substituting the appropriate values in equation (5-1) gives an average acoustic backing of 4.3 MRayl. In comparison, a solder area of 1 mm^2 on a 4 cm^2 transducer results in an average acoustic impedance of 3.05 MRayl.

5.2.3 Large multi-element transducer

The measured and simulated resistance and reactance parts of the input impedance of the individual elements of the large multi-element transducer are presented in figure 5–5. The parameters which gave the optimum fit per element are shown in table 5–3. The variation in the acoustic impedance is remarkable, because the same backing was used for all elements. However, the solder area differs per element, which causes a different acoustic backing impedance per element. The acoustic impedance of the backing was chosen such that the simulated values coincided maximally with the experimentally found values.

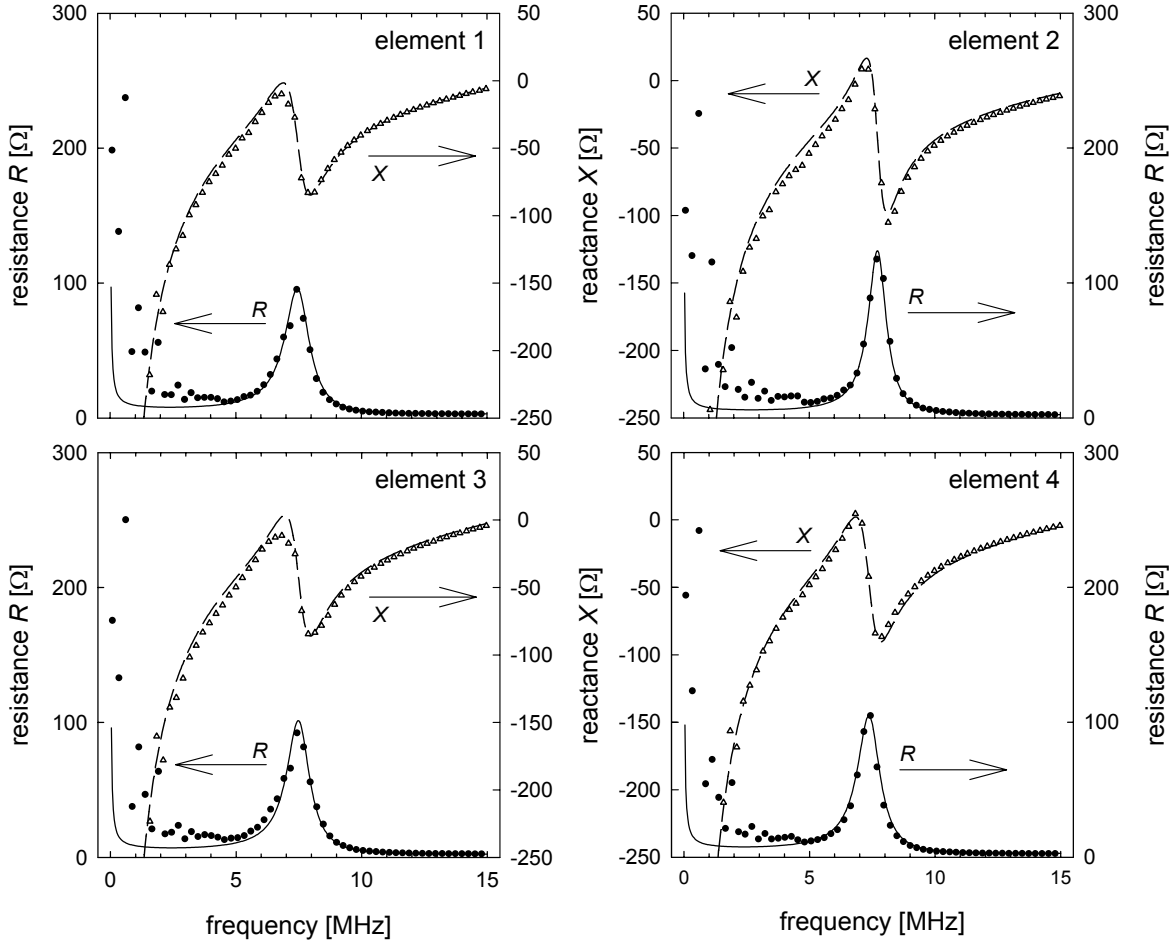

Figure 5–5 Measured (dots) and simulated (lines) resistance and reactance of the individual elements of the large multi-element transducer.

Table 5–3 Parameter values per element used for modeling the large multi-element transducer.

		value of element				
parameter	**definition**	**no. 1**	**no. 2**	**no. 3**	**no. 4**	**unit**
L_{cable}	cable inductance	280	230	310	290	[nH]
R_{cable}	cable resistance	2.7	2.1	2.1	2.5	[Ω]
Z_B	acoustic backing impedance	4.3	3.0	4.0	4.0	[MRayl]
t	thickness	317	307	316	321	[μm]

Next, the impedance of the four elements in parallel was measured and simulated. The graph in figure 5–6 shows the experimentally obtained data. The simulation data was obtained by putting four elements including the model for the connecting wires in parallel, without changing the parameters obtained per element, except the wire inductance that was changed to 460 nH, because the position and orientation changed a lot with respect to the situation in the individual impedance measurement.

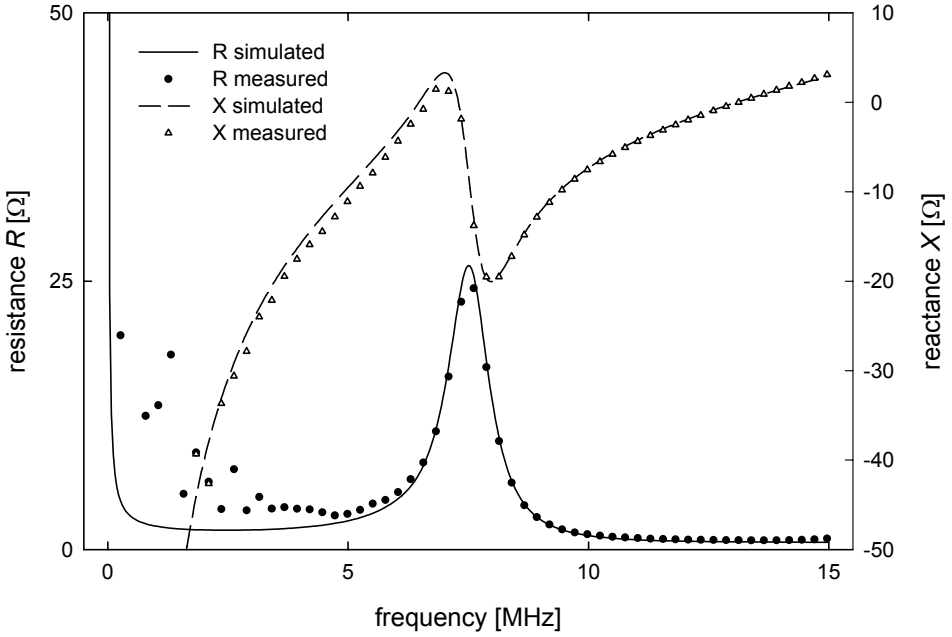

Figure 5–6 Measured (dots) and simulated (lines) resistance and reactance of the individual elements in parallel of the large multi-element transducer.

5.2.4 Small multi-element transducer

The wires to connect the elements of the small multi-element transducer are longer than used for the other transducers and also a bond wire was used. Therefore, the cable inductance will be larger than that of the other transducers.

Due to the small size of the elements the capacitance of the wires becomes significant. For comparison, the clamped capacitance of a 1 mm^2 PXE-5 element is 22 pF, whereas the capacitance of a 16 mm^2 PXE-5 element is 350 pF. Therefore, a load capacitor C_{cable} was added to the cable model as shown in figure 5–7.

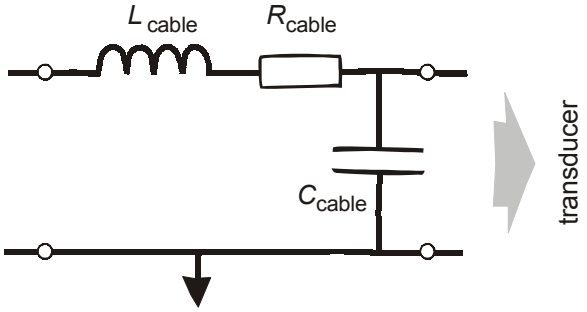

Figure 5–7 Model for the cable impedance of the cables of the small multi-element transducer.

Additionally, the Hysol layer on top of the elements is thicker than for the other transducer and cannot be ignored. The Hysol layer was modeled by a transmission line. The length of the transmission line or thickness of the Hysol is approximately 1.2 mm, the acoustic impedance of the Hysol is 3.0 MRayl, the sound velocity in the Hysol is 2600 m/s (see subsection 4.2.1, page 73) and the attenuation is estimated to be 30 dB/cm. The latter is in correspondence with the observation of Selfridge [1] who reported attenuation constants ranging from 5 dB/cm to 32 dB/cm at 5 MHz for various kinds of epoxies.

The measured and simulated resistance and reactance of the input impedance of four elements out of 16 elements of the small multi-element transducer are presented in figure 5–8. The parameters that gave the optimum fit are listed in table 5–4. The backing impedance of the transducer has a value of 4.4 MRayl, which is close to the value of 5.14 MRayl found by Selfridge [1] for silver epoxy. The same parameter values were used to calculate the impedance of the elements in parallel. The measured and simulated data is shown in figure 5–9. The discrepancy between the curves is not remarkable, since there were also differences for the individual elements. The match at higher frequencies can be improved by changing the inductance value of the cable.

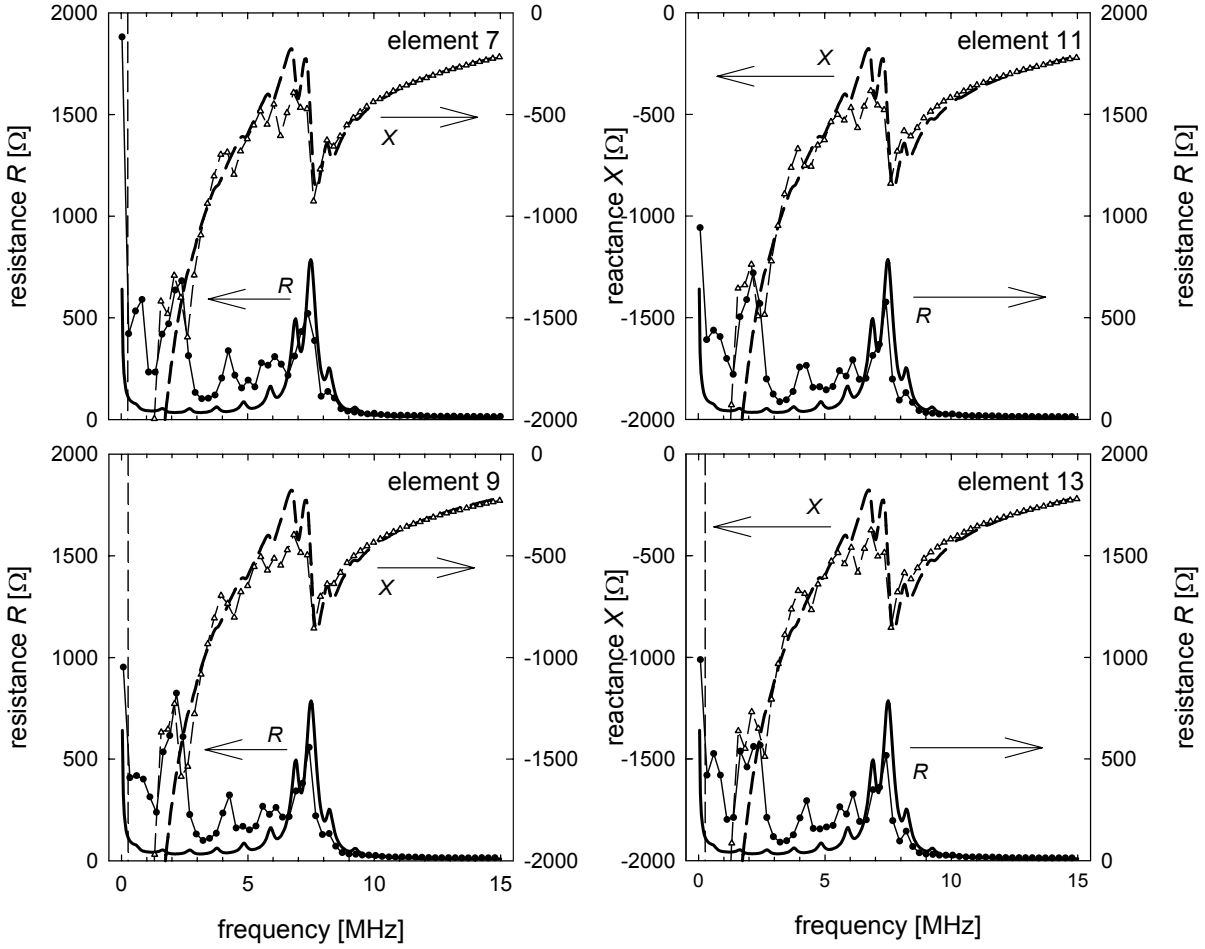

Figure 5–8 *Measured (thin lines + dots) and simulated (thick lines) resistance and reactance of four elements of the small multi-element transducer.*

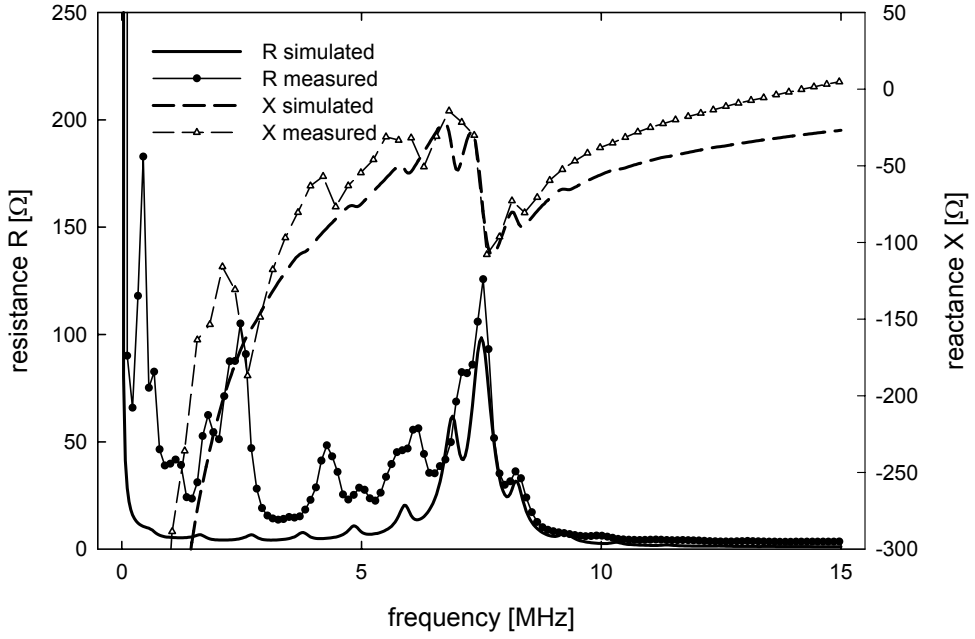

Figure 5–9 *Measured (thin lines + dots) and simulated (thick lines) resistance and reactance of the small multi-element transducer with the elements connected in parallel.*

Table 5–4 Parameter values used for all elements for modeling the small multi-element transducer.

parameter	definition	value	unit
L_{cable}	cable inductance	840	[nH]
R_{cable}	cable resistance	10	[Ω]
C_{cable}	cable capacitance	8	[pF]
Z_B	acoustic backing impedance	4.4	[MRayl]
t	thickness	303	[µm]

5.3 Insertion loss

Before presenting and discussing the experimental data on the insertion loss, the method on how the insertion loss will be measured is presented followed by a subsection on how the measured data was processed before it was used to determine the insertion loss. The large single element was used as an example to present the methods. The frequency at which the insertion loss is minimal is the optimum frequency for the excitation pulse resulting in a maximal signal transfer.

5.3.1 The pulse train method

For insertion loss measurements a continuous sine wave is required. However, this is not a practical solution using one transducer as the emitter and receiver. Therefore, a pulse train consisting of a number of continuous sine cycles will be applied to the transducer. The required number of cycles is determined by the transducer parameters, e.g. the transducer area. An appropriate number of cycles of the frequency of interest must be received to enable a peak-peak amplitude measurement. The required number of cycles is obtained from simulations. The model used for the simulations is shown in figure 2–7. The response to a pulse train consisting of 40 cycles was calculated for the lowest (5 MHz) and highest (10 MHz) frequency and are shown in figure 5–10. The box in both graphs shows over which period of time the peak-peak amplitude was calculated (6 periods of the signal). Also, at nine intermediate frequencies the insertion loss was calculated in the same way. The insertion loss *IL* was calculated by the following ratio, see also equation (3-13):

$$IL = 20\log\left(\frac{V_{out}}{V_{50\Omega}}\right) \tag{5-2}$$

where V_{out} is the peak-peak amplitudes of the received signal and $V_{50\Omega}$ is the peak-peak amplitude of the source signal delivered to a 50 Ω load. This is half of the open-loop peak-peak voltage of the source V_S: $V_{50\Omega} = ½V_S$.

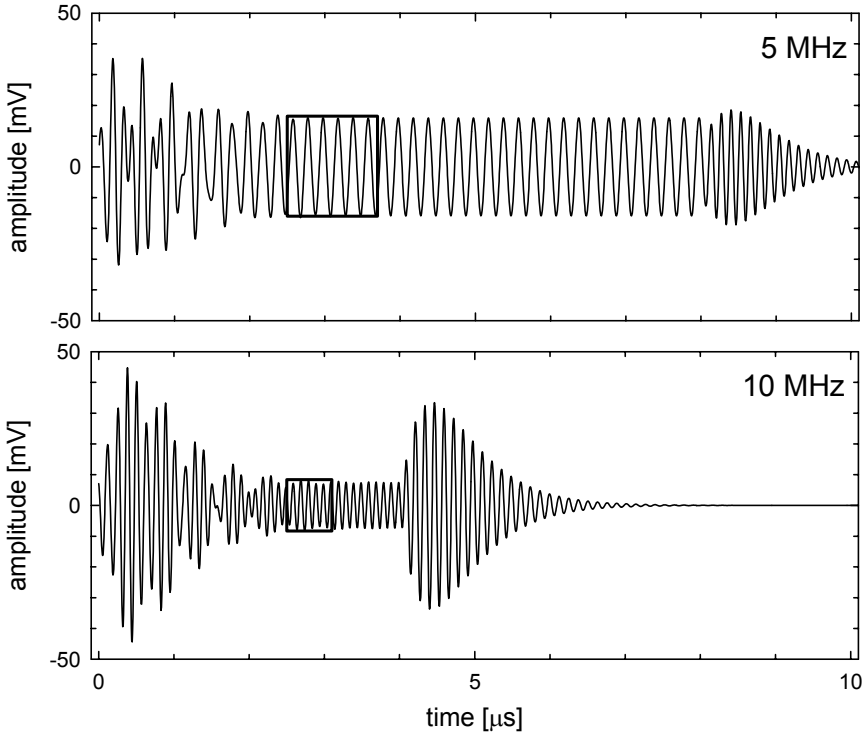

Figure 5–10 Simulated response of a 2 cm × 2 cm PXE-5 transducer to a 5 MHz and a 10 MHz pulse train consisting of 40 pulses with an amplitude of 8 V.

It is also possible to calculate the insertion loss with a continuous wave (AC analysis). The results of both methods are presented in figure 5–11, where the solid line represents the continuous wave method and the diamonds are the points calculated by the pulse train method. The graph clearly shows that both methods give identical results. In conclusion, the simulations show that the pulse train method can be used to obtain the insertion loss of a transducer.

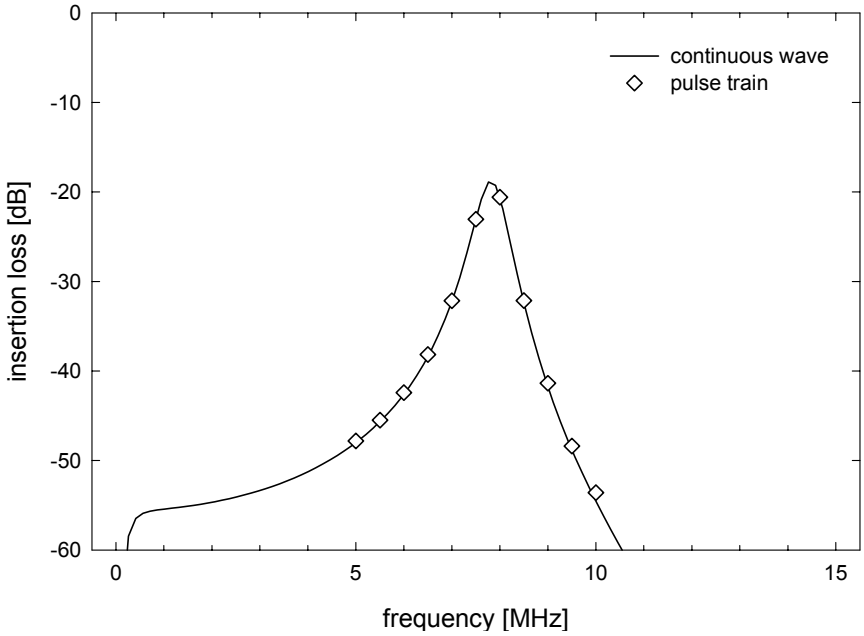

Figure 5–11 Simulated insertion loss of the 2 cm × 2 cm PXE-5 transducer with a continuous wave (line) and by the pulse train method (diamonds).

5.3.2 Data analysis and processing

The measured response of the large single element transducer to a 40-cycle pulse train with a frequency of 10 MHz is presented in figure 5–12 (raw). The measured response contains some unwanted low frequency components. These low frequency components are due to the width and length resonances of the transducer and a DC component due to the fact that the input signal has an offset. To remove these low frequency components the recorded signal was high pass filtered by an ideal filter. This was realized by a Fourier transform of the recorded signal and removing the frequency components lower than 4 MHz. Next, an inverse Fourier transform was applied to obtain the signal in the time domain. In figure 5–12 also the high pass filtered (HPF) signal is shown. From the graph it can be observed that the peak-peak voltage of the filtered signal can be obtained more easily than of the raw data.

The frequency and amplitude of the input signal V_S were measured for each pulse train. Both parameters were calculated over 6 periods. The frequency was determined by measuring the interval between to successive zero crossings (signal goes from negative to positive). The obtained frequencies were averaged.

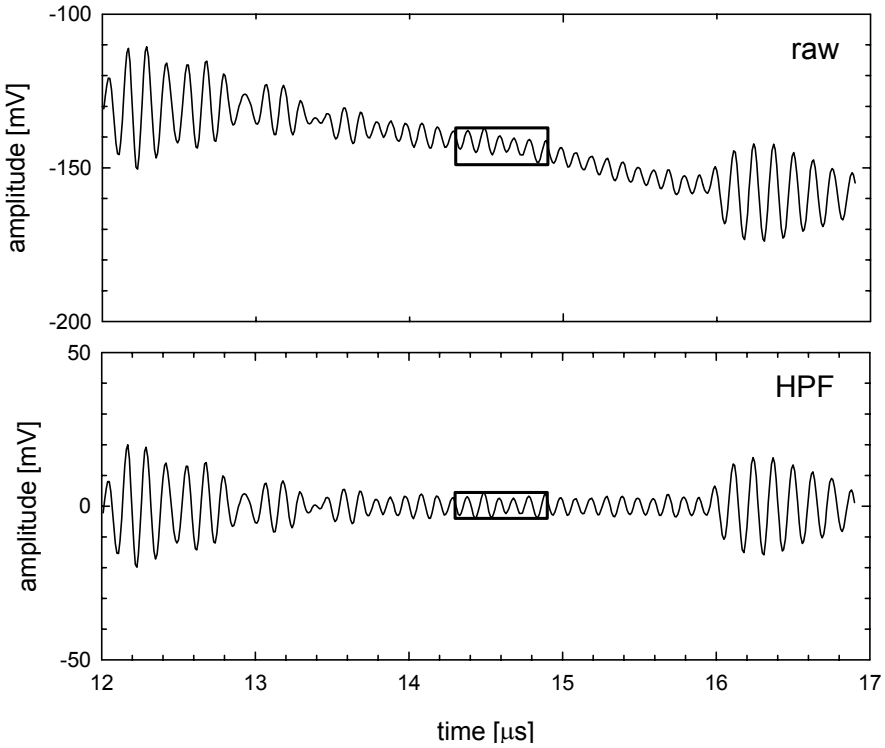

Figure 5–12 Measured (raw) response of the 2 cm × 2 cm PXE-5 transducer to a 10 MHz pulse-train and the high pass filtered (HPF) signal.

The peak-peak amplitude of the signal was calculated by subtracting the minimum value from the maximum value over the given range. Subsequently, the peak-peak amplitude of the high pass filtered response signal V_{out} was determined in the same way. Then, the insertion loss at the determined frequency was calculated using the model shown in figure 5–13 and equation (3–13).

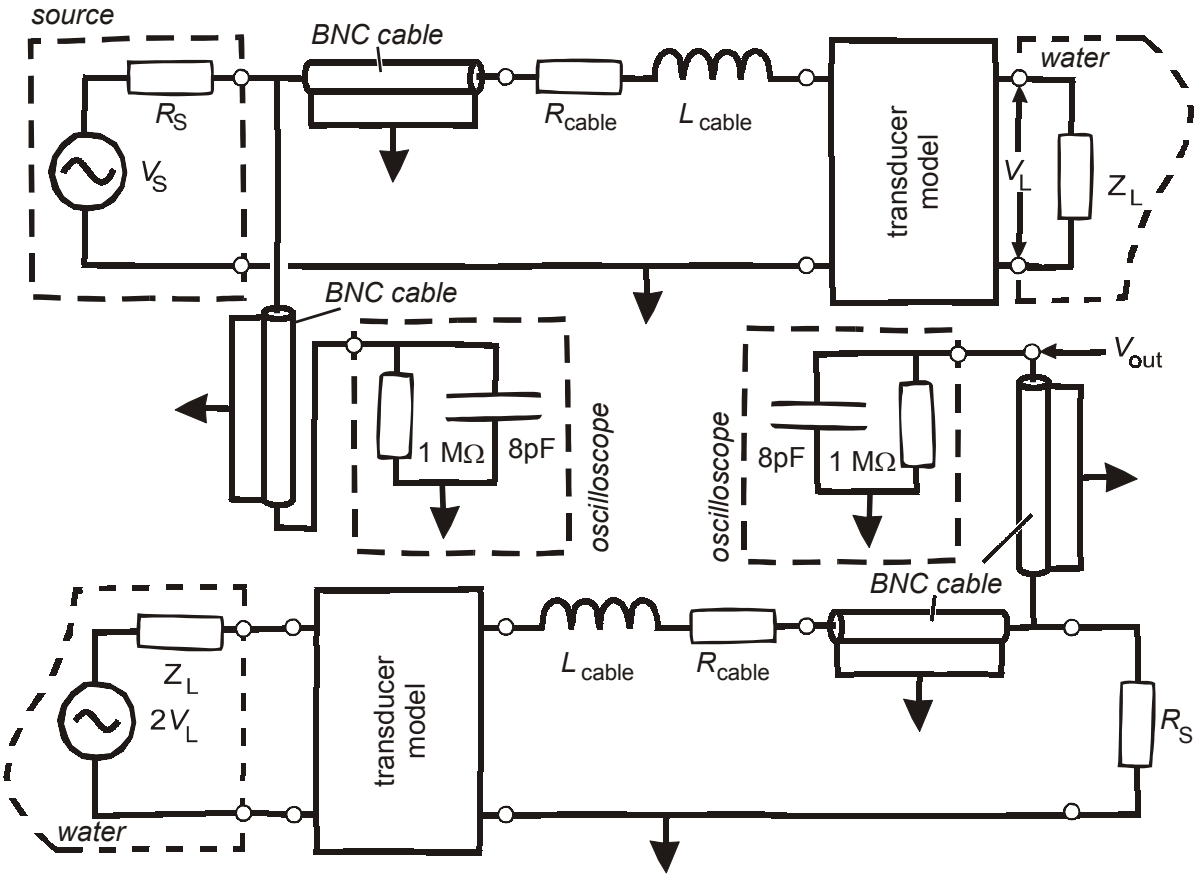

Figure 5–13 Model used for simulating the insertion loss of a single element transducer.

5.3.3 Large single element transducer

Simulations show that 40 cycles is sufficient to calculate the insertion loss of the large multi-element transducer using the pulse train method. The graph in figure 5–14 shows the calculated insertion loss as well as the 11 experimentally obtained insertion loss points. The experimental data points were fitted by a curve. This curve is identical to the simulated insertion loss but shifted downwards 4.9 dB. The additional loss is possibly caused by losses in the Hysol on top of the transducer. Also, the acoustic wave through the water is slightly attenuated, although this is a very minor effect. A more important effect is the alignment of the transducer to the water-air interface. A tiny misalignment will already affect the amplitude of the reflected signal tremendously. All these factors were not taken into account in the simulation. The minimum insertion loss was -24.3 dB at a frequency of 7.8 MHz. The -6 dB bandwidth (BW) was 780 kHz for the both the simulation as the measurement.

The insertion loss for the large single element transducer was already calculated in chapter 2 without the (BNC) cables included in the model. In that case the difference between the simulation and the experimental curve was 5.5 dB. Adding the (BNC) cables to the model improves the simulation data by 0.6 dB.

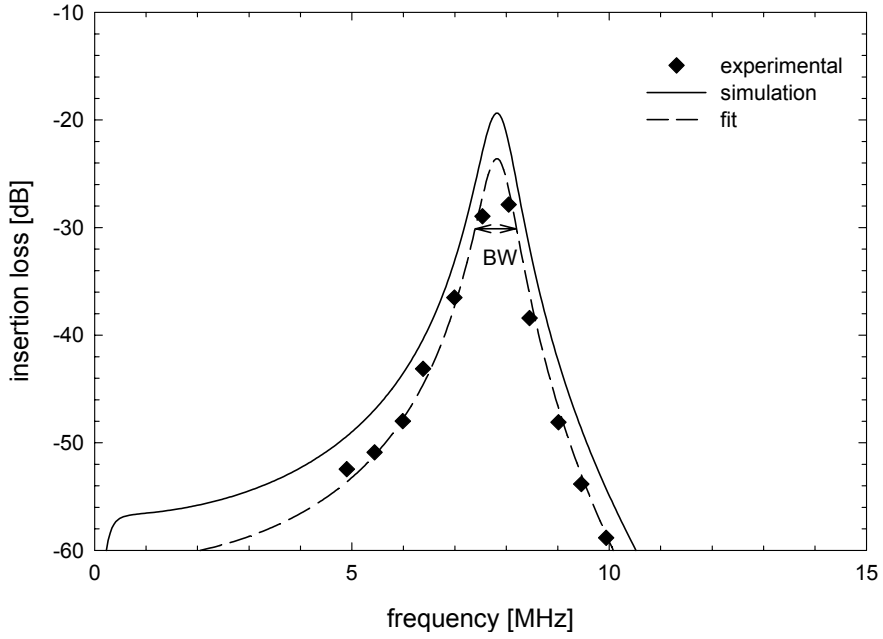

Figure 5–14 Simulated (——) and measured (◆) insertion loss of the large single element transducer. The dashed line is the fitted curve (— —) through the experimental data by shifting the simulated curve 4.9 dB downwards.

5.3.4 Small single element transducer

The number of cycles of the pulse train for the small transducer was set to 20. The insertion loss of the small single element transducer is presented in figure 5–15. The simulated curve is shifted 2.19 dB downwards to fit the experimental points. Emphasis of the fitting lays on the 6.5 MHz and 7 MHz points.

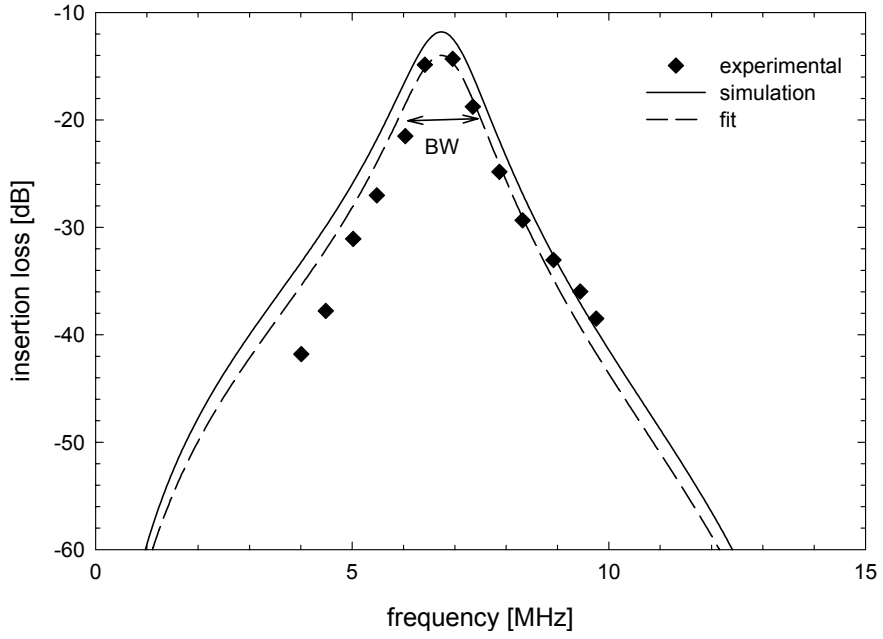

Figure 5–15 Simulated (——) and measured (◆) insertion loss of the small single element transducer. The dashed line is the fitted curve (— —) through the experimental data by shifting the simulated curve 2.19 dB downwards.

The minimum insertion loss is -14.0 dB at a frequency of 6.7 MHz. The calculated -6 dB bandwidth is 1.3 MHz, whereas the bandwidth for the experimental data is estimated at 1.6 MHz.

5.3.5 Large multi-element transducer

The experimental setup for the next experiment is shown in figure 4–11. The transducer that emits the ultrasonic wave is the large single element transducer and the receiving transducer is the large multi-element transducer. Two different insertion losses were measured:

- the four elements of the multi-element transducer were connected to each other through which one large transducer is created and thus one signal was recorded (parallel);
- the four elements were connected to the oscilloscope input in pairs of two and four separate signals were recorded (series).

In the first case, the simulated and measured insertion loss can be found in figure 5–16. The experimentally obtained minimum insertion loss is -35.4 dB, which is 9.1 dB less then the simulated insertion loss of -26.3 dB. The -6 dB bandwidth (BW) of both curves is 1.2 MHz.

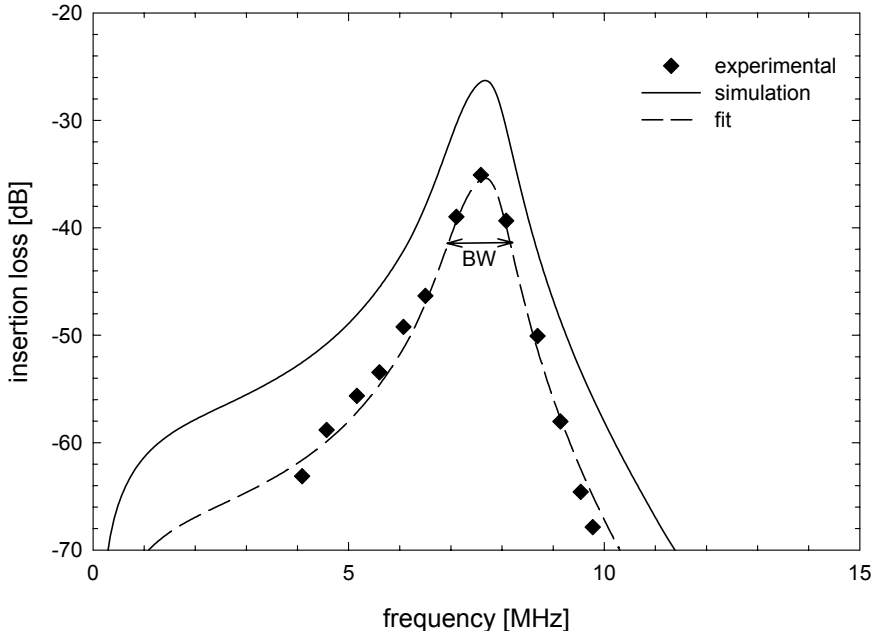

Figure 5–16 Simulated (——) and measured (◆) insertion loss of the large multi-element transducer with the large single element transducer as emitter and the elements of the receiving large multi-element transducer all connected to the same 50 Ω load. The dashed line is the fitted curve (— —) through the experimental data by shifting the simulated curve 9.10 dB downwards.

In the second case, the peak-peak amplitudes of the four elements are determined and these values are added to obtain the insertion loss. This was done because the signals of the various elements are not in phase and the peak-peak amplitude of the summed signals would be less than the sum of the peak-peak signals. The insertion loss of the multi-element transducer is presented in figure 5–17. The APLAC simulation predicts a minimum insertion loss of -20.1 dB, whereas the measured insertion loss is -25.5 dB; a difference of 5.4 dB. The simulated curve is shifted 5.34 dB downwards to fit the experimental data. The -6 dB bandwidth is 1.45 MHz and 1.3 MHz for the simulated and measured curves, respectively. The bandwidth is similar for both cases: 1.2 MHz versus 1.3 MHz. The insertion loss however is almost 10 dB less if the elements are individually connected to a 50 Ω load. Thus the multi-element transducer improves the insertion loss and the bandwidth remains constant.

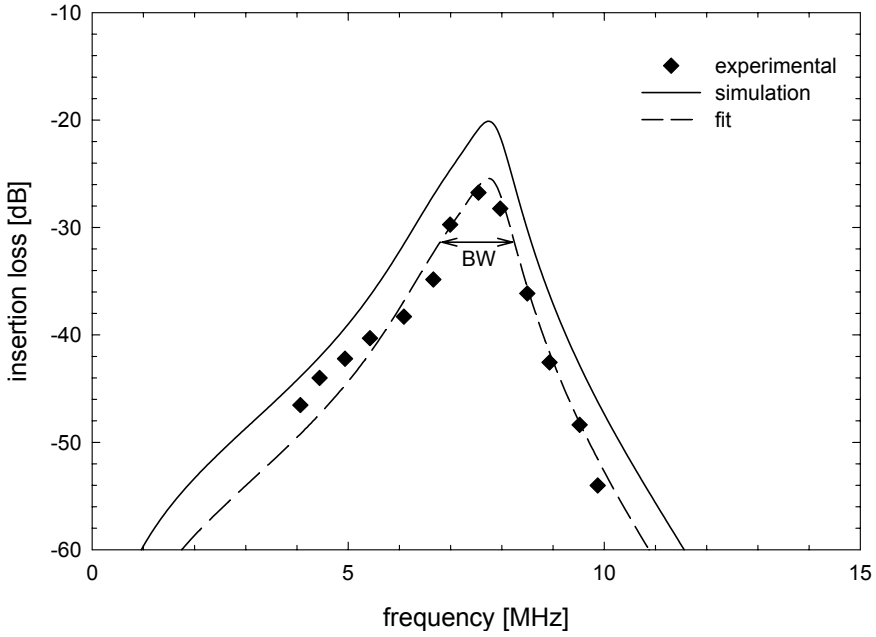

Figure 5–17 Simulated (——) and measured (◆) insertion loss of the large multi-element transducer with the large single element transducer as emitter and the elements of the receiving large multi-element transducer each connected to a 50 Ω load. The dashed line is the fitted curve (— —) through the experimental data by shifting the simulated curve 5.34 dB downwards.

5.3.6 Small multi-element transducer

The insertion loss of the small multi-element transducer was measured similar to the large multi-element transducer: with all the elements connected to each other (parallel) and the elements connected separately (series) to a 50 Ω load. The insertion loss is plotted in figure 5–18 for the elements connected in parallel. The measured minimum insertion loss is -15.4 dB. The -6 dB bandwidth is 2 MHz. If the elements are connected in series the minimum insertion loss de-

creases to -6.7 dB and the bandwidth increases to 2.3 MHz. The simulated and measured insertion loss for series connection are shown in figure 5–19. The simulated insertion loss matches well to the experimentally obtained insertion loss for the parallel as well as the series connection.

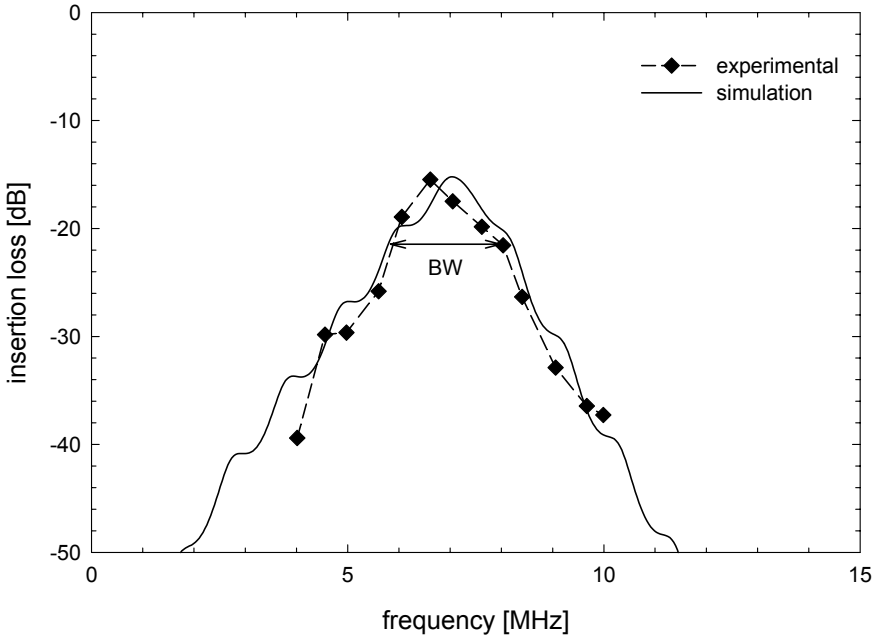

Figure 5–18 Simulated (——) and measured (◆) insertion loss of the small multi-element transducer with the small single element transducer as emitter and the elements of the receiving small multi-element transducer connected in parallel.

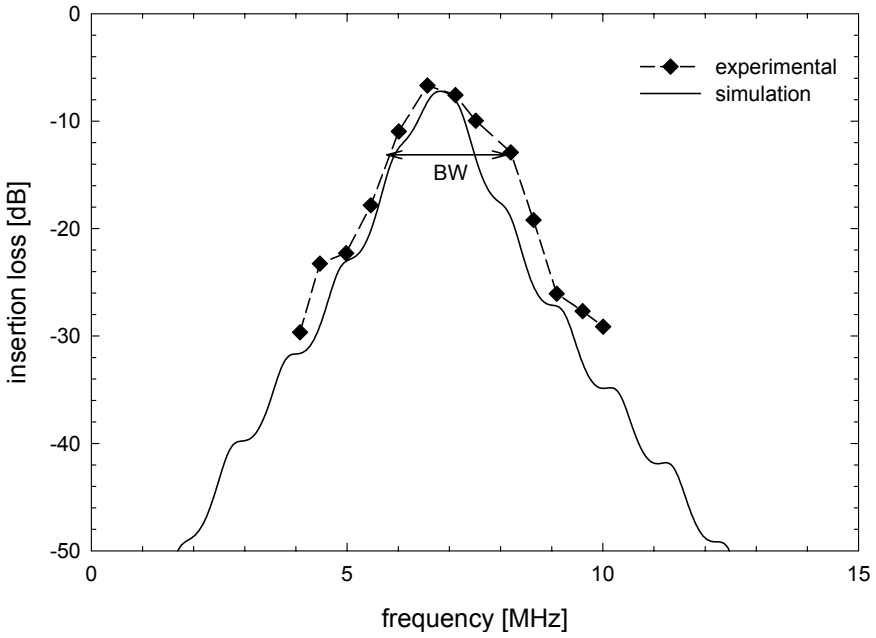

Figure 5–19 Simulated (——) and measured (◆) insertion loss of the small multi-element transducer with the small single element transducer as emitter and the elements of the receiving small multi-element transducer connected in series.

5.4 Pulse-echo experiments

5.4.1 Large single element transducer

Figure 5–20 shows an average of 256 pulse-echo signals of the large single element transducer from a water-air interface at approximately 10 mm. The signal was high pass filtered for the same reasons as the insertion loss signals, before it was compared to the theoretically predicted signal.

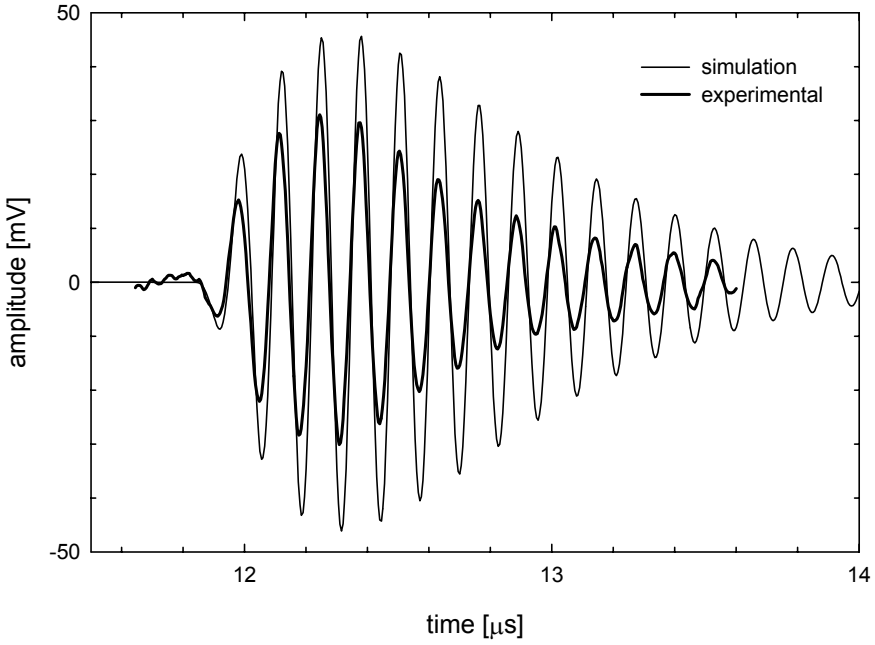

Figure 5–20 Measured and simulated pulse-echo response insertion loss of the large multi-element transducer.

The applied pulse was a 7.35 MHz single cycle sine with an amplitude of 7.5 V. The simulated pulse-echo has a peak-peak amplitude of 92 mV and the measured pulse-echo a peak-peak amplitude of 61 mV. This corresponds to a loss of 3.6 dB which is less than the 4.9 dB as found in the insertion loss curve.

5.4.2 Small single element transducer

Delay time versus distance measurements were performed for this transducer. First, the reflection from a water-air interface was measured while varying the distance from 10 mm to 1 mm between the transducer and the interface. Second, the reflection of the spinal cord phantom was measured where 100 single shot pulse echo responses per distance for distances from 10 mm to 2 mm were taken and averaged. In both cases, a single shot pulse of 6.8 MHz with an amplitude of 15.2 V was used. The recorded signals were sampled with 500 MSa/s and 8192 samples were taken per recording.

The initial distance between the transducer and the water-air interface was 10 mm. To decrease the distance between the transducer and the water-air interface 0.25 mm, 415 nl water was removed, see equation (4–3).

Figure 5–21 shows the transducer response for a distance between the transducer and the water-air interface of 1 mm (upper) and 10 mm (lower). The echo from the smallest distance can be observed in the graph, although it coincides with the ringing of the transducer. The echo from the largest distance can be clearly distinguished. To detect the time of arrival of the echo signals a simple threshold filter was applied: if the time is larger than 850 ns and the signal is greater then 25 mV an echo is being detected. The thick dashed line in both graphs indicates the threshold filter.

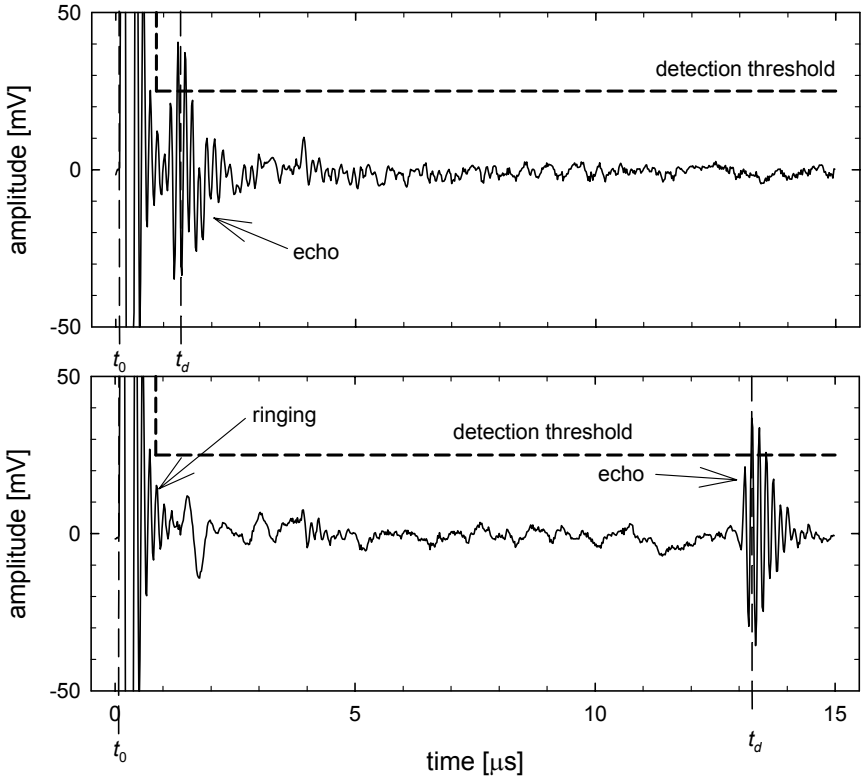

Figure 5–21 Excitation signal (left) and echo signal (right) for the small multi-element transducer with the water-air interface at a distance of 1 mm (upper) and 10 mm (lower).

The delay time of an echo is the interval between the time t_0 the excitation pulse is applied to the transducer and the time of arrival t_{echo} of the echo signal detected by the threshold filter. The delay time t_d can be found by

$$t_d = t_{echo} - t_0 \tag{5-3}$$

Applying this threshold filter to the single shot data results in a delay time versus distance plot as shown in figure 5–22. A linear fit was made through the data points. The coefficient of determination R^2 between the fit and the data was

better than 0.99. The slope of the line can be converted to the sound velocity in water v_{water} according to:

$$v_{water} = \frac{2d}{t_d} \tag{5-4}$$

where t_d/d is the slope of the fitted line. The factor 2 is introduced because d is the distance between the transducer and the interface, whereas the actual distance traveled by the acoustic wave is $2d$. The sound velocity in water v_{water} obtained in this case is 1506 m/s, which matches the value given by Selfridge of 1509 m/s for water at 30 °C.

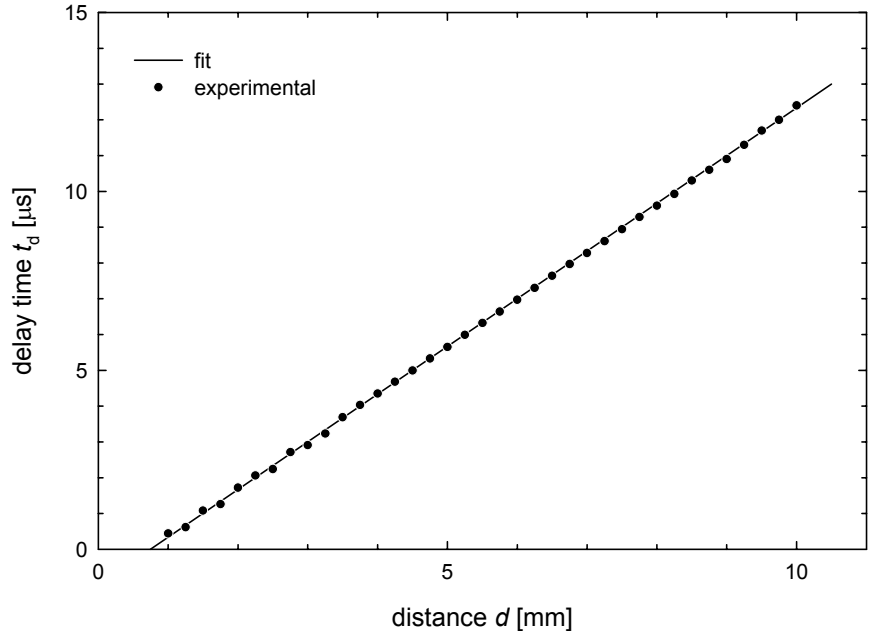

Figure 5–22 Experimentally obtained delay time versus distance (•) for pulse-echo measurements on the small single element transducer with a water-air interface and a fitted curve (——).

For the water-air interface single shot recordings were sufficient to clearly identify an echo signal, whereas the reflection coefficient of the spinal cord phantom is much lower and therefore the echo signals are much smaller. To enable echo detection the 100 recorded signals were averaged after their DC component was removed. Figure 5–23 shows the average of 100 signals if the distance between the transducer and the spinal cord phantom is 2 mm (upper) and 4 mm (lower), respectively. On the left side in both recordings the ringing of the transducer is visible. In the center of each graph a box was drawn in which an "echo" originating from the backing-water interface is observed. The backing has a thickness of approximately 4.5 mm and the sound velocity is 2600 m/s resulting in an "echo" at 3.9 µs. This "echo" can be reduced by applying a more lossy backing, e.g. epoxy filled with metal particles. Also a thinner backing may be used to avoid interference with the echo from the spinal cord phantom. Because only at 4 mm distance the echo signal is clearly distinguishable and definitely beyond the backing

echo, the signals where the distance *d* is less than 4 mm will not be used for further analysis.

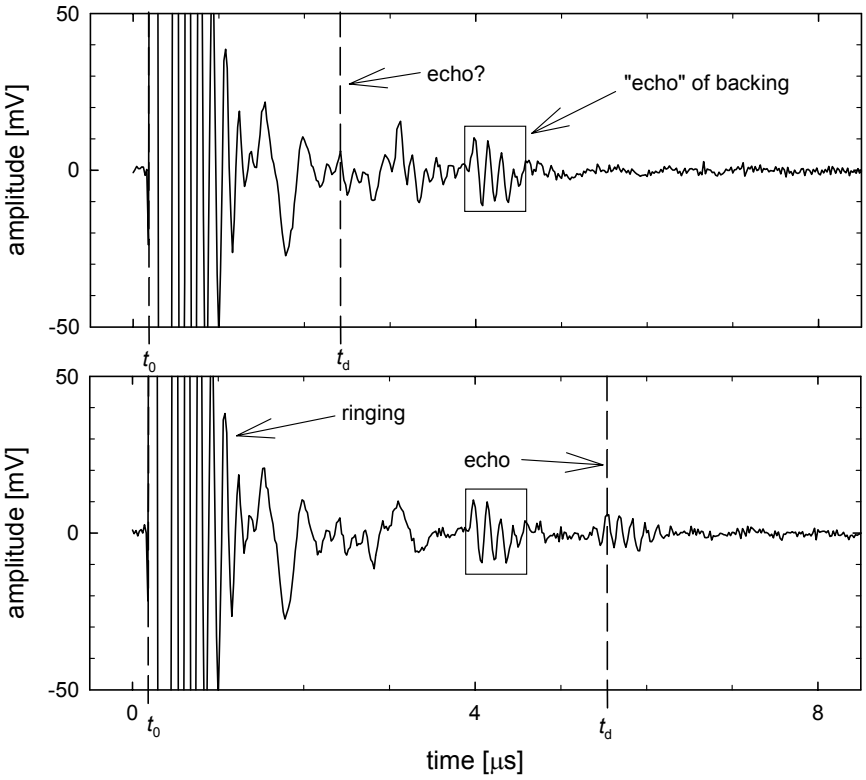

Figure 5–23 Average of 100 echo signals for the small single element transducer and the spinal cord phantom at a distance of 2 mm (upper) and 4 mm (lower).

The time of arrival of the echo t_{echo} was determined by finding the time corresponding to the maximum value of the averaged signals. The delay time t_d is plotted versus the distance *d* between the transducer and the spinal cord phantom in figure 5–24. The data points are fitted using the following linear fit:

$$t_d = \frac{2d}{v_{water}} - 0.16 \times 10^{-6} \tag{5-5}$$

where v_{water} is the sound velocity in water and has a value of 1503 m/s.

Two of the averaged echo signals are displayed in figure 5–25. The peak-peak amplitude was calculated by subtracting the minimum value of the echo signal from its maximum values as indicated in the graph. The peak-peak amplitude of the averaged signals is 14 mV and 11 mV for a distance of 4 mm and 10 mm, respectively. The peak-peak amplitude for the water-air interface is almost 75 mV. This means that the reflection coefficient of the water-spinal cord phantom interface is approximately 15 %, which is in agreement with the theoretical value of 12 % (see subsection 4.3.5 on page 80).

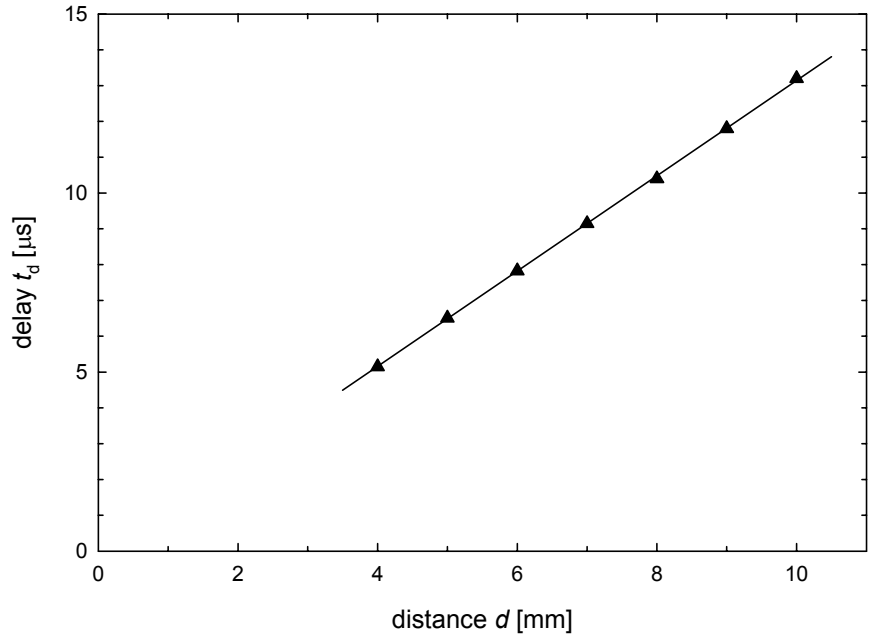

Figure 5–24 *Delay time t_d versus the distance d (▲) between the single element transducer and the spinal cord phantom obtained from the average of 100 signals and a linear fit (——).*

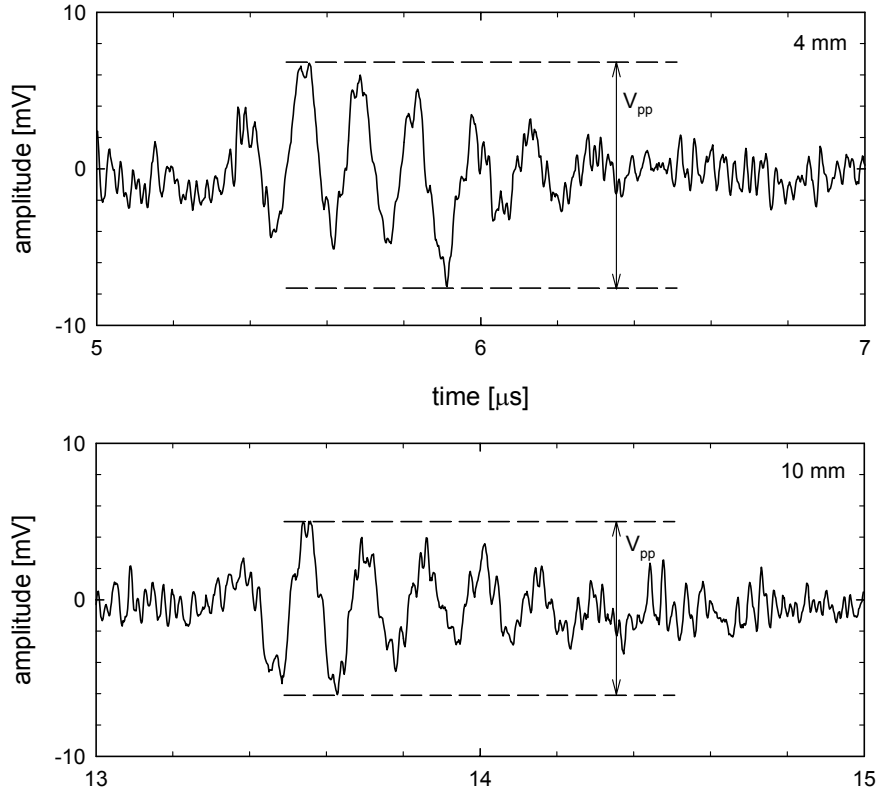

Figure 5–25 *Average of 100 echo signals for the small single element transducer and the spinal cord phantom at a distance of 4 mm (upper) and 10 mm (lower). The sample rate is 500 MSa/s.*

5.5 Signal-to-noise ratio experiments

5.5.1 Small single element transducer with spinal cord phantom

The signal-to-noise ratio (*SNR*) was obtained by using the spinal cord phantom pulse-echo responses from subsection 5.4.2. Hundred single shot pulses were taken at seven distances from 4 mm to 10 mm with a 1 mm interval. The 100 single shot recordings at each distance were averaged to obtain the peak-peak amplitude of the echo, since this is not possible from a single shot measurement due to the small *SNR*. This is illustrated in figure 5–26, where a single shot echo (gray) signal from the spinal cord phantom at a distance of 6 mm is shown together with the average of 100 echo signals (black). The time of arrival of the echo t_{echo} was already determined (see the previous section). The rms noise was obtained by the method presented in subsection 4.4.4 by integrating over the period from 4.8 µs (end of ringing) to t_{echo}-0.3µs (start of echo).

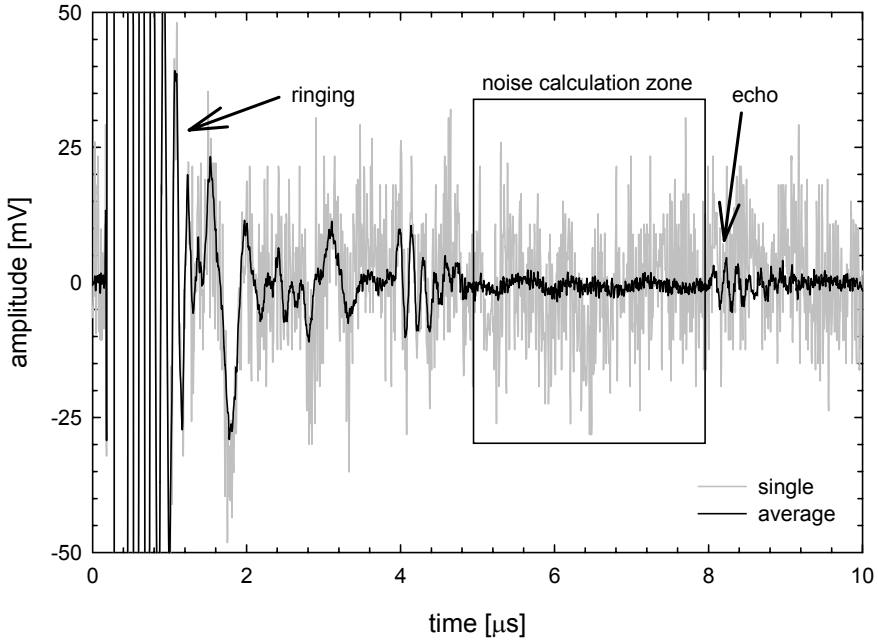

Figure 5–26 Single shot pulse-echo recording (gray) and average of 100 pulse-echo recordings (black) of the small single element transducer with the spinal cord phantom as the reflector at a distance of 6 mm.

The peak-peak amplitude of the averaged echo signal is plotted as a function of the distance *d* between the transducer and the spinal cord phantom in figure 5–27a. The graph shows that there is no correlation between the peak-peak amplitude of the echo signal and the distance *d*. The dashed line corresponds to the average value of 11.1 mV of the presented data points. In figure 5–27b the experimentally obtained rms noise is plotted versus the distance *d*. The data points were calculated by averaging the rms noise for each single shot recording. It is shown that the mean rms noise is constant. The average value, represented by the horizontal dashed line, is 8.8 mV.

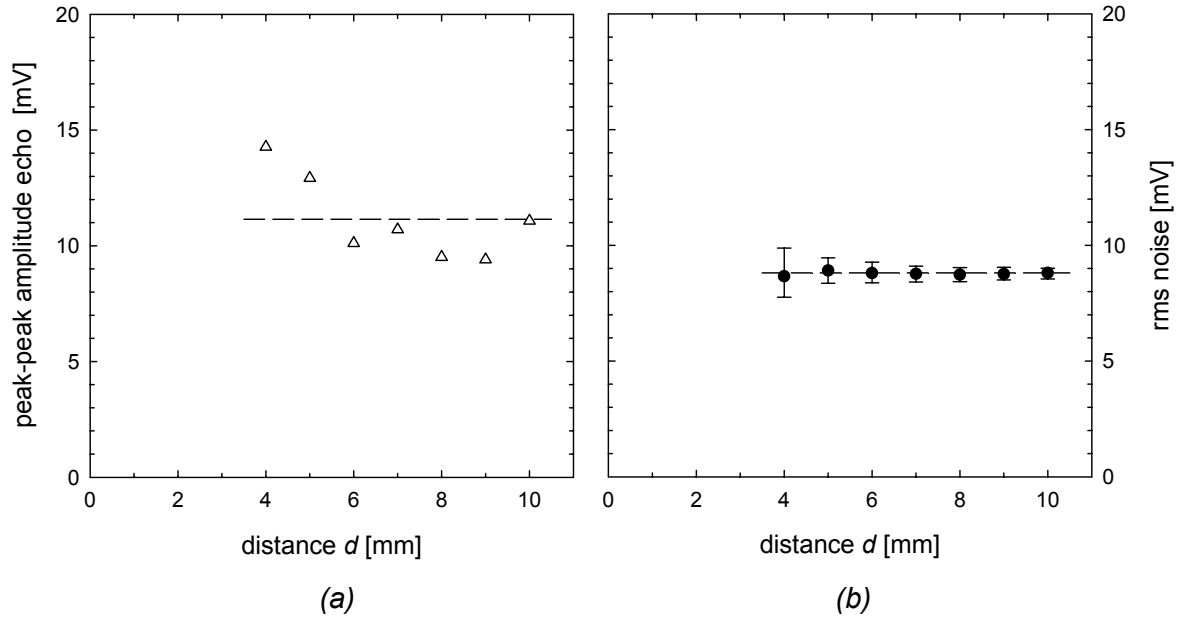

Figure 5–27 *(a) Peak-peak amplitude of the echo signal and (b) the rms noise as a function of the distance d between the transducer and the spinal cord phantom. The dashed lines are the average value of the data points. The error bars in panel b indicate the standard deviation.*

The moving average signal-to-noise ratio SNR_n is plotted versus the number of averaged single shot recordings n in figure 5–28. The distance between the transducer and the spinal cord phantom was 7 mm. If the signals are not averaged (n=1) the *SNR* is 1.9 dB, and is more than doubled for n=2 (4.8 dB). At n=10 the *SNR* is 11.2 dB and increases to 19.2 dB if the 100 signals are averaged. The noise reduction is proportional to the square root of n, which was already shown in equation (3-11). The theoretical line shown in figure 5–28 can be written as:

$$SNR_n = 1.93 + 10\log(n) \tag{5-6}$$

If n is larger than 6 the theoretical line starts to deviate from the measured data. Theoretically, the *SNR* would be 21.9 dB at n=100; the experimentally found value is 2.7 dB lower. A better experimentally determined fit for n>6 is given by:

$$SNR_n = 3.15 + 8.13\log(n) \quad n > 6 \tag{5-7}$$

where the coefficient of determination R^2 is 0.997.

The *SNR* is presented in the chart of figure 5–29 as a function of the distance d. The error bars indicate the standard deviation. The average *SNR* of all distances is 1.95 dB. For comparison the *SNR* was also calculated for the single shot recordings with the water-air interface (see subsection 5.4.2). The average *SNR* for echo from 4.5 mm to 10 mm is 36.3 dB with a standard deviation of 9.4 dB. Note, that the load impedance of the transducer is 50 Ω, which is not ideal for maximum signal transfer. In a separate experiment it was found that the ampli-

tude increases by a factor two if the load impedance is 1 MΩ instead of 50 Ω. This gives an increase in the *SNR* of 6 dB if the noise in the load does not change. The experimentally obtained squared rms noise is $8.1 \cdot 10^{-5}$ V^2. The squared Johnson noise in a 50 Ω and 1 MΩ resistor is $1.2 \cdot 10^{-11}$ V^2 and $2.4 \cdot 10^{-7}$ V^2, respectively. The noise generated by the load can therefore be neglected. Thus, it is concluded that the *SNR* increases by 6 dB if the load impedance of the transducer is changed to 1 MΩ. According to equation (5-6) this corresponds to a four times averaged single shot recording with a transducer load impedance of 50 Ω.

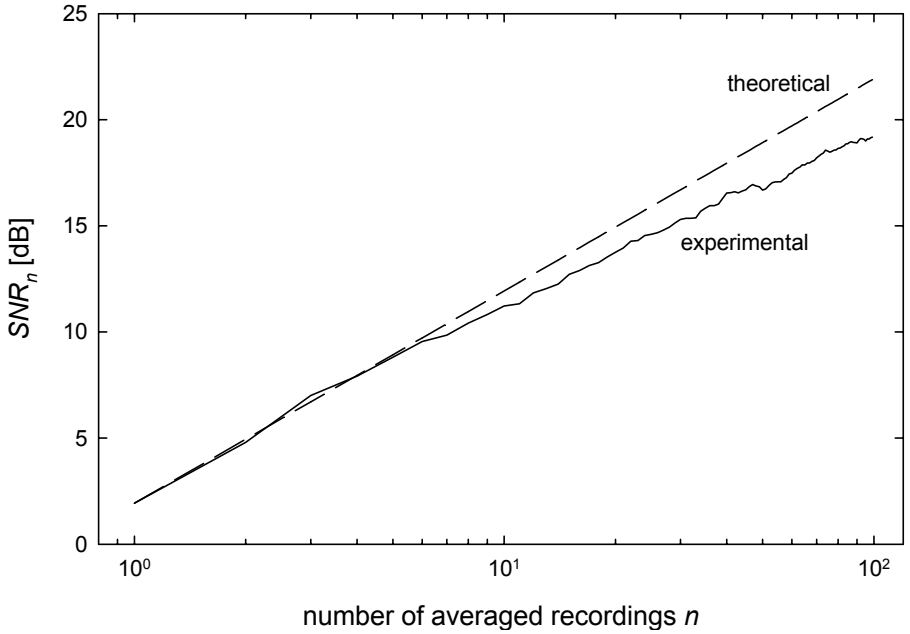

Figure 5–28 Mean signal-to-noise ratio versus the number of averages for the single element transducer with the spinal cord phantom at a distance of 7 mm.

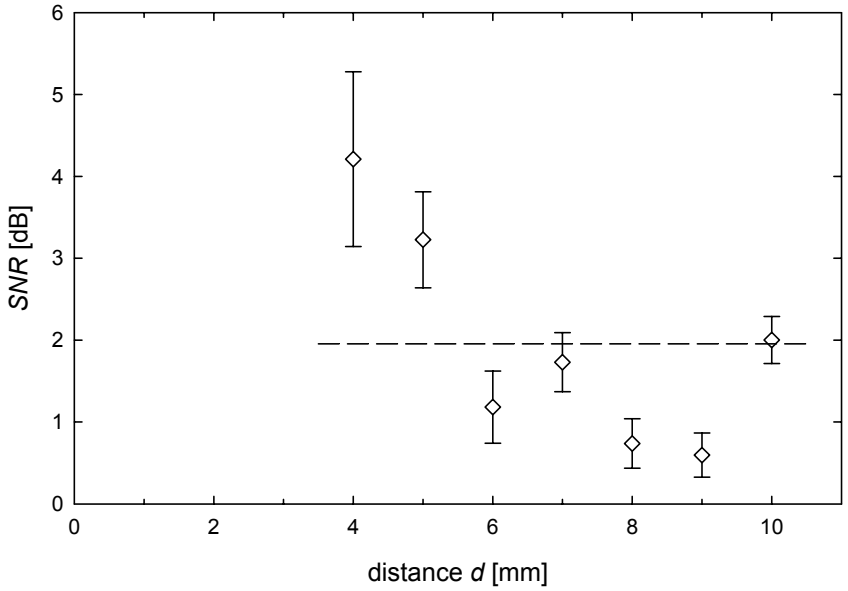

Figure 5–29 Average signal-to-noise ratio as a function of the distance d between the single element transducer and the spinal cord phantom. The error bars indicate the standard deviation and the dashed line the average value (1.95 dB).

5.5.2 Multi-element versus single element transducer

The setup shown in figure 4–11 was used to obtain pulse-echo recordings for the signal-to-noise calculations of the multi-element transducers. First, the methods and results of the large multi-element transducer (4 elements) will be discussed extensively; hereafter the results of the small multi-element transducer (16 elements) will be discussed.

The large single element transducer was used as the emitter and placed approximately 1 cm from the large multi-element transducer used as the receiver. The elements of the receiver were:

- each connected to a 1 MΩ load (in series) or
- all connected to each other and to a 1 MΩ load (in parallel).

In case of series connection the following procedure was followed to calculate the *SNR*:

- 100 single shot recordings per element (total 4 elements) were recorded;
- the DC component of all 400 recordings was removed;
- the recordings of the 4 elements were added;
- the peak-peak amplitude of the added signal was obtained;
- the rms noise of the added signal is calculated over the interval from 2.04 µs to 5.15 µs;
- the previous two steps are repeated 100 times, giving 100 *SNR* values.

Then the same procedure was followed to obtain data for the transducer with the elements connected in parallel, also resulting in 100 *SNR* values. The mean of these two series are displayed in the bar chart of figure 5–30. The *SNR* of the elements connected in series is 38.0 dB, whereas the *SNR* decreases by 6.9 dB to 31.1 dB for the elements connected in parallel. The error bars indicate the standard deviation and have values of 11.6 dB and 8.9 dB for the series and parallel connection, respectively. The theoretical *SNR* increase is approximately 2 dB (see subsection 3.3.2). Thus the experiments show a larger increase than the theory predicts.

The performance of the large multi-element transducer regarding the *SNR* could be better if the echoes received by the different elements would be in phase. To illustrate the phase difference the recorded echo signals of the four elements are displayed in figure 5–31. The vertical thick line can be used as a reference to identify the phase difference between the signals. The peak-peak amplitudes of the signals are: 33 mV, 21 mV 28 mV and 38 mV. The sum of these values is 120 mV. In the lower graph the summation of the four signals is shown. The peak-peak amplitude of this signal is 74 mV, which is about half of the sum of the peak-peak amplitudes of all the elements. Therefore it may be concluded that, if the echoes would be in phase, the *SNR* would increase from 38.0 dB to 42.2 dB. This situation is comparable to the simulations where the signals are in phase. However, the theoretically expected value for the *SNR* is approximately

120 dB (see figure 3–20), which is 78 dB more than the measured value. It is therefore concluded that the noise in the transducer signal is not only Johnson noise.

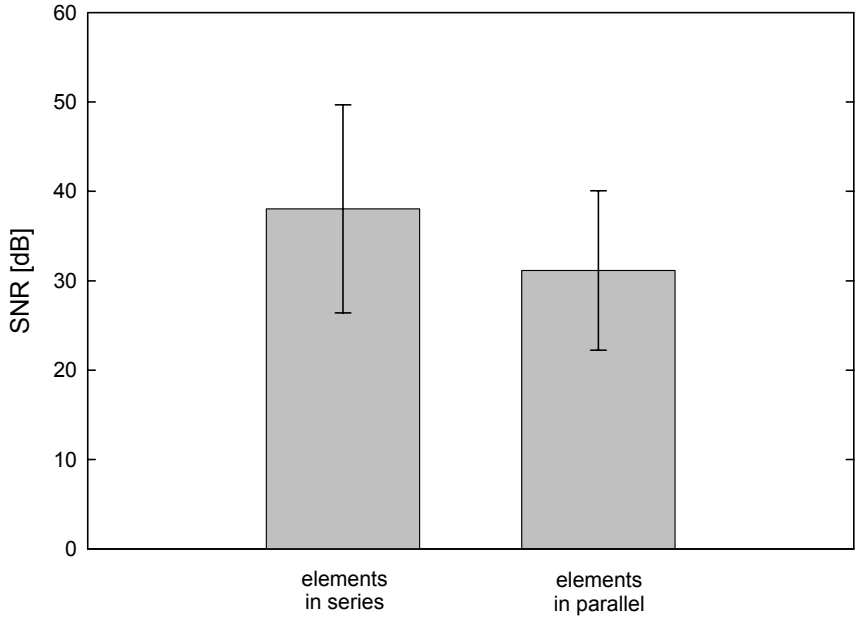

Figure 5–30 Average signal-to-noise ratio of the large multi-element transducer obtained from 100 single pulse-echo recordings using the setup shown figure 4–11: (left) the elements connected in series and (right) the elements connected in parallel. The error bars indicate the standard deviation.

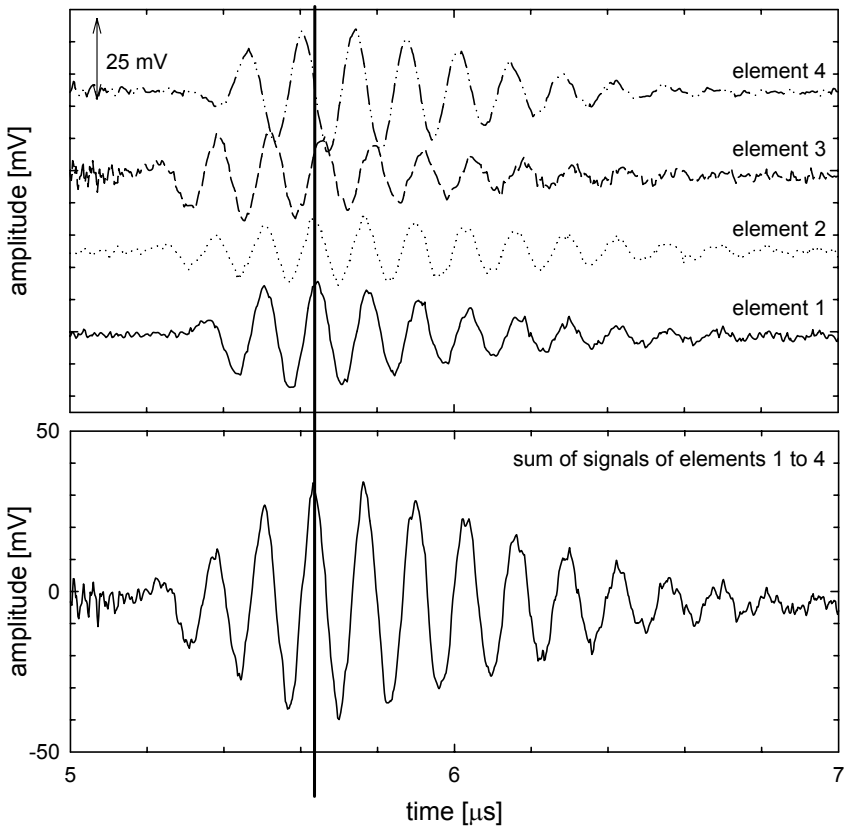

Figure 5–31 (upper) The four echo signals of the individual elements of the large multi-element transducer and (lower) the summation of the four echo signals.

Experiments on the small multi-element transducer were carried out, similar to those on the large multi-element transducer. The differences will be stated below. As the emitter the small single element transducer was used. The distance between the emitter and the receiver was approximately 2 cm. Per element 20 instead of 100 single shot recordings were made. The rms noise was calculated over the period from 2 µs to 12 µs. The results of the *SNR* calculations are shown in figure 5–32. The average *SNR* is 47.2 dB and 45.2 dB for the elements connected in series and in parallel, respectively. This is a difference of 2 dB, which corresponds well to the theoretical value in subsection 3.3.2. The calculated standard deviations for the elements connected in series and in parallel are 8.6 dB and 8.0 dB, respectively.

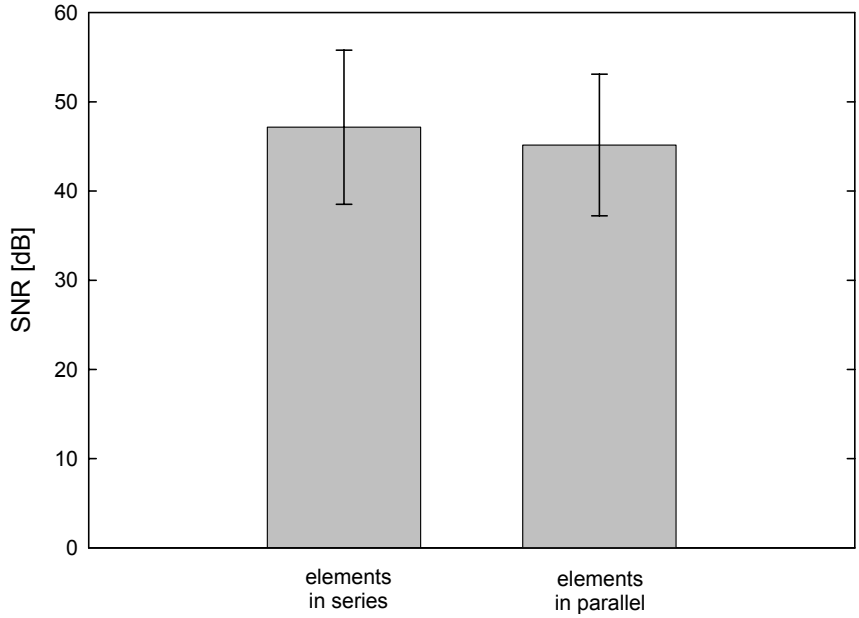

Figure 5–32 Average signal-to-noise ratio of the small multi-element transducer obtained from 20 single pulse-echo recordings using the setup shown figure 4–11: (left) the elements connected in series and (right) the elements connected in parallel. The error bars indicate the standard deviation.

In conclusion, the *SNR* of the signal of the small transducer is 2 dB and will increase by 2 dB if a multi-element transducer is used instead of a single one. The *SNR* of an echo-signal from the spinal cord phantom as measured in subsection 5.4.2 will increase 6 dB if a load impedance of 1 MΩ instead of 50 Ω is used; the *SNR* will thus increase by 8 dB and will have an *SNR* of approximately 10 dB. Although the peak-peak amplitude of the echo increases in that case, according to equation (5-7), the *SNR* of such a signal is comparable to the average of seven single shot recordings with a transducer load impedance of 50 Ω. In figure 5–33 the average of seven signals is shown together with the average of 100 signals (for reference). The graph shows that it is still difficult to detect the echo signal, which has an *SNR* of 9.9 dB, in a simple way.

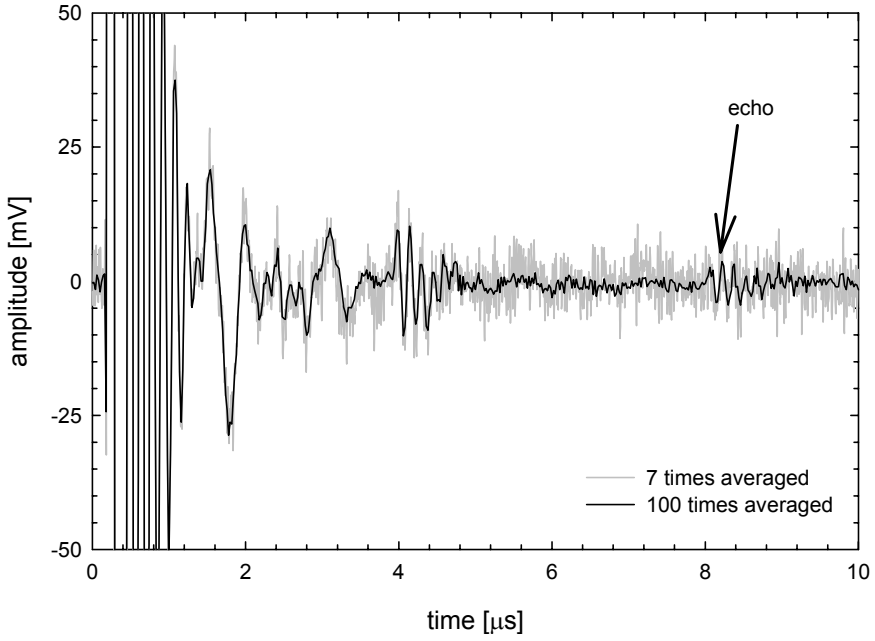

Figure 5–33 The average of seven (gray) and 100 (black) echo signals from the spinal cord phantom at a distance of 6 mm measured with the small single element transducer.

5.6 Conclusions

The transducer impedance can be modeled accurately by the proposed modified KLM model. An additional model for the wires that are connected to the transducer was added to the model. This wire model consisted of a series resistor and inductance; a load capacitance had to be added to the model for small (1 mm^2) transducer elements. The influence of the wires becomes important at frequencies above 8 MHz. The parameter values that were selected to obtain the best possible fit between the experimental data and the simulation data are within a realistic range. The modeled and experimentally obtained transducer impedance are in good agreement.

The predicted insertion loss is for all but the small single element transducer approximately 5 dB less than the measured insertion loss. There are three factors that may cause this difference:

- losses in the Hysol on top of the transducer. A Hysol layer of 0.1 mm will cause a loss of 0.6 dB;
- attenuation of the ultrasonic wave in the water, which is a minor effect. An ultrasonic wave of 10 MHz will be attenuated 0.04 dB while traveling over 2 cm of water;
- misalignment of the transducer to the water-air interface. A tiny misalignment affects the amplitude of the reflected signal tremendously.

The model predicts the shape of the insertion loss well, but the simulated insertion loss is less than the empirical value.

The measured insertion loss and bandwidth for the tested transducers are summarized in table 5–5. The insertion loss for both multi-element transducers increases almost 10 dB compared to a single element transducer of equal size. The bandwidth increases slightly in favor of the multi-element transducers.

Table 5–5 Measured insertion loss (IL_{min}), bandwidth (BW) and signal-to-noise ratio (SNR) transducer for the tested transducer.

transducer type	***IL*$_{min}$ [dB]**	**BW [MHz]**	***SNR* [dB]**
large single element	-24.3	0.78	-
small single element	-14.0	1.6	36.3*
large multi-element			
parallel	-35.4	1.2	31.1**
series	-25.5	1.3	38.0**
small multi-element			
parallel	-15.4	2.0	45.2**
series	-6.7	2.3	47.2**

* reflection from an water-air interface, with emitter and receiver as the same element and a load impedance of 50 Ω

** single element was used as the emitter and the multi-element transducer as the receiver with a load impedance of 1 MΩ.

The shapes of the measured and simulated pulse-echo response for the large single element transducer match. The amplitude of the measured signal is smaller than the simulated amplitude, but the difference corresponds to the difference in the insertion loss.

Ringing of the transducer must be reduced to enable detection of the spinal cord at distances below 4 mm. The axial resolution of the transducer is sufficient for this application. The size of the transducer is within the maximum dimensions allowed.

The *SNR* is increased by 6.9 dB for the large multi-element transducer when the elements are connected in series instead of in parallel. However, the standard deviation of the calculated values is 9 dB, which makes the increase non-significant. The results for the small multi-element transducer are similar, but the increase in the *SNR* when the elements are connected in series instead of in parallel (2 dB) is less than for the large multi-element transducer. Also, in this case the standard deviation is substantial.

Even under optimal conditions the *SNR* of a multi-element transducer is not sufficient to detect the echo signal. Therefore, a signal processing method to reliably detect the echoes is needed and will be presented in the next chapter.

References

[1] A.R. Selfridge, "Approximate Material properties in Isotropic Materials," *IEEE transactions on sonics and ultrasonics*, vol. SU-32, no. 3, pp. 381-394, 1985.

Chapter 6

Signal processing and its realization

6.1 Introduction

The system requirements for distance detection for a spinal cord stimulation (SCS) system were already stated in chapter 1. The two requirements concerning the signal processing part are: measuring distance between 3 mm and 6.5 mm with an accuracy of 0.5 mm and a low power consumption. The latter will be discussed in subsection 6.1.1.

As shown in the previous chapter, the single shot echo signal from the spinal cord phantom is very small and has a poor *SNR* (≈2 dB). The *SNR* of this signal can be increased to 10 dB by using a multi-element transducer and a 1 MΩ load instead of a 50 Ω load. Another method to increase the *SNR* is by averaging. It was calculated that for detection of the echo signal the average of 100 single shot signals is needed. However, this would increase the power consumption considerably. A single shot signal is preferred, but the *SNR* of 10 dB is not sufficient to identify the echo accurately. Therefore, an alternative signal processing method for reliable detection of the reflected signal is proposed.

A block diagram of the complete ultrasonic distance detection system for SCS is shown in figure 6–1. The pulse generator drives the piezoelectric transducer. The transducer signal is passed through a signal processor to reliably detect at which moment an echo is present in the transducer signal. The signal processor sends a signal to the spinal cord stimulator, which determines the corresponding stimulation level. The stimulator may consist of a (voltage controlled) current source or a DA converter [1]. After a short time (seconds, minutes; clock 1), a new cycle to determine the delay of the echo signal has to be started. The spinal cord stimulator applies pulses with a frequency generally ranging from 50 pulses

per second (pps) to 100 pps (clock 2) to the spinal cord. Note that clock 1 does not indicate the actuation frequency of the transducer, but the frequency of the distance measurements.

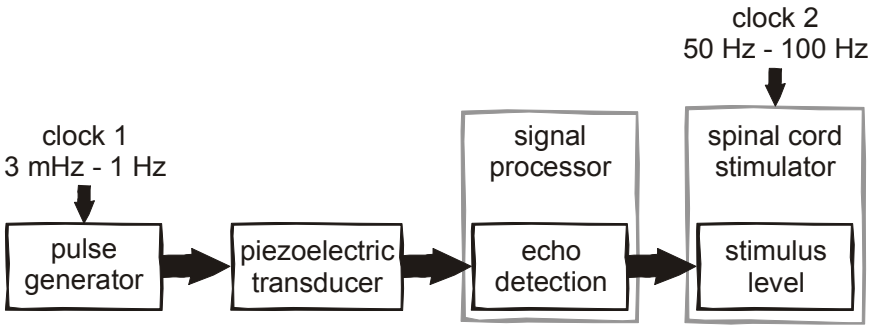

Figure 6–1 Block diagram of the system for the spinal cord echo detection system.

6.1.1 Power consumption

For long term use the power consumption of the distance detection system must be low with respect to the power consumption of the used SCS system. The specifications of the ITRELL II (Medtronic) are listed in table 6–1. The stimulation current (40 µA rms) is based on pulses with a duration of 0.2 ms, an amplitude of 4 mA and a rate of 50 pps. Under these favorable conditions the battery lifetime *BLT* will be:

$$BLT = \frac{\text{battery capacity}}{\text{rms current}} = \frac{2.7\ \text{Ah}}{(40+7)\,\mu\text{A}} \approx 58\,000\ \text{hours} \approx 6\tfrac{1}{2}\ \text{years} \qquad (6\text{–}1)$$

The stimulation can be considerably higher for high pulse rates (80 pps – 100 pps) and high stimulation voltages (7 V – 10.5 V), thus reducing battery lifetime by 50 % or more.

Table 6–1 Specifications of the ITRELL II (Medtronic).

parameter	value	unit
bias current	7	[µA]
stimulation current	40	[µA rms]
output amplitude	0 – 10.5	[V]
battery capacity	2.7	[Ah]
battery voltage	3.7	[V]

The battery lifetime will also be reduced if the distance detection system is implemented. The rms current needed to drive the transducer will be the main component. The current consumed by any additional electronics for driving the transducer and detecting the echo signal is omitted in this calculation.

The transducer is stimulated by a single sine voltage pulse with a peak-peak amplitude of 8 V, which gives a current with an almost identical shape with an amplitude i_{pp}. The rms current through the transducer can be calculated from:

$$i_{rms} = \tfrac{1}{2} i_{pp} \sqrt{\frac{T_s}{2T}} \qquad (6\text{–}2)$$

where T_s is the period of the stimulation current, and T the interval between successive excitation pulses. As an example a 4 mm × 4 mm PXE-5 transducer with a thickness of 0.3 mm was used to measure the current consumption. The peak-peak current through the transducer is 550 mA. The frequency of the pulse was 6.9 MHz. For an interval of 60 seconds between two excitation pulses, the rms current is 9.6 µA. Assuming that the current consumption of ITRELL II is approximately 50 µA, the current consumption of this transducer will reduce the battery lifetime by approximately 20 percent.

To keep the power consumption lower the driving signal may be chosen lower. Because this reduces the *SNR* of the echo signal, an echo detection filter must be realized that is capable of detecting an echo with a poor *SNR*.

6.1.2 Echo signal analysis

The echo signal properties were obtained in chapter 5 and will be repeated here briefly. The peak-peak amplitude of the echo signals is several millivolts (9-15 mV). The *SNR* of the single shot pulse-echo responses is approximately 2 dB. If the multi-element transducer, consisting of 16 elements, is considered with a 1 MΩ load per element the *SNR* increases to approximately 10 dB.

Figure 5–25 shows two typical echo signals obtained from the spinal cord phantom (reflector) at 4 mm and 10 mm distance. These echo signals were sampled at a rate of 500 MSa/s and one hundred were averaged. The shape of the echo signal depends on:

- the position of the transducer and the spinal cord phantom due to the varying impedance between the reflector and the transducer and
- the angle of incidence/reflection of the ultrasonic wave on the spinal cord phantom.

The echo signal spectrum was estimated by calculating the Fourier transform of the averaged echo signals at distances from 4 mm to 10 mm. The procedure to obtain the echo spectrum is:

- the time t_{echo} corresponding to the maximum amplitude of the average of 100 echo signals was obtained;
- 1024 samples were taken from t_{echo}–0.5 µs to t_{echo}+1.546 µs;
- a Hanning window $w_{Hanning}(t)$ was applied to this signal:

$$w_{Hanning}(t) = \tfrac{1}{2}\left(\tfrac{1}{2} - \tfrac{1}{2}\cos\left(\frac{2\pi t}{T_0}\right)\right) \qquad (6\text{–}3)$$

where T_0 is the time window;

- a Fast Fourier Transform was applied;
- the four previous steps were carried out for the echo signals from 4 mm to 10 mm distance between transducer and spinal cord phantom. The seven spectra were averaged.

The averaged spectrum is shown in figure 6–2. The spectrum is centered at 6.84 MHz. The bandwidth of the echo is approximately 2 MHz. The spectrum can be seen as a 6.84 MHz signal modulated by a 1 MHz frequency.

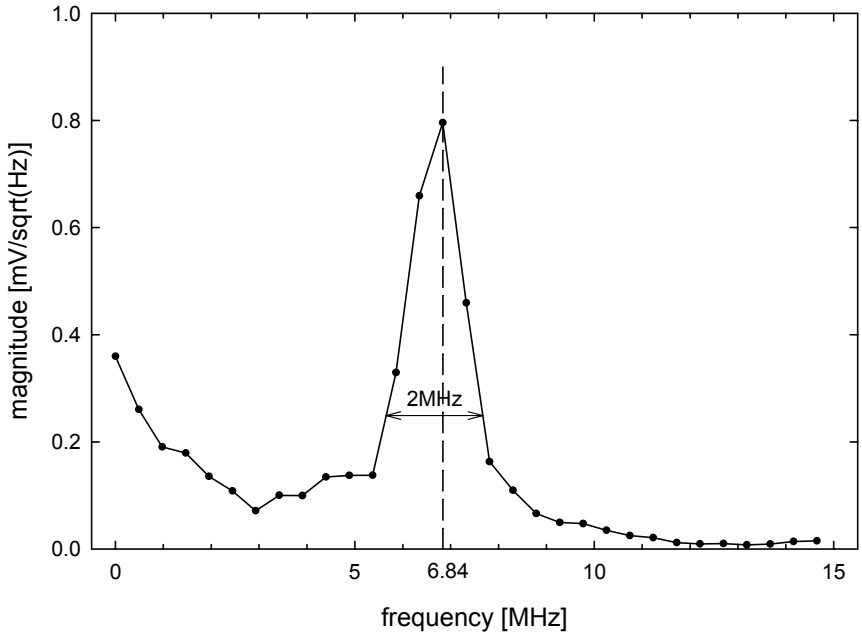

Figure 6–2 Average spectrum of the echo from the spinal cord phantom with the small single element transducer.

6.2 Filters

A commonly used technique to improve the *SNR* is filtering. The selection criteria for a filter are that it is capable of detecting an echo with a poor *SNR* and that the power consumption is low to minimally reduce the battery lifetime. From a range of filters known in literature [2-4] two filters were selected: the matched filter and the amplitude demodulation filter.

The matched filter (subsection 6.2.1) is commonly used to detect echo signals that are buried in noise. Although digital filtering is the simplest way to build a matched filter, it is usually more power consuming than analog techniques. The shape of the echo signal must be known and preferably be identical whatever the circumstances, to realize a reliable matched filter. However, the shape of the echo signal depends on the angle of incidence/reflection on the reflector (spinal cord), the distance between the transducer and the reflector as well as on the shape of the reflector [5].

The echo signal consists of a high frequency part modulated by a lower frequency. Therefore, the amplitude demodulation filter (subsection 6.2.2) is considered for echo detection. This filter can be realized with analog electronics, which is an advantage over digital techniques with respect to its power consumption.

The mathematical background of the matched filter and the amplitude demodulation filter are presented in the following two subsections. The performance of the amplitude demodulation filter is compared to that of a matched filter. Ultimately, threshold or peak detection is required to obtain the time of arrival from the echo signal at the output of both the matched filter and the amplitude demodulation filter.

6.2.1 Matched filter

A matched filter has an impulse response that has the same shape as the expected input signal reversed in time. Therefore, it is called a matched filter; the impulse response is matched to the expected input signal. The optimality criterion for a matched filter is that the *SNR* of the filter output is maximal. The input waveform $x(t)$ consists of a signal $f(t)$ of finite duration and known shape, but of unknown amplitude disturbed by additive noise $n(t)$:

$$x(t) = f(t) + n(t) \tag{6–4}$$

The matched filter design is such that the output of the filter will rise to a large value when the signal arrives, whereas it is relatively small otherwise. The impulse response of a matched filter is $h(t)$, and the input signal is defined in equation (6–4). The resulting output signal $y(t)$ can be written as:

$$y(t) = x(t) \otimes h(t) = f(t) \otimes h(t) + n(t) \otimes h(t) = y_s(t) + y_n(t) \tag{6–5}$$

where $\otimes$ denotes the convolution, and $y_s(t)$ is the component of the output due to the signal and $y_n(t)$ the component due to input noise. The *SNR* of the output signal is defined as:

$$SNR = \frac{y_s(t)}{\sqrt{E\left\{|y_n(t)|^2\right\}}} \tag{6–6}$$

The variance of the output noise can be written as the inverse Fourier transform of the input noise spectrum $P_{nn}(\omega)$ and the transfer function $H(\omega)$:

$$E\left\{|y_n(t)|^2\right\} = \frac{1}{2\pi}\int_{-\infty}^{+\infty} P_{nn}(\omega)|H(\omega)|^2 d\omega \tag{6–7}$$

The signal component of the output signal of the filter can be denoted as:

$$y_s(t) = \frac{1}{2\pi}\int_{-\infty}^{+\infty} F(\omega)H(\omega)e^{j\omega t} d\omega \tag{6–8}$$

The squared *SNR* can be calculated by substituting equations (6–7) and (6–8) into equation (6–6), resulting in:

$$SNR^2 = \frac{\left|\frac{1}{2\pi}\int_{-\infty}^{+\infty} F(\omega)H(\omega)e^{j\omega t}d\omega\right|^2}{\frac{1}{2\pi}\int_{-\infty}^{+\infty} P_{nn}(\omega)\left|H(\omega)\right|^2 d\omega} \tag{6–9}$$

Define two functions, $G_1(\omega)$ and $G_2(\omega)$, which product is the integrand of the numerator of the previous equation and where one of the functions is the root of the denominator:

$$G_1(\omega) = \sqrt{P_{nn}(\omega)}\left|H(\omega)\right| \tag{6–10}$$

and

$$G_2(\omega) = \frac{F(\omega)}{\sqrt{P_{nn}(\omega)}}e^{j\omega t} \tag{6–11}$$

Substituting equations (6–10) and (6–11) into equation (6–9) followed by applying Schwarz's inequality (see appendix A.3) gives:

$$\begin{aligned} SNR^2 &= \frac{1}{2\pi}\frac{\left|\int_{-\infty}^{+\infty} G_1(\omega)G_2(\omega)d\omega\right|^2}{\int_{-\infty}^{+\infty}\left(G_1(\omega)\right)^2 d\omega} \\ &\le \frac{1}{2\pi}\frac{\int_{-\infty}^{+\infty}\left(G_1(\omega)\right)^2 d\omega\int_{-\infty}^{+\infty}\left(G_2(\omega)\right)^2 d\omega}{\int_{-\infty}^{+\infty}\left(G_1(\omega)\right)^2 d\omega} = \frac{1}{2\pi}\int_{-\infty}^{+\infty}\left(G_2(\omega)\right)^2 d\omega \end{aligned} \tag{6–12}$$

Substituting $G_2(\omega)$ gives the maximum squared *SNR*:

$$(SNR^2)_{max} = \frac{1}{2\pi}\int_{-\infty}^{+\infty}\frac{\left|F(\omega)\right|^2}{P_{nn}(\omega)}d\omega \tag{6–13}$$

The *SNR* attains its maximum value when $G_1(\omega)$ is proportional to $G_2(\omega)$ (see appendix A.3):

$$G_1(\omega) = aG_2^{\,*}(\omega) \Leftrightarrow H(\omega)\sqrt{P_{nn}(\omega)} = a\frac{F^*(\omega)e^{-j\omega t}}{\sqrt{P_{nn}(\omega)}} \tag{6–14}$$

In the special case of white noise:

$$P_{nn}(\omega) = A \tag{6–15}$$

where A is a constant, the transfer function $H(\omega)$ becomes:

$$H(\omega) = \frac{a}{A}F^*(\omega)e^{-j\omega t} \tag{6–16}$$

Thus the impulse response $h(t)$ can be obtained by taking the inverse Fourier transform of equation (6–16), because $F^*(\omega) \leftrightarrow f^*(-t)$:

$$h(t) = \frac{a}{A} f(\tau - t) \tag{6–17}$$

which shows that the time response of the filter is the time-reversed version of the input signal. The expected signal and the filter impulse response are illustrated in figure 6–3.

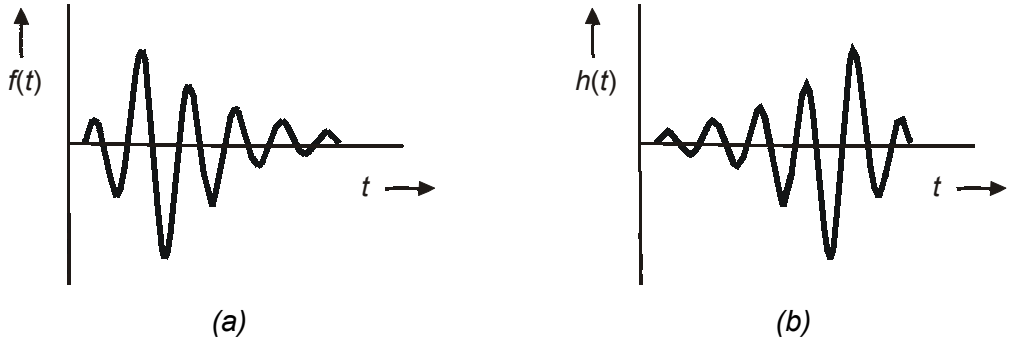

Figure 6–3 (*a*) *expected input signal, and* (*b*) *matched filter time response.*

The maximum *SNR* can be obtained by combining equations (6–13) and (6–15), and applying Parseval's Theorem (see appendix A.2) which yields:

$$SNR_{\max} = \sqrt{\frac{S_{ff}}{A}} \tag{6–18}$$

where S_{ff} is the energy of the signal $f(t)$.

The use of a matched filter gives an optimum performance in the presence of coherent interference as well as random noise. The realization of a matched filter is obtained from the transfer function $H(\omega)$ of equation (6–16) and taking $a=A$ for simplicity, this results in:

$$Y(\omega) = X(\omega)H(\omega) = X(\omega)F^*(\omega)e^{-j\omega\tau} \tag{6–19}$$

where $Y(\omega)$ is the output of the matched filter, $X(\omega)$ is the input signal, and $F^*(\omega)$ is the complex conjugated of the expected signal. The previous equation is similar to the cross-correlation (in the time domain). Figure 6–4 shows a block diagram of a cross-correlator or a matched filter. The low pass filter (*LPF*) is not a perfect integrator. The cross-correlation $R(\tau)$ will therefore be a good approximation. The delay time corresponds to the maximum value of the cross-correlation $R(\tau)$. Therefore, a peak detector is included in figure 6–4.

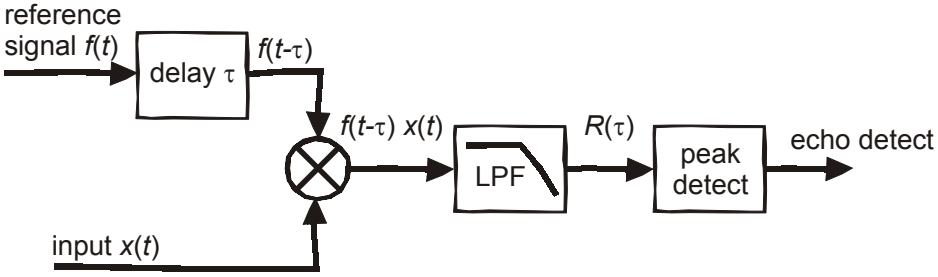

Figure 6–4 Realization of a matched filter including peak detection.

6.2.2 Amplitude demodulation

Amplitude demodulation can be used when a transducer signal consists of a low frequency signal $f_L(t)$ (the modulating signal) and a high frequency signal $f_H(t)$ (the carrier frequency). The transducer signal $x(t)$ with additive noise $n(t)$ can be written as:

$$x(t) = f_L(t) \cdot f_H(t) + n(t) \tag{6–20}$$

The carrier signal with an angular frequency ω_H is modulated by the signal of interest $f_L(t)$. The total signal is disturbed by noise $n(t)$. The signal of interest $f_L(t)$ can be written as:

$$f_L(t) = \begin{cases} A_L \sin(\omega_L t) & t_1 \le t \le t_2 \\ 0 & \text{elsewhere} \end{cases} \tag{6–21}$$

where ω_L is the angular frequency in rad/s. The carrier signal $f_H(t)$ is:

$$f_H(t) = A_H \cos(\omega_H t) \tag{6–22}$$

where ω_H is the angular frequency in rad/s, and $\omega_L \ll \omega_H$.

Amplitude demodulation can be used to obtain the signal $f_L(t)$ from the signal $x(t)$ generated by the transducer. A schematic diagram of an amplitude demodulation filter is shown in figure 6–5. Figure 6–6 shows the demodulation process schematically.

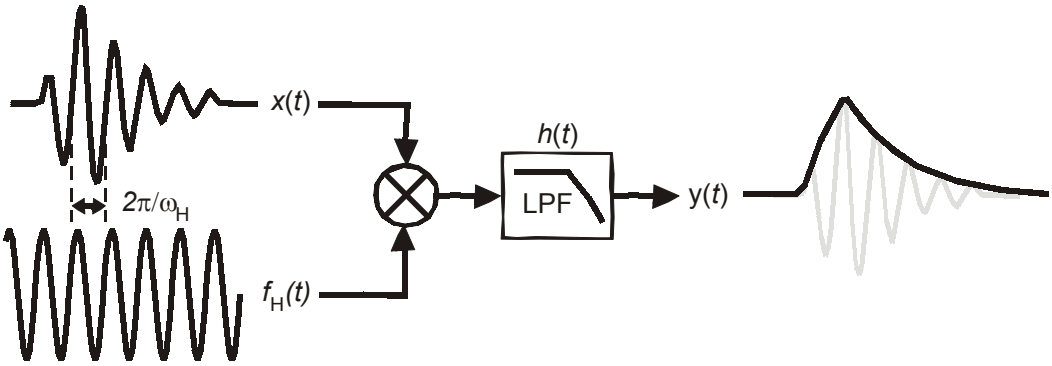

Figure 6–5 Schematic diagram of the amplitude demodulation method.

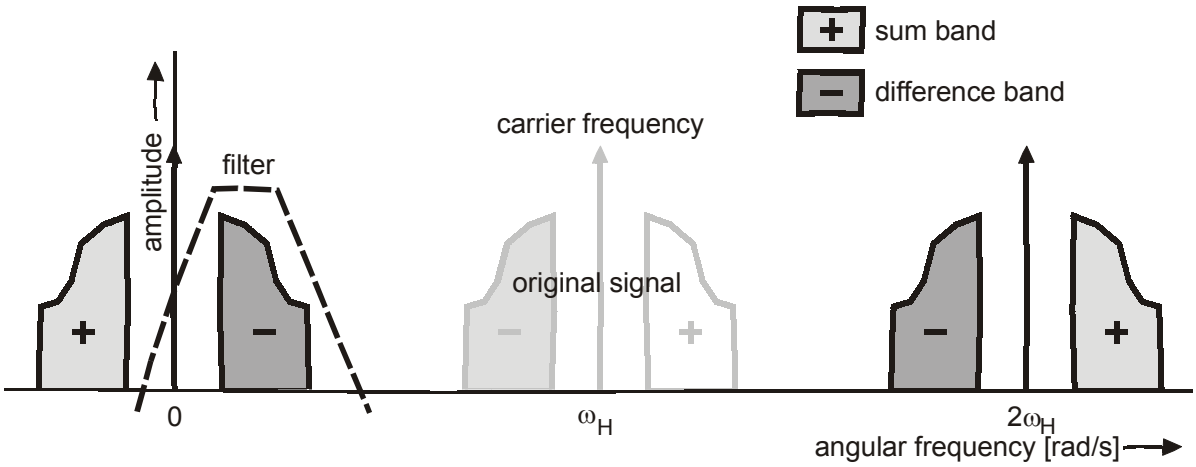

Figure 6–6 Schematic representation of the amplitude demodulation method.

The transducer signal is multiplied by a carrier signal with an angular frequency ω_H. The product is then low pass filtered. The product of $x(t)$ and $f_H(t)$ can be written as (the noise is omitted):

$$x(t) \cdot f_H(t) = \{A_L \sin(\omega_L t) A_H \cos(\omega_H t)\} A_H \cos(\omega_H t) \tag{6–23}$$

The previous equation can be rewritten into the following[3]:

$$x(t) \cdot f_H(t) = \tfrac{1}{4} A_L A_H^2 \left(2\sin(\omega_L t) + \sin((2\omega_L - \omega_H)t) + \sin((2\omega_L + \omega_H)t)\right) \tag{6–24}$$

Because the signal of interest has a lower frequency than the carrier frequency the signal of interest can be obtained by low pass filtering (*LPF*) the output of the multiplier, giving:

$$LPF\{x(t) \cdot f_H(t)\} = \tfrac{1}{2} A_L A_H^2 \sin(\omega_L t) \tag{6–25}$$

6.3 Amplitude demodulation filter versus matched filter

6.3.1 Introduction

The theoretical performance of the amplitude demodulation filter and the matched filter were compared. Both detection methods were implemented in APLAC. For both detection methods, the input signals were pre-filtered by an identical method in step 1. Then the filter was applied in step 2 and the maximum of the filter output was detected in step 3. The index *i* in the subscripts of the time and frequency symbols is used to denote the discrete character.

The time window $w(t_i)$, as shown in figure 6–7, in which an echo can be expected is from 5 µs to 14.5 µs, which corresponds to distances from 4 mm to 10 mm. The echo signal $x_1(t_i)$ was passed through the time window $w(t_i)$:

$$w(t_i) = \frac{1}{1 + 10^3\left(2 - \left[\tanh\left(10^7 t_i - 45\right) + \tanh\left(150 - 10^7 t_i\right)\right]\right)} \tag{6–26}$$

The time window output $x_2(t_i)$ can be written as:

$$x_2(t_i) = x_1(t_i) w(t_i) \tag{6–27}$$

Then the signal was filtered by either the amplitude demodulation (*AM*) filter or the matched filter (*MF*):

$$x_3(t_i) = AM\left[x_2(t_i)\right] \tag{6–28}$$

or

$$x_3(t_i) = MF\left[x_2(t_i)\right] \tag{6–29}$$

---

[3] $\sin(\omega_1)\cos(\omega_2) = \tfrac{1}{2}\{\sin(\omega_1 + \omega_2) + \sin(\omega_1 - \omega_2)\}$

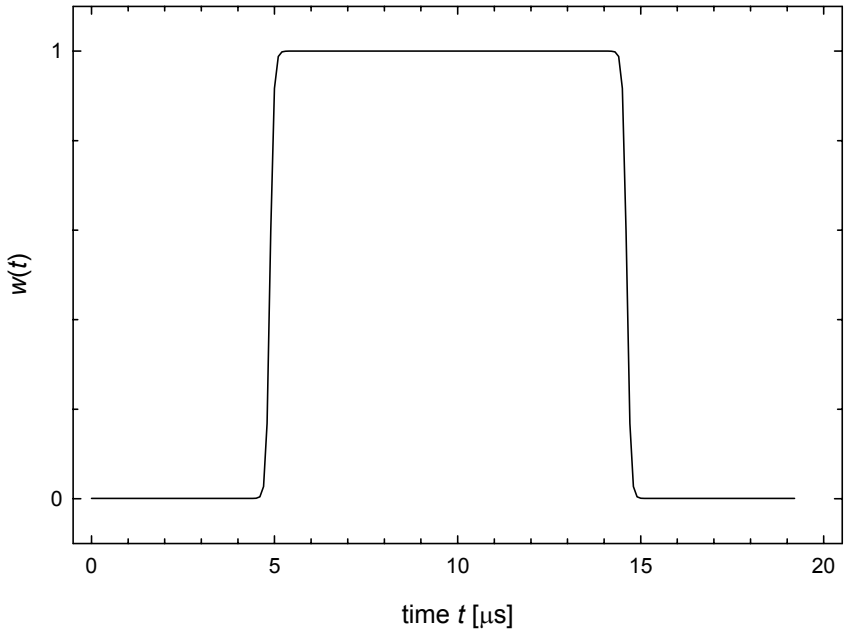

Figure 6–7 The time window w(t).

The amplitude demodulation was carried out by a 6.84 MHz carrier signal after which the signal was low pass filtered by an ideal low pass filter with a cut-off frequency f_0 of 1 MHz.

$$x_3(t_i) = FFT^{-1}\{FFT\{x_2(t_i)\sin(2\pi f_H t_i)\}H_{\text{LPF}}(f_i)\} \tag{6–30}$$

where $H_{\text{LPF}}(f_i)$ is the transfer function of the low pass filter defined by:

$$H_{LPF}(f_i) = \begin{cases} e^{-j2\pi f_i k} & |f_i| \le f_0 \\ 0 & |f_i| > f_0 \end{cases} \tag{6–31}$$

where k is a time constant defining the delay of the filter; in this case k=0.

The matched filtering is performed in a similar fashion. First, the impulse response of the filter must be defined. The impulse response is determined by the signal to be detected, i.e. the echo signal. Therefore, a 100 times averaged echo signal from the spinal cord phantom at 10 mm from the small single element transducer was taken. This signal was low pass filtered (f_0=15 MHz). The part of the signal that is used to define the matched filter's impulse response is shown in figure 6–8. Then, the *FFT* was taken from the impulse response yielding the transfer function $H_{\text{MF}}(f_i)$ of the matched filter. The input signal $x_2(t_i)$ is also fast Fourier transformed, $X_2(f_i)$, and multiplied by $H_{\text{MF}}(f_i)$. Subsequently, the inverse *FFT* was taken to obtain the signal in the time domain. Summarizing:

$$x_3(t_i) = FFT^{-1}\{X_2(f_i)H_{\text{MF}}(f_i)\} \tag{6–32}$$

Finally, the time t_{echo} corresponding to the maximum value of $x_3(t_i)$ for both filters is determined by applying a peak detection system.

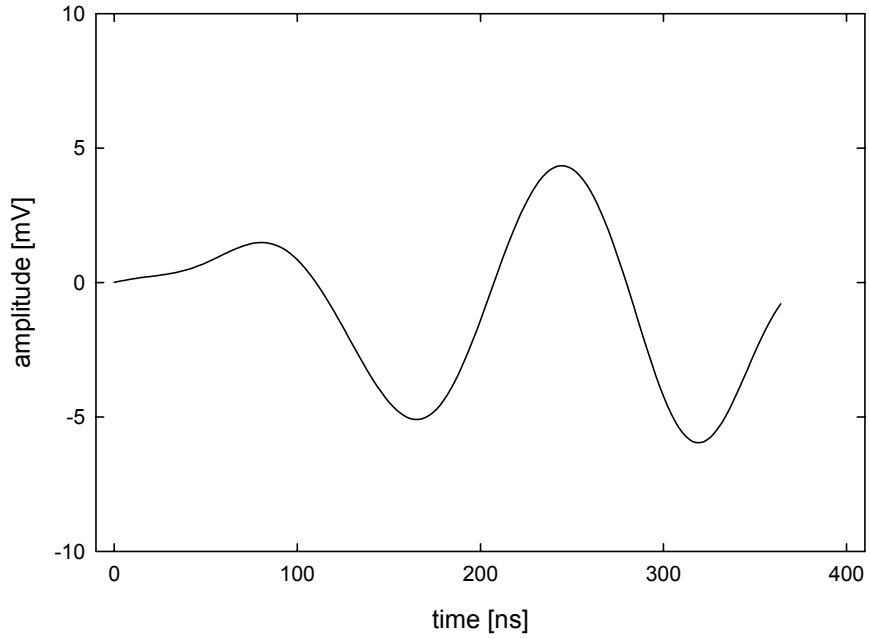

Figure 6–8 Reference signal for correlation with the echo signal or the time inverse of the impulse response of the matched filter.

6.3.2 Filtering the echo signals in APLAC

The recordings as described in chapter 5 were used to test the amplitude demodulation filter and compare its performance to the matched filter. Three sets of signals were used as the filter's input:

- reference signal: average of 100 single shot recordings;
- single shot signal: no averaging;
- optimized signal: average of 7 single shot recordings.

Each set consists of recordings with a distance *d* between the transducer and the spinal cord phantom ranging from 4 mm to 10 mm at intervals of 1 mm.

The reference signal was used to obtain seven reference delay times $t_{d,true}$ to compare to the results of the other sets of signals. The *SNR* of the reference signals is 19.2 dB (standard deviation: 0.7 dB), whereas the single shot recordings have an *SNR* of 1.95 dB (standard deviation: 1.3 dB). The optimized signal has an *SNR* comparable to that of the small multi-element transducer with a 1 MΩ load per transducer element. It was derived from the set of single shot recordings and contains 14 signals per distance having an average *SNR* of 10.2 dB (standard deviation: 1.3 dB).

To determine the performance of the filters a confidence interval of t_{int} = 330 ns (corresponding to a resolution of 0.5 mm) was chosen. The percentage of calculated delay time points within the interval $t_{d,true} \pm t_{int}$ was calculated for each distance. The performance of the filter thus increases with the percentage of points

within the interval. If all the points are within this interval the detection rate is 100 %.

The delay times estimated from filtering are presented in figure 6–9. The upper two graphs show the estimated delay time t_d versus the distance d for the matched filter (▽) on the left and the amplitude demodulation filter (●) on the right. The symbol in the graph represents the delay obtained from the reference signal. The error bars indicate the maximum and minimum calculated delay times t_d for the single shot signals. In the bar chart beneath each plot, the percentage of the single shot estimates within the confidence interval (330 ns) is plotted. The average detection rate of the matched filter is 33 %, which means that 67 % of all the detected delay times is outside the confidence interval. For the amplitude demodulation filter the average detection rate is 57 %. These results are not sufficient for an adequate detection system. Therefore, the filters were also tested with signals with a higher *SNR*, because the filter's performance should increase if the *SNR* of the input signals is increased. Therefore, the optimized signals were used as the input signals. The results are presented in figure 6–10 in the same way as in figure 6–9. The matched filter now has a detection rate of 96 %, whereas the amplitude demodulation filter has a detection rate of 98 %. The overall (in)accuracy of both methods is comparable. If the *SNR* of the input signal is sufficiently high (10 dB), the detection rate reaches almost 100 %.

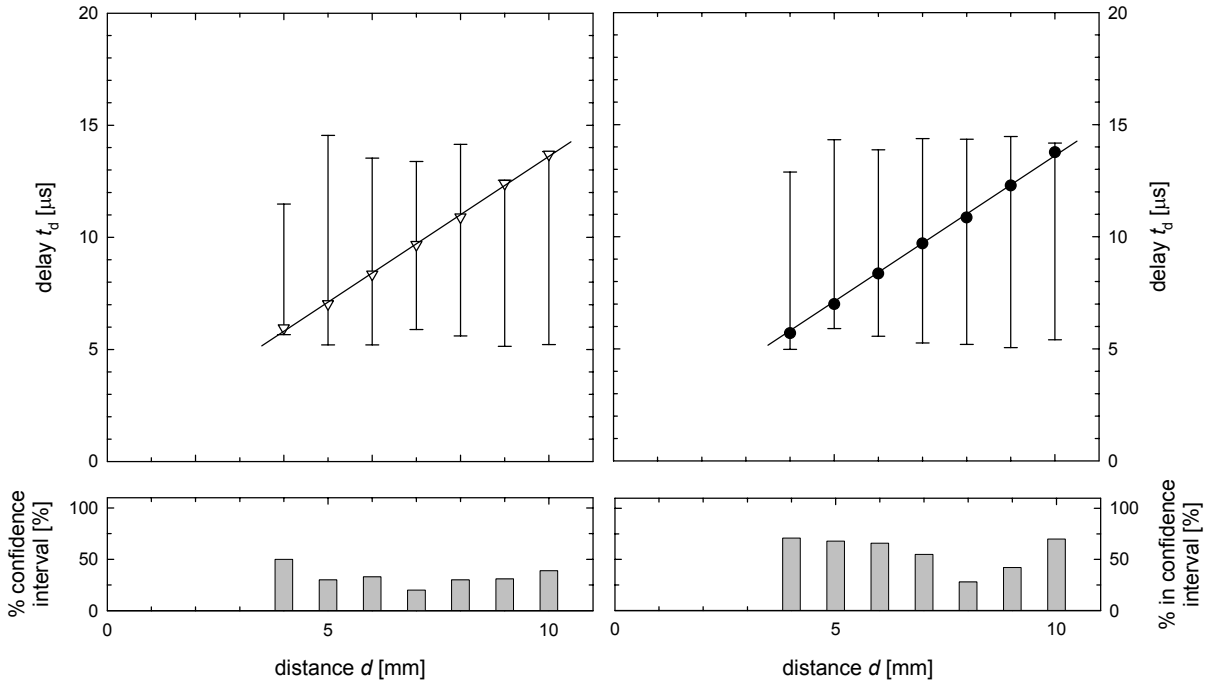

Figure 6–9 Estimated delay time versus the distance for the matched filter (▽) and the amplitude demodulation filter (●) for the single shot recordings. The error bars indicate the maximum and minimum calculated delay times t_d for the single shot signals.

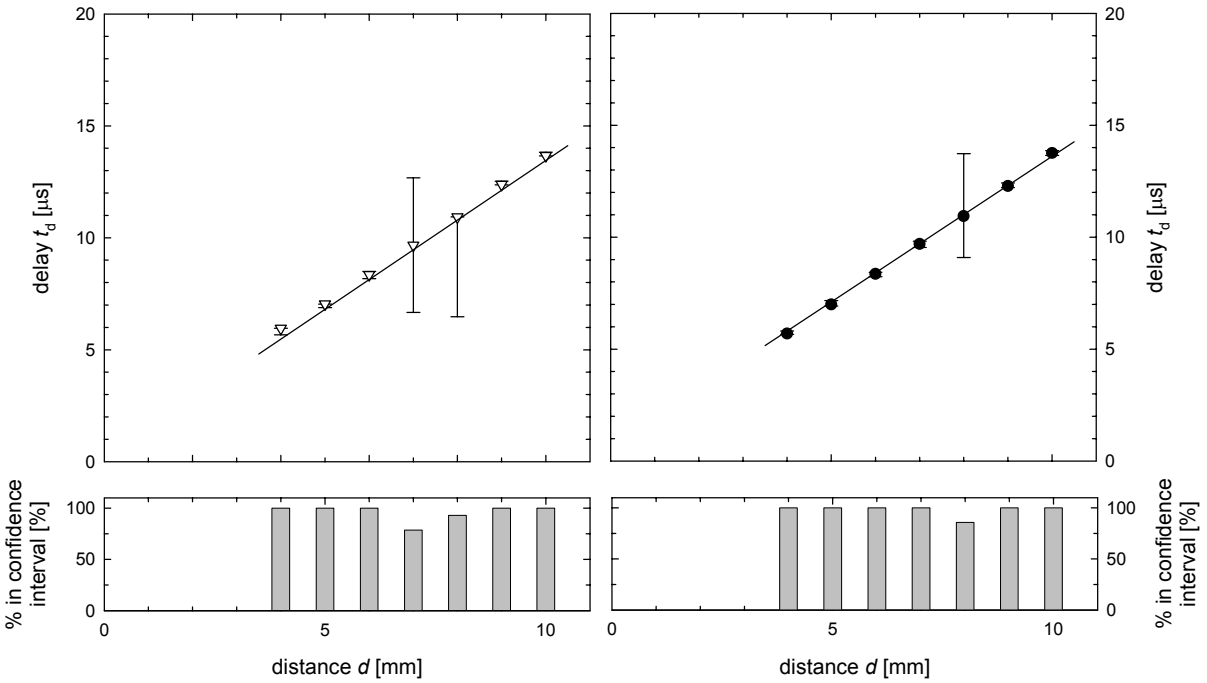

Figure 6–10 Estimated delay time versus the distance for the matched filter (▽) and the amplitude demodulation filter (●) for the optimized signal. The error bars indicate the maximum and minimum calculated delay times t_d for the measurement set.

6.4 Realization of the amplitude demodulation filter

An amplitude demodulation filter has been realized using a low voltage high performance mixer FM IF system (Philips SA636). A schematic diagram of the amplitude demodulation filter is shown in appendix B.

The realized amplitude demodulation filter was compared to an ideal amplitude demodulation filter in APLAC that first multiplies the input signal $x(t_i)$ with the carrier signal $f_H(t_i)$. Subsequently, it is fast Fourier transformed and low pass filtered with the transfer function $H_{LPF}(f_i)$ of equation (6–31) with $k=10^{-9}$ and $f_0=2$ MHz. The output in the time domain $y(t_i)$ is found by taking the inverse Fourier transform. Thus:

$$y(t_i) = FFT^{-1}\{FFT\{x(t_i)f_H(t_i)\}H_{LPF}(f_i)\} \tag{6–33}$$

Figure 6–11 shows the input and normalized output signal of the amplitude demodulation filter. Both the real and the simulated filter output show a peak at the time of arrival of the echo signal.

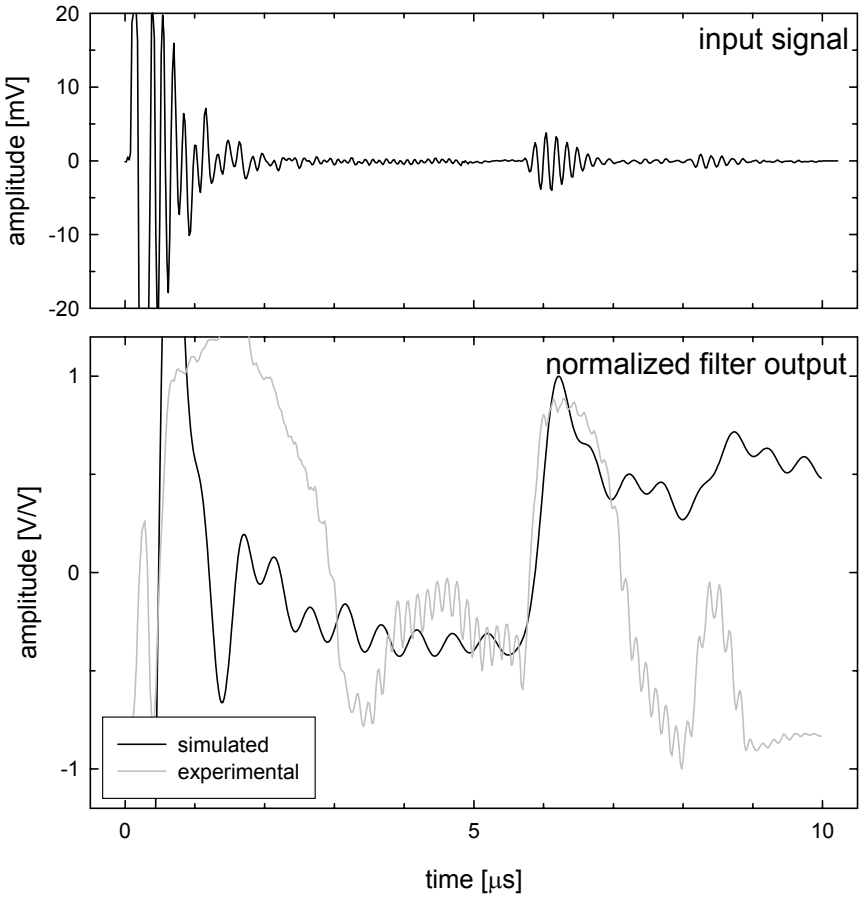

Figure 6–11 The input (top) and normalized output signal (bottom) of the amplitude demodulation filter.

6.5 Conclusions

A filter based on amplitude demodulation was shown to reliably detect echo signals with an *SNR* of 10 dB. The performance of this filter was compared to that of a matched filter, which is commonly used for the detection of echo signals buried in noise. A disadvantage of the matched filter method is that it requires digital signal processing techniques, while the amplitude demodulation method can be performed using the SA636. Digital techniques are usually power consuming especially at high sample rates, and become more inaccurate when the sample rate is decreased.

The detection rate of the amplitude demodulation filter is comparable to that of the matched filter, although the first performs slightly better. Using an input signal with an *SNR* of 10 dB for the amplitude demodulation filter results in a detection rate of 98 %, i.e. the percentage of echoes detected within a confidence interval of 330 ns corresponding to a resolution of 0.5 mm. An analog amplitude demodulation filter has been realized, which performs similar to the simulated filter.

References

[1] W. Starkebaum and M.T. Rise, Ultrasonic Techniques for Neurostimulator Control. Medtronic, Inc. 627,574[5,628,317]. 1997. Minnesota,USA. Ref Type: Patent

[2] D.J. DeFatta, J.G. Lucas, and W.S. Hodgkiss, *Digital Signal Processing: A System Design Approach* New York: Wiley, 1998.

[3] H. Baher, *Analog & Digital Signal Processing* Chichester: Wiley, 1990.

[4] H.J. Blinchikoff and A.I. Zverev, *Filtering in the time and frequency domains* New York: Wiley, 1976.

[5] J.M. Martín Abreu and T.F. Bastos, "Ultrasonic echoes from complex surfaces: an application to object recognition," *Sensors and Actuators A*, vol. 31 pp. 182-187, 1992.

Chapter 7

Conclusions and suggestions for further research

7.1 Conclusions

7.1.1 Introduction

In this thesis the development of an ultrasonic distance detection system for spinal cord stimulation (SCS) has been described. This chapter comprises the main observations and conclusions originating from the work described in this thesis. These observations and conclusions are grouped in sections to their corresponding subject. At the end of this chapter some suggestions for further research are listed.

7.1.2 System requirements

The transducer for distance detection in the spinal cord stimulation (SCS) system must be integrated on the electrode array. Therefore, the transducer dimensions are limited to an area of 5 mm × 5 mm and a thickness of 2 mm. The power consumption should be low to limit battery drain of the implantable pulse generator. This implies a high efficiency to minimize power consumption. The distance between the electrode array and the spinal cord may vary between 1 mm and 10 mm. Because most electrodes are implanted in the low thoracic region (T11-T12) the range varies between 3.0 mm and 6.5 mm. The position of the spinal cord should be measured with an accuracy of at least 0.5 mm for op-

timal stimulation. The sound velocity in the surrounding fluid (CSF) is approximately 1500 m/s resulting in a minimum frequency of the required ultrasonic wave of 1.5 MHz to enable a resolution of 0.5 mm. The reflected signal to be detected is small because the acoustic impedance of the spinal cord is close to the value of the CSF. Therefore it is likely that the signal-to-noise ratio (*SNR*) of the transducer signal will be critical.

7.1.3 Transducer modeling

A modified KLM model was implemented in APLAC to model a thickness mode piezoelectric transducer. The modification includes both dielectric and mechanical losses. A method for parameter estimation was used, followed by an optimization procedure to minimize the error between measurement and simulation results.

The modified KLM model was verified using different experiments with a PXE-5 transducer, i.e. impedance measurement, insertion loss and pulse-echo measurements. The proposed model predicts the shape of the insertion loss well, but the simulated insertion loss is approximately 5 dB less than the empirical value. The results of the pulse-echo simulations and experiments show that the shape of the measured and simulated signal match. The difference between the simulated and measured pulse-echo amplitude corresponds to the difference in the insertion loss. It is concluded that the model is useful to predict the transducer's behavior.

7.1.4 The multi-element transducer

The optimum transducer can be characterized as the transducer with the lowest insertion loss, a pulse-echo response with the highest peak-peak amplitude and the highest *SNR*. Four transducer types were presented: single element, dual element, stacked and multi-element transducer. Two piezoelectric materials, i.e. PVDF and PXE-5, were used for the simulations of the four transducer types. The simulation results of these four transducer types showed that the single element PXE-5 transducer has superior pulse-echo response and *SNR*. Improvement of the transducer’s performance may only be achieved by optimizing a PXE-5 transducer resulting in the construction of a multi-element transducer.

APLAC simulations predict that a PXE-5 based multi-element transducer gives a better *SNR* than a single element transducer with the same total area. According to the simulation results a transducer with an effective area of 4 mm $\times$ 4 mm consisting of 16 elements has an *SNR* that is 2.4 dB higher than a single element transducer of the same area. However, increasing the number of transducer elements does not result in an unlimited *SNR* increase.

A single and multi-element PXE-5 transducer with an area of 4 mm × 4 mm were realized. The multi-element transducer consisted of 16 elements. The per-

formance of the realized transducers was compared to the simulation results. The experimental data on the transducer input impedance and insertion loss matched the simulated data. *SNR* experiments showed that the *SNR* of the multi-element transducer increased 2 dB with respect to the single element transducer, which is in agreement with the theoretically expected increase of 2.4 dB.

Changing the load impedance from 50 Ω to 1 MΩ increases the signal-to-noise ratio by approximately 6 dB. Together an increase of 8 dB can be achieved, which is, however, not sufficient to detect the echo signal reliably in a simple way. Therefore, a filter based on amplitude demodulation was designed to be able to detect echo signals with an *SNR* of 10 dB.

7.1.5 The amplitude demodulation filter

The performance of the amplitude demodulation filter was tested by comparing its performance to that of a matched filter, which is commonly used for the detection of echo signals buried in noise. The detection rate of the amplitude demodulation filter is comparable to that of the matched filter, although the first performs slightly better. Using an input signal with an *SNR* of 10 dB for the amplitude demodulation filter gives a detection rate of 98 %, i.e. the percentage of echoes detected within a confidence interval of 330 ns (corresponding to a resolution of 0.5 mm). An analog amplitude demodulation filter has been realized, which performs similar to the simulated filter.

7.1.6 Final conclusions

The area of the realized transducer is 4 mm × 4 mm, which is within the maximum allowed dimensions. The thickness of the backing was 4.5 mm, which exceeds the maximum thickness of 2 mm. The PXE-5 thickness is 0.3 mm. Thus by reducing the backing thickness by 3 mm, the total transducer thickness will be less than 2 mm.

A multi-element transducer and an amplitude demodulation filter have been realized that are capable of measuring the distance ranging from 4 mm to 10 mm of an interface, spinal cord phantom in water, with a reflection coefficient of 15 %. The resolution of the distance measurement is at least 0.5 mm, which is sufficient for distance detection in SCS. Unfortunately, the echo from the spinal cord phantom cannot be detected if the distance between the transducer and the phantom is less than 4 mm, which is a serious limitation.

7.2 Suggestions for further research

7.2.1 Introduction

This section is divided into three different parts. First, the electronics and the integration with the existing SCS systems will be discussed. Second, the reliability of echo detection and how to distinguish false detection from a true echo will be discussed. Third, the design of the entire transducer and integration on the electrode array will be discussed.

7.2.2 Electronics

The electronics for the distance detection system need to be integrated with the electronics of the implantable pulse generator. This extended system for spinal cord stimulation should measure the delay and control the amplitude of the pulses stimulating the spinal cord. The electronic system should preferably drive the piezoelectric transducer as well.

The excitation pulse used for the experiments was a single sine pulse. This was done to reduce the effect of the width and length resonances. However, for a practical solution a single sine pulse is generally more difficult to realize than a mono- or biphasic square pulse (as used in the implantable pulse generator for nerve stimulation). Simulations predict that the peak-peak amplitude of the echo from a monophasic square pulse is about 75 % of that from a biphasic square pulse. The peak-peak amplitude of the echo from a square biphasic pulse is equal to that of a single sine pulse. The energy content of the different input signals is equal. Another advantage of the biphasic square pulse is that its amplitude is 71 % of that of the single sine pulse with the same energy content. A disadvantage of a square pulse is that it not only actuates the thickness resonance of the transducer, but also the length and width resonances.

7.2.3 Echo detection: resolution and reliability

The resolution of the distance measurement is most critical for small distances ranging from 2 mm to 5 mm. Therefore, the resolution of distance measurements with the spinal cord phantom as presented in subsection 6.3.2 is examined. Decreasing the confidence interval from 330 µs to 133 µs, corresponding to a resolution of 0.2 mm, results in a detection rate of 93 % and 76 % for the amplitude demodulation and matched filter, respectively. The detection increases to 98 % and 94 % for the amplitude demodulation and matched filter, respectively, if the desired resolution is 0.3 mm. Although the detection rate is quite high, a method should be found to enable the system to discriminate between a false or true echo detection. Two alternatives are given here. In the first alternative two successive measurements within 50 µs are made and the outcome of both measurements is compared. It is unlikely that the position of the spinal cord will

change dramatically in this short time. Therefore, to classify the measurement as valid the outcome of two measurements should be within the confidence interval. This method is rather power consuming, which leads to the second alternative. In this thesis the first echo signal was determined to measure the distance between the transducer and the spinal cord phantom. However, a second and even a third echo signal can be found, although they are very small. These echoes originate from the ultrasonic wave reflecting on the transducer to the spinal cord phantom and back to the transducer, etc. The delay between the excitation of the transducer and the first echo is equal to the delay between the first and second echo. Thus, if the second echo signal can be detected reliably, this would be a good method to improve the system's reliability.

7.2.4 Transducer design and integration

Ringing of the transducer must be reduced to enable detection of the spinal cord at distances below 4 mm. Even more important is the reduction of the echo signal of the backing-water interface, which appears at 3.9 μs and interferes with an echo corresponding to a distance of 3 mm. The effect of this signal can be made less interfering by making the backing thinner. Its thickness should be reduced from 4.5 mm to 1.5 mm to obtain a transducer with a total thickness of 2 mm. The echo from the backing-water interface will then appear at 1.3 μs, which is sufficient to reduce the minimum detectable distance to 1 mm.

Another issue, which has not been described in this thesis yet, is the integration of the piezoelectric transducer on the electrode array. The electrode array is made of silicone rubber, which attenuates ultrasound considerably. Therefore, encapsulating the transducer in the paddle is not recommended, because the echo signal will be reduced such that detection becomes very difficult. It is suggested to design a transducer backing with an area larger than that of the piezoelectric material. In this way the transducer can be clamped in the electrode array, preventing it to be separated from the array.

Appendix A

Signal processing definitions

A.1 Convolution and correlation

The convolution of two functions $x(t)$ and $y(t)$ in the time domain is:

$$x(t) \otimes y(t) = \int_{-\infty}^{\infty} x(\tau) y(t-\tau) d\tau \tag{A–1}$$

If $x(t) \leftrightarrow X(\omega)$ and $y(t) \leftrightarrow Y(\omega)$, then the Fourier transform of equation (A–1) can be written as:

$$\mathrm{F}\{x(t) \otimes y(t)\} = X(\omega) Y(\omega) \tag{A–2}$$

The inverse transform can be denoted as:

$$x(t) \otimes y(t) = F^{-1}\{X(\omega) Y(\omega)\} \tag{A–3}$$

The cross-correlation $R_{XY}(\tau)$ between two functions $x(t)$ and $y(t)$ is defined by:

$$R_{XY}(\tau) = E\{x(t) y(t+\tau)\} = \int_{-\infty}^{\infty} x(t) y(t+\tau) dt \tag{A–4}$$

where $E\{\ldots\}$ is the mathematical expectation.

The inverse Fourier transform of the cross-correlation is:

$$\mathrm{F}^{-1}\{R_{XY}(\tau)\} = X^*(\omega) Y(\omega) \tag{A–5}$$

where $X^*(\omega)$ denotes the complex conjugated. The auto-correlation of a function $x(t)$ is $R_{XX}(\tau)$. The inverse Fourier transform of this function is:

$$\mathrm{F}^{-1}\{R_{XX}(\tau)\} = X^*(\omega) X(\omega) = |X(\omega)|^2 \tag{A–6}$$

In general, it can be stated that multiplying in one domain corresponds to convolution in the other domain, and vice versa.

A.2 Energy and power spectrum

The energy of a signal $x(t)$ in the time domain is:

$$S = \int_{-\infty}^{\infty} |x(t)|^2 dt \tag{A–7}$$

This energy is equal to the energy of the signal in the frequency domain (Parseval's Theorem):

$$S = \int_{-\infty}^{\infty} |x(t)|^2 dt = \frac{1}{2\pi} \int_{-\infty}^{\infty} |X(\omega)|^2 d\omega \tag{A–8}$$

The energy spectrum of a signal $x(t)$ is defined as:

$$S_{XX}(\omega) = X^*(\omega)X(\omega) \tag{A–9}$$

The previous equation and equation (A–6) give the following transform pair (Wiener-Khintchine theorem):

$$R_{XX}(\tau) \leftrightarrow S_{XX}(\omega) \tag{A–10}$$

The power spectrum $P_{XX}(\omega)$ represents the energy flow per unit frequency range per unit time averaged over all time, denoted as:

$$P_{XX}(\omega) = \lim_{T\to\infty} \frac{1}{T} X(\omega)X^*(\omega) = \lim_{T\to\infty} \frac{1}{T} S(\omega) \tag{A–11}$$

The power spectra of the input ($P_{XX}(\omega)$) and the output ($P_{YY}(\omega)$) of a filter with a transfer function $H(\omega)$ are related by:

$$P_{YY}(\omega) = |H(\omega)|^2 P_{XX}(\omega) \tag{A–12}$$

A.3 Schwarz's inequality

The Schwarz inequality is given by:

$$\left(\int f(t)g(t)dt\right)^2 \le \int (f(t))^2 dt \int (g(t))^2 dt \tag{A–13}$$

The left and right side are equal when:

$$g(t) = af^*(t) \tag{A–14}$$

where a is a constant, and $f^*(t)$ the complex conjugated of $f(t)$ or in the frequency domain:

$$G(\omega) = aF^*(\omega) \tag{A–15}$$

Appendix B

AM demodulation filter

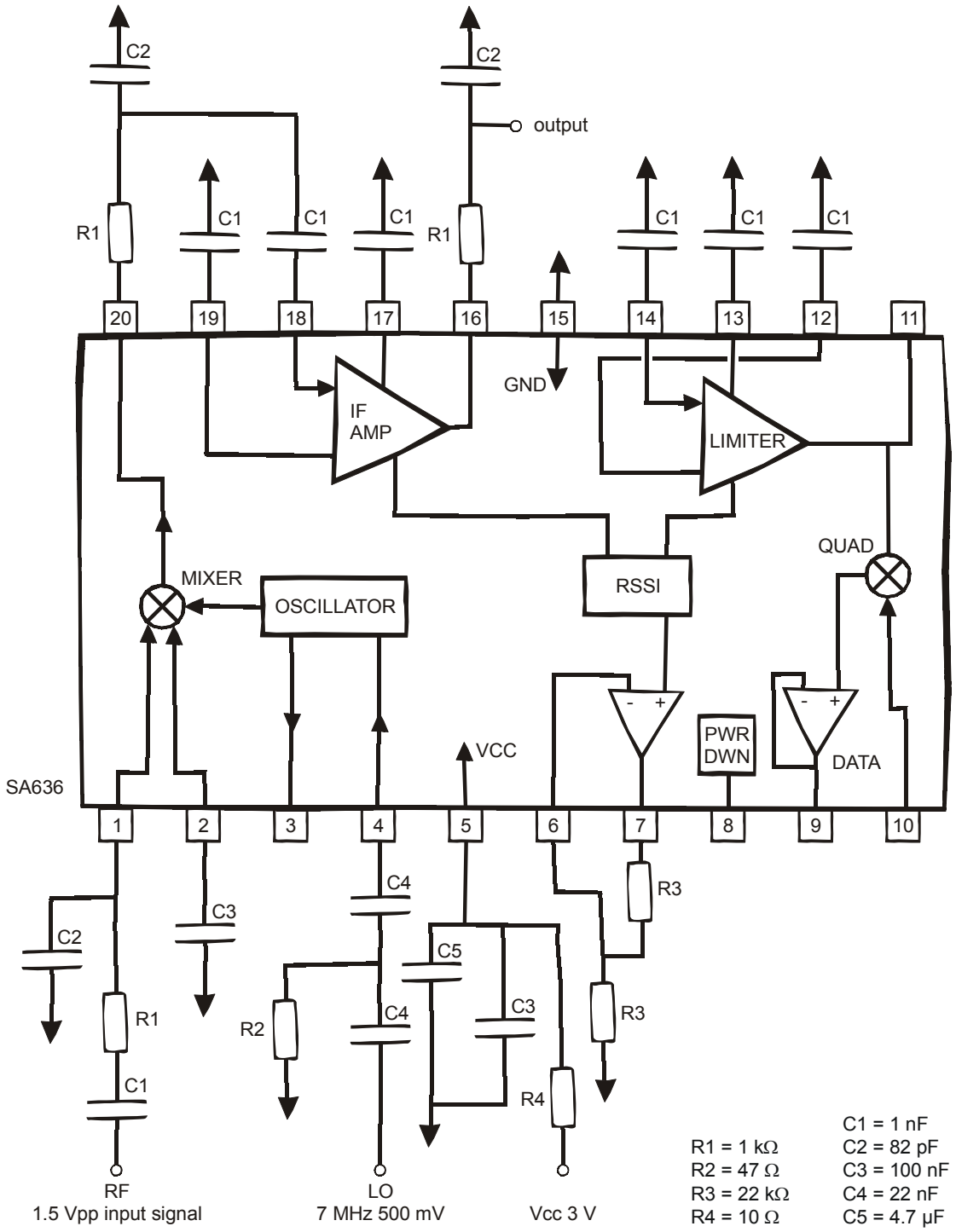

Schematic diagram of the amplitude demodulation filter consisting of the Philips SA636.

Summary

Spinal cord stimulation (SCS) is a clinical method for primarily the management of chronic, intractable pain. The method is based on electrical stimulation of nerve fibers in the posterior part of the spinal cord. An electric field is applied by an electrode array, implanted medially in the posterior epidural space, at some distance from the spinal cord. An implantable pulse generator provides the electrical stimulation pulses to the electrode array via a cable. When stimulating the spinal cord with pulses of constant amplitude, the current density in the spinal cord and thus the effects on nerve fibers will change with body position and/or posture, due to the varying distance between the spinal cord and the stimulating electrode array. As a result, the pain relieving effect may either vanish (when the distance is too large), or be dominated by uncomfortable sensations. To avoid these adverse conditions the current density in the spinal cord has to remain within a small window. In present SCS systems the stimulus applied by the electrode array is either set at a constant value, or the patient is allowed to select one out of only two preset pulse amplitudes. Therefore, a major improvement would be achieved if the distance between stimulation electrode array and spinal cord could be measured and used as a feedback signal to control the stimulus amplitude in a closed-loop system. Therefore, an ultrasonic distance detection system has been proposed to measure the distance between stimulation electrode array and the spinal cord. The ultrasonic system consists of a piezoelectric transducer and an echo detection circuit. To enable the design and optimization of the piezoelectric transducer an appropriate model description is needed.

In chapter 2 the KLM model for a thickness mode piezoelectric transducer is presented. The KLM model has been modified to provide modeling of losses in piezoelectric materials. A lossy transmission line and a complex elastic stiffness were used to model the mechanical losses, whereas the dielectric losses were modeled by a complex dielectric constant. The modified KLM model was implemented in APLAC. The model was verified by simulating and measuring the input impedance in the frequency domain of a ceramic and polymer transducer. A first approximation of the piezoelectric parameters was obtained from the measured

input impedance. Subsequently, the simulated input impedance was fitted to the measured data by varying several model parameters for the best possible fit. Computation of the pulse-echo response on an arbitrary transmitted signal was accomplished by considering the KLM circuit as a two-port network and propagating the input waveform to and from a water load. The transfer function was obtained by calculating the ratio of the transducer response signal to the input signal in the frequency domain. The product of the input signal and the transfer function was transformed by an inverse Fourier method to calculate the response of the transducer in the time domain. Simulation and measurement results of a ceramic and polymer transducer both in the frequency and time domain are presented. Excellent agreement between measured and simulated data was obtained.

The design criteria for transducer optimization were presented in chapter 1. These criteria are: transducer size and maximize the signal-to-noise ratio. In chapter 3 several transducer types are presented and simulated to investigate which type is the most appropriate choice. Besides the single element piezoelectric transducer, three other transducer types are introduced. First, the dual element transducer is presented. This transducer contains an emitting and a receiving element in a single housing, allowing emitter and receiver to operate independently. The emitter and receiver are placed next to each other and can be made of the same material, but also from different materials. The second type is the stacked transducer in which a polymer transducer element is put on top of a ceramic transducer element. The ceramic element is used as the emitter and the polymer element is used for receiving the reflected acoustic signal. Third, the multi-element transducer consisting of several transducer elements of the same material in a chessboard-like architecture is shown. In the actuating mode all the elements are connected in parallel and thus one large transducer is created. In the sensing mode, the elements are read individually and the separate signals are added to improve the signal-to-noise ratio (*SNR*).

The proposed transducer types, including the single element transducer as a reference, were simulated. The simulations were used to find the optimum signal transfer and minimal power consumption and include noise analysis for calculating the *SNR*. The simulations show that the stacked configuration increases neither the signal transfer nor the *SNR* with respect to a single element transducer. Therefore, a multi-element transducer is proposed to enhance the *SNR* and to keep the power consumption low. Simulations show that a transducer consisting of multiple transducer elements has a better *SNR* than a single element transducer with an equivalent area. However, the *SNR* increase of a multi-element transducer is limited. For a given transducer area the *SNR* increases up to a maximum by increasing the number of transducer elements. Nevertheless, the multi-element transducer performs best concerning signal-to-noise ratio and signal transfer with respect to the other transducer types.

In chapter 4, the processing and characterization method of two transducers types, i.e. the single-element transducer and the multi-element transducer, are described. First, two different single-element transducers were made: a large transducer (20 mm × 20 mm) and a small transducer (4 mm × 4 mm). Second, two multi-element transducers were fabricated. One consisting of four elements with an area of 4 mm × 4 mm each, the large multi-element transducer, and another one consisting of 16 square elements with a total area of 16 mm^2, the small multi-element transducer. For the initial experiments the large multi-element transducer should be sufficient to verify the *SNR* improvement of the summed output signal of the multi-element transducer. Two measurement set-ups can be discerned: one for transducer characterization and one for the pulse-echo measurements. In the first measurement setup the input impedance and the insertion loss of the transducer are measured (frequency domain), whereas in the other setup the pulse-echo response of the transducer is measured (time domain).

The experimental results obtained from the single and multi-element transducers are presented in chapter 5. First, the input impedance of the transducer, including its wires, was measured by an impedance analyzer and calculated by APLAC. The transducer model parameter values were varied to match the simulation data to the experimental data. This was done for all four transducers. The transducer impedance can be modeled accurately by the proposed modified KLM model. An additional model for the wires that were connected to the transducer was added to the model. The modeled and experimentally obtained transducer impedance were in good agreement. The insertion loss of the transducers was measured, and compared to the simulation results, to obtain the appropriate excitation pulse frequency. The parameter values obtained by transducer impedance matching were used for the insertion loss simulations. The model predicts the shape of the insertion loss well, but the magnitude of insertion loss is approximately 5 dB less for the simulation than the experimentally obtained insertion loss. The simulated pulse-echo response for the large single element transducer was compared to the measured pulse-echo. The results show that the shape of the measured and simulated signal match. The amplitude of the measured signal is smaller than the simulated amplitude, but the difference corresponds to the difference in the insertion loss. Subsequently, the *SNR* was obtained for the multi-element transducer and compared to the *SNR* of the single element transducer. The *SNR* increases 6.8 dB for the large multi-element transducer with respect to the single element transducer. The *SNR* of the small multi-element transducer increases 2 dB compared to that of a single element transducer. The *SNR* of the small multi-element transducer increases by approximately 6 dB when changing the load impedance from 50 Ω to 1 MΩ. Together an increase of 8 dB can be achieved, which is, however, not sufficient to detect the echo signal reliably in a simple way. Therefore, a signal processing

method is developed to detect the echoes reliably, which is presented in chapter 6.

In chapter 6 a low power electronic circuit is described which enables detection of the small echo signals from the spinal cord and, accordingly, measures the delay between the emitted and received ultrasonic pulse. The system requirements have to be identified to make the appropriate choices for a detection system. The signal to be detected mainly determines the filter to be used. Therefore, the statistical properties of the echo signal are analyzed. Subsequently, two filters are described, i.e. a matched filter and an amplitude demodulation filter. Based on the signal analysis and other criteria, e.g. power consumption, the amplitude demodulation filter was selected as the most suitable one. To test the filtering capabilities of the amplitude demodulation filter its performance was compared to that of a matched filter, which is commonly used for the detection of echo signals buried in noise. For that purpose, both filter methods were simulated in APLAC using measured echo signals. The amplitude demodulation filter shows results comparable to those of the matched filter. The amplitude demodulation filter was realized in hardware. Experimental results showed that the amplitude demodulation filter performs as expected.

Finally, the conclusions are listed in chapter 7. The proposed system shows that it is possible to measure the distance, ranging from 4 mm to 10 mm, between the spinal cord phantom and piezoelectric transducer with this transducer with the required accuracy of 0.5 mm. The area of the realized transducer is within the maximum allowed dimensions. The thickness of the transducer exceeds the maximum thickness. However, the thickness of the transducer backing can be reduced so that the total transducer thickness will within the maximum allowed thickness. If the backing thickness is reduced it will also be possible to detect distances below 4 mm.

Samenvatting

Ruggenmergstimulatie is een klinische methode die voornamelijk gebruikt wordt voor de behandeling van chronische, niet op andere wijze te behandelen pijn. De methode is gebaseerd op de elektrische stimulatie van de zenuwvezels aan de achterzijde van het ruggenmerg. Een elektrisch veld wordt aangelegd met een elektrode-array dat in het midden, aan de achterzijde van de epidurale ruimte geïmplanteerd is op enige afstand van het ruggenmerg. Een geïmplanteerde pulsgenerator biedt de elektrische stimulatiepulsen via een kabel aan het elektrode-array aan. Ten gevolge van een veranderende lichaamshouding of –positie, verandert de afstand tussen de stimulatie-elektrode en het ruggenmerg. Als deze afstand verandert en het ruggenmerg wordt gestimuleerd met pulsen met een constante amplitude dan zal de stroomdichtheid in het ruggenmerg variëren, en dus het effect op de zenuwvezels. Dit heeft tot gevolg dat de pijnverzachtende effecten zullen verdwijnen als de afstand te groot is, of dat deze zullen worden gedomineerd door onaangename sensaties als de afstand te klein is. Om deze ongewenste effecten te voorkomen dient de stroomdichtheid in het ruggenmerg binnen nauwe grenzen te blijven. In de huidige ruggenmergstimulatiesystemen wordt de aangebrachte prikkel ofwel op een constante waarde ingesteld, of de patiënt heeft de keuze uit twee vooraf instelbare pulsamplitudes. Het systeem kan worden verbeterd als de afstand tussen het elektrode-array en het ruggenmerg gemeten kan worden en gebruikt kan worden als terugkoppelsignaal om de amplitude van de stimulatiepulsen automatisch aan te passen door middel van een gesloten systeem. Daartoe wordt een meetsysteem voorgesteld waarmee een ultrasone puls vanaf het elektrode-array wordt uitgezonden en gereflecteerd door het ruggenmerg. Het gereflecteerde signaal wordt vervolgens gemeten en de looptijd van de puls, die evenredig is met de afstand tussen elektrode-array en ruggenmerg, wordt als terugkoppelsignaal gebruikt. Het ultrasoon detektiesysteem bestaat uit een piëzoelektrische transducent en een echodetectiecircuit. Om de benodigde piëzoelektrische transducent te ontwerpen en te optimaliseren is een model van de transducent gewenst.

In hoofdstuk 2 wordt het KLM-model voor een dikte-mode piëzoelektrische transducent gepresenteerd. Het KLM-model is aangepast om ook de verliezen in

piëzoelektrische materialen te kunnen modelleren. Een lossy transmissielijn en een complexe elastische stijfheid zijn gebruikt om de mechanische verliezen te modelleren, terwijl de elektrische verliezen zijn gemodelleerd door een complexe diëlektrische constante. Het aangepaste KLM-model is geïmplementeerd in APLAC. Het model is geverifieerd door de gesimuleerde en gemeten ingangsimpedantie als functie van de frequentie te vergelijken voor zowel een keramische als een polymeer transducent. Een eerste benadering voor de piëzoelektrische modelparameters is verkregen uit de gemeten ingangsimpedantie. Vervolgens is de gesimuleerde ingangsimpedantie optimaal gefit aan de gemeten ingangsimpedantie door een aantal modelparameters aan te passen. De puls-echo responsie ten gevolge van een willekeurig signaal wordt bepaald door het KLM-model als een twee-poort te beschouwen die het ingangsignaal geleidt naar en van een waterbelasting. De overdrachtsfunctie wordt bepaald door de verhouding te berekenen van het uitgangs- en ingangssignaal van de transducent in het frequentiedomein. Het product van het ingangssignaal en de overdrachtsfunctie is inverse Fourier getransformeerd om de responsie in het tijddomein te bepalen. Simulatie- en meetresultaten van een keramische en een polymeer transducent, zowel in het tijd- als frequentiedomein, zijn gepresenteerd. De gemeten en gesimuleerde data komen uitstekend overeen.

De ontwerpcriteria zijn in hoofdstuk 1 vastgesteld. Deze zijn: transducentgrootte en het maximaliseren van de signaal-ruis-verhouding. In hoofdstuk 3 worden verschillende typen transducenten gepresenteerd en gesimuleerd om vast te stellen welk type het meest geschikt is. Naast de één-element transducent worden drie andere typen geïntroduceerd. Allereerst de dubbele transducent, die bestaat uit een onafhankelijk zend- en een ontvangstelement in één behuizing. De zender en ontvanger worden naast elkaar geplaatst en kunnen van hetzelfde of van verschillende materialen worden gemaakt. Het tweede type is de gestapelde transducent, waarbij een polymeer transducent element boven op een keramisch transducent element is geplaatst. De keramische transducent wordt gebruikt als zender en de polymeer transducent als ontvanger. Als derde wordt een multi-element transducent voorgesteld. Deze bestaat uit verschillende kleine elementen van hetzelfde materiaal in een matrix. Tijdens het zenden worden de elementen parallel geschakeld, zodat er sprake is van een grote transducent. In ontvangstmode worden de elementen ieder afzonderlijk uitgelezen en worden de verschillende signalen opgeteld om de signaal-ruis-verhouding te verbeteren. De bovengenoemde transducenten, inclusief de één-element transducent, gebruikt als referentie, zijn gesimuleerd. De simulatieresultaten zijn gebruikt om de optimale signaaloverdracht en minimaal vermogensverbruik te vinden. Tevens is er een ruisanalyse uitgevoerd om de signaal-ruis-verhouding te berekenen. De simulatieresultaten tonen aan dat noch de signaaloverdracht noch de signaal-ruis-verhouding van de gestapelde transducent verbeteren ten opzichte van de één-element transducent. De simulatieresultaten laten voor de multi-element transducent een verbeterde signaal-ruis-verhouding zien ten opzichte van de één-

element transducent met een gelijk oppervlak. Echter, de signaal-ruis-verhouding heeft een plafond. Voor een bepaald oppervlak neemt de signaal-ruis-verhouding niet oneindig toe als het aantal elementen toeneemt. Desondanks presteert de multi-element transducent vergeleken met de andere transducent typen als beste wat betreft de signaal-ruis-verhouding en signaaloverdracht.

In hoofdstuk 4 wordt de vervaardiging en karakterisatie van de één-element en multi-element transducent beschreven. Er zijn twee één-element transducenten gemaakt: een grote (20 mm × 20 mm) en een kleine (4 mm × 4 mm). Eveneens zijn er twee multi-element transducenten gemaakt. Eén bestaande uit vier elementen waarvan ieder element een oppervlakte heeft van 4 mm × 4 mm: de grote multi-element transducent, en één bestaande uit 16 elementen met een totaal oppervlak van 16 mm^2: de kleine multi-element transducent. Voor de eerste experimenten is het voldoende om de verbetering van de signaal-ruis-verhouding aan te tonen van de grote multi-element transducent. Er worden twee verschillende meetopstellingen besproken. Eén voor de karakterisatie van de transducenten en één voor het doen van puls-echo metingen. Bij de karakterisatie van de transducent wordt de ingangsimpedantie en de insertion loss van de transducent bepaald in het frequentie domein. Met de andere opstelling wordt de puls-echo responsie van de transducent gemeten in het tijd domein.

De experimentele resultaten verkregen van de single en multi-element transducent worden in hoofdstuk 5 gepresenteerd. De ingangsimpedantie van de transducent, inclusief de draden, is gemeten met behulp van een impedance analyzer en berekend met APLAC. De transducent parameters zijn zodanig aangepast dat de gesimuleerde data overeenkomen met de gemeten data. Dit is gedaan voor alle vier de transducenten. De ingangsimpedantie van de transducent kan nauwkeurig gemodelleerd worden met het aangepaste KLM-model. Extra componenten zijn toegevoegd om de draden te modelleren. De gemeten en gesimuleerde data komen uitstekend overeen. De insertion loss van de transducenten is gemeten, en vergeleken met de gesimuleerde data, om de optimale excitatiefrequentie te bepalen. De parameterwaarden, zoals bepaald voor de ingangsimpedantie zijn ook gebruikt voor de insertion loss simulaties. Het aangepaste KLM-model voorspelt de vorm van de insertion loss goed, maar de absolute waarde ligt ongeveer 5 dB hoger dan de gemeten waarden. De puls-echo responsie voor de grote één-element transducent is gemeten en vergeleken met de gesimuleerde responsie. De vorm van beide signalen komt overeen. De amplitude van de gemeten puls-echo responsie is lager dan die van de gesimuleerde responsie. Dit verschil komt overeen met het verschil in de gemeten en berekende insertion loss. Vervolgens is de signaal-ruis-verhouding bepaald voor de grote multi-element transducent en vergeleken met die van de één-element transducent. De signaal-ruis-verhouding van de multi-element transducent is 6.8 dB hoger dan die van de één-element transducent. De signaal-ruis-verhouding van de kleine multi-element transducent neemt 2 dB toe ten opzichte van de één-element

transducent. Als de belastingsweerstand van de transducent verhoogd wordt van 50 Ω naar 1 MΩ neemt de signaal-ruis-verhouding met ongeveer 6 dB toe. Indien beide worden toegepast zal de signaal-ruis-verhouding ongeveer 8 dB toenemen tot een waarde van 10 dB. Echter, dit is onvoldoende om de echo op eenvoudige wijze te bepalen. Daarom wordt er in hoofdstuk 6 een methode gepresenteerd om de echo's op een betrouwbare manier te bepalen.

In hoofdstuk 6 komt een laag vermogen elektronisch circuit aan bod dat het mogelijk maakt om de echosignalen afkomstig van het ruggenmerg te detecteren en daaruit de tijd tussen het uitzenden en ontvangen van de ultrasone puls te bepalen. De signaal-ruis-verhouding van het signaal is laag waardoor het moeilijk is om op een eenvoudige manier de echo te detecteren. Daarom is er een filter ontwikkeld dat het mogelijk maakt om op een betrouwbare manier de echo te detecteren. Allereerst dienen de systeemeisen omschreven te worden om een goede keuze van het detectiefilter mogelijk te maken. De keuze van het filter wordt in hoge mate bepaald door het signaal dat gedetecteerd moet worden. Hiertoe worden de statistische parameters van het echosignaal geanalyseerd. Vervolgens worden er twee filters besproken: het matched filter en het amplitude demodulatie filter. Op basis van de signaalanalyse en andere criteria, bijvoorbeeld vermogensverbruik, is het amplitude demodulatie filter gekozen als meest geschikt. Om de prestaties van dit filter te testen worden de resultaten ervan vergeleken met die van het matched filter. Dit filter wordt algemeen gebruikt om echosignalen met een zeer lage signaal-ruis-verhouding te detecteren. Beide filters zijn geïmplementeerd in APLAC en getest met daadwerkelijk gemeten signalen. De resultaten van het amplitude demodulatie filter zijn vergelijkbaar met die van het matched filter. Het amplitude demodulatie filter is gerealiseerd in hardware en experimentele resultaten laten zien dat het filter werkt zoals voorspeld.

Tot slot worden in hoofdstuk 7 de conclusies besproken. Het voorgestelde systeem maakt het mogelijk om afstanden van 4 mm tot 10 mm tussen de transducent en het ruggenmerg te meten met de vereiste nauwkeurigheid van 0.5 mm. Het oppervlak van de gerealiseerde transducent ligt binnen de grenzen van de maximale afmetingen. De dikte van de transducent overschrijdt de maximale dikte, maar dit kan opgelost worden door de dikte van de backing te verkleinen. Dit zal tevens tot gevolg hebben dat het mogelijk wordt om afstanden kleiner dan 4 mm te bepalen.